Evidence of an Allostatic Response by Intestinal Tissues Following Induction of Joint Inflammation

Meghan M. Moran[1, 2, 3*], Jun Li[3], Quan Shen[4], Sheona P. Drummond[5], Caroline M. Milner[5], Anthony J. Day[5], Ankur Naqib[1, 6], D. R. Sumner[1, 2], Anna Plaas[3]

1- Dept. of Anatomy & Cell Biology, Rush University Medical Center (RUMC), Chicago, IL, USA
2- Dept. of Orthopedic Surgery, RUMC, Chicago, IL, USA
3- Dept. of Int. Medicine (Rheumatology), RUMC, Chicago, IL, USA
4- Dept. of Neurosurgery, RUMC, Chicago, IL, USA
5- Manchester Cell-Matrix Centre & Lydia Becker Institute of Immunology and Inflammation, Faculty of Biology, Medicine and Health, The University of Manchester, Manchester, UK; 6- Bioinformatics Core, RUMC, Chicago, IL, USA

*Corresponding Author: Meghan M. Moran, meghan_moran@rush.edu

ABSTRACT

Disrupted intestinal epithelial barrier function has been proposed to be integral to rheumatoid arthritis (RA) progression and pathogenesis. To further define the molecular pathways in synovial inflammation and the response of the intestinal tissues, we have used a rat model of mono-joint inflammatory arthritis, induced by intra-articular injection of Complete Freund's adjuvant (CFA). The predominant inflammatory response of a single injection of the adjuvant into the knee joint resulted in rapid and reproducible formation of a fibrotic myeloid-infiltrated synovial pannus. Our aim was to determine how intestinal tissues, including the proximal and distal ileum and distal colon, responded to inflammatory changes in the synovium in a temporally coordinated manner by comparing their transcriptomic landscapes using RNASeq analyses. We confirmed the timeline of joint inflammation by knee joint swelling measurement, increased synovial fluid levels of bikunin (a component of both the acute phase protein pre-alpha-inhibitor and inter-alpha-inhibitor) and demonstrated a self-correcting response of trabecular and cortical bone to the CFA challenge. Intestine-specific responses were monitored by 16S microbiome amplicon sequencing, histopathology for mucus layer integrity, and immune cell immunohistochemistry. We present data that shows the intestinal tissue displays an allostatic response to the acute joint inflammation and was region specific. The ileum primarily responded with increased mucus secretion and silencing of T-cell specific pathways, whereas the colon showed a transient upregulation of macrophages, with a broader suppression of immune related and metabolic pathway related transcripts. Interestingly, many neuropathways were activated early but then suppressed later in both the ileum and colon. There were only insignificant changes in the fecal microbiome composition in ileum or colon post-CFA administration. In summary, our data show for the first time a suppression of intestinal inflammatory and immune responses following the induction of joint inflammation and only minimal and transient changes in the microbiome. The results help clarify the molecular responses of intestinal tissues to inflammatory stresses that accompany the pathogenesis of inflammatory joint diseases.

INTRODUCTION

In the past decade, numerous studies have focused on the role of 'gut health' in the progression of several chronic musculoskeletal disorders including rheumatoid arthritis, spondylarthrosis, ankylosing spondylitis, psoriatic arthritis[1, 2], osteoarthritis[3], and bone disorders[4], including osteoporosis[5] and implant loosening[6]. Many of these studies have reported alterations in the composition of the gut microbiota, defined as "dysbiosis", which includes decreased microbial diversity and/or expansion of specific bacterial taxa that affect the host physiology [7, 8].

However, since acute and chronic inflammatory disease states are accompanied by autocrine and paracrine production of mediators (i.e. cytokines, chemokines, and growth factors), activation of immune cells, and modification of enteric neuronal signals, they can transform the host intestinal environment by altering the structure and the intestinal barrier and function of its resident cells[9, 10]. The intestinal barrier is composed of an outer mucus layer in contact with the commensal gut microbiota[11], anti-microbial proteins, secreted immunoglobulin A molecules[12], a specialized epithelial cell layer[13], and an inner lamina propria that is populated with innate and adaptive immune cells[14]. The multicellular intestinal epithelium consists of multiple cell types, including absorptive enterocytes, mucin-secreting goblet cells, enteroendocrine cells, Paneth cells, and intraepithelial lymphocytes[15]. Furthermore, specific interactions of structural molecules secreted by the epithelial cells, such as mucins and tight junction proteins provide selective permeability for nutrient absorption, while also providing a blockade as primary defense against bacteria to maintain immune homeostasis[16].

Disruption of intestinal epithelial barrier function has been reported as integral to rheumatoid arthritis (RA) progression and pathogenesis [17, 18]. In fact, an early disease response in a collagen induced model for RA (CIA) was shown to be through the Zonulin-CXCR3 mediated dissociation of tight junctions [19]. In addition, elevated HIF2α in intestinal epithelial cells during RA progression can accelerate disease progression. Therapeutic mitigation of those pathogenic responses protected intestinal barrier function and diminished activation of intestinal and lymphatic T-helper 1 (Th1) and Th17 [20]. However, it remains to be determined if the intestinal responses are mediated by a disrupted systemic immune response in RA, and/or if the bone and cartilage destruction mediated by an inflamed synovium ("RA pannus") is the central link driving the intestinal pathogenesis in RA.

In addition to RA [21, 22], multiple reports suggest the existence of a "joint-gut communication axis" in osteoarthritis, spondylarthrosis, and degenerative disc disease [23-26] that can be part of disease initiation and/or progression. The gut microbiome is proposed as both a target and a mediator in this crosstalk. Likewise an increasing number of studies have explored a correlation between perturbed bone metabolism in osteoporosis, diabetes [27], fracture healing[28], and implant loosening [6] on intestinal homeostasis. These studies also focus predominantly on the role of intestinal dysbiosis and perturbed production of beneficial bacterial metabolites such as short chain fatty acids [21, 29-31], with a few studies implicating the role of T-cells in the communication routes [32, 33].

To further delineate the molecular and cell biological pathways in intestinal responses to joint inflammation, we used a rat model of mono-joint inflammatory arthritis, induced by intra-articular injection (IAI) of Complete Freund's adjuvant (CFA) [34, 35]. The predominant inflammatory response of a single injection of the adjuvant into the knee joint results in rapid and reproducible formation of a hyperplastic and fibrotic synovial pannus[36] and can produce changes in the intestinal microbiome [37, 38].

The objective of this study was to determine whether inflammatory changes in the CFA-exposed synovium induced temporally related changes in the intestinal barrier of the ileum and/or the colon. The timeline of joint inflammation was assessed by measuring knee joint swelling, joint histology, synovial fluid levels of bikunin (a component of both the acute phase protein pre-alpha-inhibitor (PαI) and inter-α-inhibitor (IαI) [39], bulk-RNA sequencing of synovial tissue, and micro-computed tomography for trabecular and cortical bone changes [40]. At the same time points, intestinal tissue responses were assessed by examining changes in components of the intestinal barrier. This included histochemical analyses of mucus layers, alterations in the intestinal tissue transcriptome using bulk-RNA Sequencing, composition of the mucus layers and abundance and distribution of CD4 and CD8 positive T-cells. 16S RNA analyses for fecal microbiome composition in ileum and colon was also completed.

Taken together, our data show that the intestinal tissue response to an acute joint inflammation was region specific. The ileum responded with increased mucus secretion and redistribution of CD8+ intraepithelial lymphocytes (IEL) as well as a broad suppression of immune function and metabolism-related transcripts. In addition, a concurrent silencing of similar pathways was seen in the colon. The intestinal cell response along with the minimal change in microbiome composition in either intestinal compartment indicated that as a result of an acute inflammation in the joint, intestinal cells will respond with allostasis[41]. This is a mechanism to defend against stress to protect barrier and immune functions as well as microbiota composition and thereby maintain overall function of the gut as a vital organ. This is discussed in the context of examining the mechanisms leading to failure of such preventative responses during progression of chronic inflammatory diseases, such as rheumatoid arthritis, to develop targeted interventions for mitigation of intestinal dysfunction in these diseases.

RESULTS

Knee joint responses following IAI of CFA

To establish a time course of knee joint responses following CFA or PBS injections, CFA-IAI and naïve rats were sacrificed at days 3, 7 and 14 post-IAI for analyses (**Fig. S1** and Methods). Knee joint swelling in the medial-lateral orientation had developed by 3d post-CFA-IAI and remained elevated through 14d ($p < 0.001$, 2-way ANOVA) compared to controls (**Fig. 1A**). There was a significant time effect with CFA-IAI ($p = 0.005$, 1 way ANOVA) as well as a time x study group interaction ($p = 0.008$, 2-way ANOVA).

A transient increase in serum effusion into the joint space was confirmed by synovial fluid accumulation of serum-derived bikunin•CS as well as in both inter-α-inhibitor (IαI) and pre-α-inhibitor (PαI) **(Fig. 1B & Fig. S2)** with a concurrent decrease in all these species in the serum (**Fig. 1C**). Furthermore, an abundance of albumin

and IgG in synovial fluids at 3d post-CFA-IAI (**Fig. S2**), as determined by SDS-PAGE confirmed the accumulation of serum derived components in the joint space. However, since these proteins were no longer present in the synovial fluids collected at 14d post-CFA, but increased knee diameters persisted, the latter was likely due to joint tissue responses, such as hyperplasia and fibrotic remodeling of the synovium and joint capsule, as well as patellar tendon swelling (**Figs. 1D-I**). No alteration in joint swelling, joint fluid composition or tissue remodeling were noted after PBS-IAI.

Transient changes in metaphyseal bone following CFA-IAI

As reported by others using the CFA rodent model [34, 42], micro-CT analyses of the distal femoral metaphyseal and epiphyseal bone detected changes in both the cortical and trabecular bone compartments. Surface pitting was observed at 3d post-CFA-IAI in the proximal region of the patellar groove and by 7d the pitting extended to the periosteal surface of the epiphysis and distal metaphysis. (**Fig. 2A**). Adjacent to the periosteal surface, periosteal reactions were present in n=7 7d and n=2 14d rats, primarily in the antero-mediolateral region of the distal femur (representative image, **Figs. 2B & S3**). These reactions occurred transiently coincident with the peak knee swelling, metaphyseal bone loss, and synovial fluid content of bikunin in response to CFA-IAI. By 14d the cortical surface pitting had resolved leading to the smooth appearance of the periosteal and patellar groove surfaces (**Fig. 2B & D**). These cortical changes were associated with significant alterations in cortical bone geometry. Specifically, cortical thickness exhibited significant differences with an overall one-way ANOVA result ($p = 0.003$), and Bonferroni post-hoc analysis revealed significant changes between 3d and 7d ($p = 0.022$) as well as between 3d and 14d ($p = 0.003$). Medullary area also showed an overall significant effect ($p = 0.031$), with Bonferroni post-hoc significance observed between 3d and 14d ($p = 0.041$). Similarly, total area demonstrated significant overall changes ($p = 0.036$), with Bonferroni post-hoc significance between 3d and 14d ($p = 0.047$). Cortical area showed a trend toward significance ($p = 0.069$). Trabecular bone volume fraction, normalized to pre-treatment groups, was significantly decreased in the distal femoral metaphysis following CFA-IAI (**Fig. 2E**). This reduction persisted through the 7d peak of inflammation and remained evident at 14d post-CFA-IAI.

Transcriptomic responses of the knee joint synovium following IAI of CFA or PBS

Assessment of changes in tissue- or cell-specific transcriptomic landscapes by RNASeq methodologies has become an essential tool to identify and quantitate responses to disease-causing injurious stimuli in a range of tissues [43]. We have applied bulk-RNASeq methodology and post-sequencing bioinformatic analyses to identify such changes using the Database of Essential Genes (DEG) and associated pathway responses of synovial tissues to IAI of CFA or PBS vehicle control injection.

A global overview of gene expression profiles in synovium at pre- (0d) and post-CFA or PBS is shown in **Fig. 3A**. Whereas PBS injections caused only minimal shifts (increased or decreased abundance) in gene expression profiles at early (3d) and or late (14d) time points, CFA-IAI resulted in extensive changes in the

transcriptome, at all time points (3d, 7d, and 14d). DEGs at each post-IAI treatment time point, relative to 0d were calculated and significantly modified genes were outlined in the volcano plots (**Fig. 3B-F;** red dots = activated >1.5 $\log_2$ FC, p-value<0.05 or suppressed <-1.5 $\log_2$FC, p<0.05). Using 'significant fold change' selection parameters, CFA exposure upregulated transcript abundance for 592, 1037, and 998 genes at 3, 7 and 14d, respectively, but decreased transcripts for 167, 998 and 166 genes at the corresponding time points. By comparison, after sham-IAI-PBS, increases relative to 0d occurred for 32 and 180 genes and suppression for 37 and 67 genes 3d and 14d, respectively.

The acute (3d) response to CFA-IAI resulted in limited but strong immune and inflammation responses, with >100 fold increases in transcripts of the neutrophil protein *S1009* [44], the macrophage receptor *Clec5a [45]* and the pro-angiogenic protease *Mmp9* [46] as well as the lymphocyte activating factor *Slamf6* [47]. In addition, multiple genes, previously identified with inflammatory arthritis showed sustained modification up to 14d. These included transcripts for pro-inflammatory mediators *Ccl3, Cxcl1, Ccl2, Ccl9,' Nos2, Arg1, Il1m, Il1b,* and *Osm,* their regulators *S100a9* [48], *Slamf6* and *Il1r2*, the C-type lectins *Clec5a* and *Clec4e [49]*, as well as *Lcn2* associated with bone damage in RA [50, 51]. In addition, macrophage activating factor *Gdf15* [52], *Adam8* and an integrin, *Itgb8*, from synovial fibroblasts [53] were affected. Notably, transcripts of the *Spp1* gene that encodes the bone protein OPN (osteopontin) and is associated with RA-related synovial inflammation [54], were highly activated in the acute joint response at 3d to both, CFA- and PBS-IAI and remained high up to 7d post-CFA-IAI. Furthermore, transcripts for multiple genes with known functions in innervation and inflammatory pain, *Kcne5, Grin3a, Map2, Erc2, Serpini1, Gprin3, Trhde,* and *Mdga2* were suppressed at all times post-CFA-IAI.

Transcriptomic responses of the proximal and distal ileum and distal colon following IAI of CFA

Bulk RNASeq analyses was also performed for intestinal tissues collected at 3, 7 and 14d post-CFA-IAI from the proximal and distal ileum and the distal colon. Bioinformatic analyses of sequencing data for DEGs, pathways, and biological process modifications were performed as described in the methods. It should be noted that since PBS-IAI did not yield significant modification of synovial gene transcriptions when compared to CFA exposure (**Fig. 3**), RNASeq analyses of gut tissues was only performed on naïve and CFA-treated gut samples. Gene expression profiles and DEGs for all three intestinal regions (proximal and distal ileum and colon) are shown in **Figs. 4-6,** respectively. These show a wide range of transcriptional changes relative to d0, with statistically significant increases and decreases in DEGs (<$\log_2$-1.5 and > $\log_2$+1.5). To supplement the volcano plots in B-D panels, details of DEGs are also shown as heat maps (**Figs. S3A-C** & **S4A-C)**. Together, these data show that changes in affected genes were region-specific and varied with time post-CFA treatment. For example, maximum modifications of the proximal ileal transcriptome were seen at 7d post-CFA, compared to 3d for the colonic transcriptome, with the distal ileum showing a weaker and rather uniform response at all 3 post-CFA time points (**Fig. S3**).

Transcripts that were modified at more than one post-CFA time point in each of the three intestinal regions are summarized in **Fig. S4A-C**, and many of these DEGs implicate responses of several cell types in the

intestinal barrier. For example, in the proximal ileum, the *Mptx1* pseudo gene [55, 56] is a gut-specific member of the pentraxin family, which is involved in bridging adaptive and innate immunities in inflammatory responses in enterocytes. It is a product of Paneth and epithelial cell transcripts for several REG family proteins, *Reg1a, Reg3b and Reg3G* [57, 58], which are multifunctional molecules secreted by Paneth cells to exert anti-apoptotic, anti-inflammatory and anti-microbial effects were decreased after CFA-IAI. Two genes, *Adgrg2* [59] and sodium and potassium absorption, *Tmprss15* [60], are known to be part of Tuft cell function in the regulation of immune responses. In addition, transcripts for two genes associated with neutrophil responses, *Mpo* [61] *and Mst1* [62], and known to be involved in IBD pathologies, were elevated at 7d and 14d post-CFA-IAI.

In the distal ileum, in addition to the increased transcript for the *Mptx1*, a strong and sustained response of enterocytes was supported by increases in the transcription factor *Hoxa9* [63], the amino acid transporter *Slc7a14* [64], the tight junction protein *Cldn8* [65], the anti-microbial Lysozyme *Lyc2* (*Lyzl-1* [66]), and the *Rdh7* gene, for retinoic acid metabolism [67]. Downregulated expression was seen for epithelial cell specific genes, involved in glucose transport and uptake, *Gpr17* [68], *Slc2a2* [69] and *Slc5a4* (*Sglt3*) [70].

The most profound transcriptional response to CFA-IAI was seen in the distal colon with decreased mRNA levels for a wide range of genes (**Figs. S3C** & **S4C**). Downregulated transcripts were seen for genes involved in regulation of intestinal immune responses, including the immune cell infiltration-related *Serpine1* [71] and the transcription factor *Atf3* [72, 73]. Several of the modified transcripts also point to cell-specific responses in the colon including the epithelial cell-associated genes *Btnl8* [74], *Fabp1* [75], *Prkg2* [76], *Car1* [77] and *Dmbt1*[78]; the fibroblast/myofibroblast associated genes *Cxcl11* [79], *Nr4a1* [80], and *Tbx5* [81]; as well as the enteroendocrine cell gene *GcG* [82]. Small, but significant increases were also seen for the transcription factor *EyA1* [83], which is implicated in the activation of cell proliferation and EMT in colon cancers.

Pathway and biological process allocation of DEGs using GO enrichment

To assign a functional significance of modified gene transcripts within the context of cellular pathways in synovium and intestinal tissues, GO enrichment analyses was performed using the KEGG pathway database. Individual pathways were further assigned to the following six biological processes listed in that database: Metabolism, Cellular Processes, Genetic Information Processing, Environmental Processing, Immune System and Nervous System. Note that all gene sets with a log FC value of <-0.3 and >+0.3, and an adjusted p-value <0.05, were included. The data are displayed in dot plots for synovium (**Figs. S5** & **S6**), proximal ileum (**Fig. S7**), distal ileum (**Fig. S8**) and distal colon (**Fig. S9**) and are also summarized in Venn diagrams (**Figs. 7** & **8**) Following CFA-IAI, a large number of pathways were activated in synovial tissue (**Figs. 7A** & **S5A**) (i.e., 45, 40 and 37 at 3d, 7d and 14d, respectively) or suppressed (i.e. 22, 32 and 6 at 3d, 7d and 14d, respectively). As expected from previous reports of the CFA model [34, 36], the adjuvant produced robust and persistent immune and inflammatory reactions in the synovium. Activated pathways included “NK cell mediated cytotoxicity”, “Neutrophil extracellular trap formation”, “Th1 and Th2 cell differentiation”, “Th17 cell differentiation” and “B cell receptor signaling” pathways at 3d, 7d, and 14d post-CFA-IAI. This was accompanied by a stimulation of “Toll-

like-receptor”-, “C-type lectin-” “IL17-” and “NOD-like”-immune cell signaling characteristic of immune cells. Other inflammation-related pathways such as of “cytokine–cytokine receptor interactions”, “chemokine signaling” and “NF-kB signal transduction” were also stimulated. Throughout the post-CFA period examined, a range of other pathways were suppressed, such as the Hippo pathway [84, 85], which can lead to induction of cell division and the suppression of apoptosis by PPAR signaling. This would be expected to interfere with control of the inflammatory response to TNF-α in synovial cells [86]. Other notable adjuvant-activated responses were seen in lysosomal, phagosomal, apoptotic, and necroptotic pathways, while neuronal system pathways such as “axon guidance” and “glutamatergic synapse function” were suppressed. By comparison, PBS-IAI resulted in a very minimal response in the synovium. The only modified pathways post-PBS-IAI that showed overlap with those modified by CFA-IAI were “heparan sulfate biosynthesis”, “RNA polymerase”, and “tryptophan metabolism” at 3 d and “neuroactive ligand-receptor interaction” and “HIF-1 and calcium signaling” pathways at 14d. There was a lack of immune or inflammation related pathways changed by PBS. This is in contrast to what was expected and previously shown as a mild sham-IAI response in the clinical setting for sham injection[87] or joint space lavage[88].

The corresponding GO analyses of intestinal tissues **(Figs. 8 & S6-S8)** showed fewer affected pathways than those identified in the synovium. As expected from the extensively downregulated transcriptome (**Figs. 4-6**) after CFA-IAI, many of the intestinal pathways were suppressed, most notably those associated with the immune system. In the proximal ileum, “Th1 and Th2 cell differentiation”, “Natural killer cell mediated cytotoxicity”, “Th17 cell differentiation”, and “Antigen processing and presentation” were suppressed over the entire experimental timeline. In the distal ileum, the “Intestinal immune network for IgA production” and the “Antigen processing and presentation” pathways were suppressed at 7d and 14d. These immune pathways were also suppressed in the distal colon, together with “B cell receptor” and “T cell receptor-signaling, and “Leukocyte trans endothelial migration”. Transcripts for a range of metabolic pathways and signaling pathways were also decreased in both the ileum and colon.

A comparison of pathway-specific responses between synovial and intestinal tissues, is shown in **Fig. 9.** Although many of the same pathways were affected, activation responses in the synovium gave corresponding suppression responses in the intestinal tissues, and this was particularly evident during the peak joint inflammation responses at 3d and 7d. This, together with the DEG data, confirms a generalized ‘silencing’ of inflammatory and immune reactions in the intestine post-CFA-IAI. This likely constitutes a shielding response to maintain intestinal barrier function in the presence of an acute innate immune and inflammatory insult at a remote tissue site.

<u>Effect of IAI CFA on intestinal immune cells and mucin metabolism.</u>

To test for alterations in intestinal immune cell population, such as macrophages and T-cells, we performed IHC analyses of sections from Swiss-rolled ileum and colon using anti-CD68 for macrophages, anti-CD4 and anti-CD8 for resident T cells (**Figs. 10A-C** and **S10-S12**). In healthy tissue, CD68+ macrophages were

almost exclusively located in the lamina propria of the ileum and the colon, and there was no change in their abundance or localization along the ileum. However, in the colon, at 3d post-CFA-IAI, transient increases in CD68+ve cells surrounding crypts and interspersed between enterocytes along the villi was seen (black arrows, **Fig. 10A**) was seen. This acute buildup of macrophages in the colon was further supported by increased transcript abundance of macrophage-specific genes *Trem2*[89] and *C1qc*[90] (**Fig. 10D**).

CD4+ T cells were distributed along the villi in the ileum and additionally in the apical regions in the colon, likely expressed by the intraepithelial lymphocytes[15] (IELs), which were unchanged during the post-CFA period (**Fig. 10B**). In naïve intestinal tissue, the anti-CD8 also stained predominantly IELs **(Fig. 10C)**. However, at 3d and 7d post-CFA-IAI, increased staining of such cells in the apical part of the villi was seen in many regions throughout the ileum and the colon. In addition, at 7d CD8+ve populations had also accumulated in the crypts (**black arrows**, **Fig. 10C**). By 14d, however, the abundance of these T-cells and their locations had returned to those seen in naïve intestinal tissues.

In keeping with the protective response of intestinal tissues to knee joint inflammation, there were no changes in cell proliferation (Ki67 staining) in any intestinal region (**Fig. S13**). We also observed increased secretion of mucins in the distal ileum, during the acute response phase at 3d & 7d, shown by Alcian blue staining (**Fig. 11A**), and supported by increases in transcript abundance for the gel-forming mucins *Muc2* and *Muc5b[91]* (**Fig. 11C**). Furthermore, histochemical staining with O-linked oligosaccharide specific lectins (GSL I, MAL II, and UEA) showed an increased reactivity in mucus with the GSL I (specific for terminal α-N-acetylgalactosamine or α-N-galactose residues)[92] in the distal ileum at 3d post-CFA-IAI (**Fig. 10B**). There were no detectable changes in staining with MAL II (terminal α-2,3 sialic acid) or UEA (α-linked fucose) (**Fig. S14**). Modulation of mucin glycosylation in response to the joint inflammation was further underlined by altered mRNA transcripts for multiple glycosyltransferases, including *St6galnac1* (**Fig. 10C**), the major sialyltransferase in goblet cells, known to be induced by microbial pathogens and critically important for maintaining mucus integrity [93].

<u>Effect of CFA-IAI on Digestive Functions and Microbiome Composition</u>

Based on our RNASeq data, several digestive system pathways throughout the different regions of the intestine were affected by the inflammatory response of the knee joint. For example, transcripts encoded by genes associated with 'mineral absorption' were modulated in all 3 regions of intestine and were largely decreased compared to pre-treatment. The distal colon showed suppression of the fat digestion pathways, with decreases in expression of 4 associated genes **(Fig. 11A).**

Notably, there was no evidence for development of dysbiosis in the model. The fecal microbiota from the distal ileum and colon were minimally altered in response to the knee joint inflammation and respective intestinal cell responses. Alpha diversity for within-group comparison was unaltered, as shown by evenness ($p = 0.697$), Shannon index ($p = 0.997$), and Simpson index ($p = 0.998$). Relative bacterial abundance (>1%) for the distal ileum and the colon (**Fig. 11B**) at the phylum level showed a slight shift from Naïve to 3d, 7d and 14d post-CFA-IAI. Amongst this shift, there was a decrease in *Romboustia* in the ileum at 3d post-CFA, followed by an increase

at 7d and a return to naïve levels by 14d. *Lactobacilus* showed the opposite shift with an increase by 3d, decrease by 7d and a return to naïve levels by 14d. This change in abundance supports a mild and importantly, a limited transient response of the microbiome when acute inflammation in the joint peaks at 7d post-CFA-IAI. Due to the observation of a transient change in mucus layer 16S data were mined for the abundance of mucin-degrading bacteria (*Akkermansia, Alistipes*) and sialic acid cleaving bacteria (*Bifidobacterium*) (**Figs. 12** & **S14**). Apart from the appearance of a low levels of *Akkermansia* in the feces from distal ileum and distal colon post IAI of CFA, the joint inflammation had not detectable effect on the other two species.

DISCUSSION

In this study we present novel data on coordinated cell and molecular biological changes in the synovium and intestinal tissues in the acute CFA-induced knee joint inflammation model. Due to its reproducibility and rapid inflammation responses in the injected joint, this model has been used extensively for preclinical efficacy testing of a wide range of anti-inflammatory [94, 95] and analgesic [96-99] RA drugs. A number of these studies have chosen the inflamed synovium as a target, with a focus on the cytokines and the NFκB signaling pathway [100-103]. This model has also been used in several studies to examine the effect of joint inflammation on the gut microbiota [37, 96] supporting the existence of a “cross-talk” between joint and remote tissues like the gut. However, only limited data of the cell biological responses in the intestinal barrier tissues and innate immune cell populations are currently available. Our data reported here provide a detailed and comprehensive assessment of cellular and molecular biological changes underlying inflammatory responses during the formation of a synovial pannus and corresponding intestinal responses.

Our data confirm an early and robust response of the joint to the adjuvant at 3d and 7d post-CFA-IAI. In addition to measurements of joint swelling, we showed joint effusion by elevated levels of serum albumin and serum-derived bikunin-containing complexes[39] in the synovial fluids. The latter include the liver-derived IαI and the acute phase proteoglycan PαI, which are known to accumulate in synovial fluids in osteoarthritis and rheumatoid arthritis[104-106]. In this context, it is notable that in an inflammatory tissue environment, bikunin-containing complexes can act as donors of their chondroitin sulfate bound-heavy chains for transfer to hyaluronan in the presence of TSG6[107-110]. This results in a crosslinked extracellular hyaluronan network[111] that is permissive for leukocyte cell adhesion[112, 113]. Generation of such a matrix in joint tissues is likely involved in the acute phase of this model, since RNASeq data show a ~2-fold increase in mRNA levels for TSG6 (*Tnfaip6*) as well as hyaluronan synthase 2 (*Has2*), at 3d post CFA, with both genes returning to pre-inflammation levels by 7d (data not shown). Moreover, following the acute inflammatory response, the perimeniscal synovium was transformed into a hyperplastic tissue with a fibrotic matrix that was extensively populated by myeloid cells, but no significant presence of T-lymphocytes was detected.

Recent studies of RA patient-derived synovial biopsies have identified subgroups of synovial “pathotypes” [114, 115]. Interestingly, our data suggest that CFA-IAI results in formation of the mixed myeloid/fibroid, but not the lymphoid pathotype. The former is reported to be treatment-resistant to many current DMARDs contributing

to persistent “low joint disease activity” of many RA patients. This underscores the utility of this model to develop novel therapeutic approaches targeting joint tissue destruction in inflammatory arthritis. The development of a macrophage-rich synovial tissue is supported by the RNASeq based pathway analyses. Firstly, post-CFA activation of signaling pathways, including Notch, JAK/STAT, NF-κB, and MAPK [116], metabolic reprogramming, and increased glycolytic pathways are known to control macrophage polarization towards the pro-inflammatory phenotype in RA. In addition, biosynthetic pathways for arginine, a substrate for the inducible nitric oxide synthase (iNOS) in macrophages, indicates elevated production of nitric oxide (NO) and citrulline, both of which are key metabolites in the inflammatory pathogenesis of RA [117, 118]. Notably, persistent activation of the “lipolysis in adipocytes", fatty acid metabolism, as well as cortisol synthesis and secretion pathways seen in our studies have also been reported to be a markers for a highly pro-inflammatory synovial subtype in OA and RA patients[119-121]; and is consistent with turnover of the sub-synovial adipose tissues induced by joint inflammation.

The development of a pro-inflammatory macrophage-rich synovium is also likely responsible for epiphyseal and metaphyseal periosteal surface pitting present at 3d and 7d post-CFA, in regions that were invaded by the hyper-proliferative pannus[122]. A transient downregulation was present of propanoate, a short-chain fatty acid known for its role in anti-inflammatory macrophage polarization, and specifically in suppression of osteoclastic activities in particle-induced aseptic osteolysis[123-125]. Re-establishment of a smooth periosteal surface by 14d supports the conclusion that the specific macrophage-mediated inflammatory joint tissue responses in the CFA-model are self-limiting, which is further supported by a robust increase in transcripts for oxidative phosphorylation[126]. This pathway plays a critical role during the polarization of the macrophage phenotype from a pro-inflammatory, glycolysis-dependent type to the anti-inflammatory type[127, 128]. This together with a mineralization response seen in the post-CFA reactive periosteum would account for the reversal of periosteal surface damage. On the other hand, trabecular bone recovery did not occur in keeping with published data[129], as remodeling cycles in this compartment are long compared to the 14d time frame of our experiment with timing of osteoclast recruitment to this site, lifespan of osteoclasts, and their lifespan in rats is on the order of months[130].

On the other hand, there was no attenuation of the increases in cytokine and chemokine signaling pathways or activated T and B cell characteristic pathways, suggesting that even though several inflammatory responses in the joint are transient, many of the CFA-induced cellular and metabolic changes are in keeping with an irreversible modification of the synovial tissues. Moreover, additional challenges to such joints could lead to more severe innate responses and eventually lead to activation of the adaptive immune system and development of a chronic inflammatory arthritis. It should also be noted that only a few DEGs during intestinal responses to CFA-IAI overlapped with those detected for the synovium. We show that *Nos2, S100a9, Cxcl1, Ccl2, and Lcn2* increased in the synovium and decreased in the intestine, whereas *C1ql3* and *Serpine1a* were decreased in the synovium and increased in the intestine.

Gross evaluation by histological assessment of the ileum and colon revealed no detectable changes in the overall appearance of the tissue during the 2-week post-CFA period. This included intactness of intestinal villi, no increases in vascularization of the submucosa (data not shown), and unchanged cell proliferation indices, as determined by distribution and abundance of Ki67+ cells. There were no marked changes in the abundance of goblet cells throughout the ileum and colon, with only a transient change in mucus secretion in the distal ileum. In addition, the microbiota composition was minimally affected, with only a mild and transient response during peak joint inflammation (7d post-CFA-IAI) and normalized by the 14d time point. Moreover, using immunohistochemistry, we detected only transient alterations in immune cell abundance, including increased CD68+ macrophages in crypts of the colon and increased CD8+ T cells at the apical surface of villi in the ileum. Moreover, such changes occurred in sporadic regions of the intestinal compartments.

Our data contrast with the widespread intestinal manifestations observed in the chronic rodent models of inflammatory arthritis induced by immunization with type 2 collagen[131]. In fact, our bulk RNASeq data analyses from the proximal and distal ileum and the distal colon indicate a widespread "allostatic" response[41] to the CFA-induced inflammation and pain stressors in the joint. We observed significant suppression of transcriptomes compared to levels seen in those tissues pretreatment and included downregulation of genes in multiple pathways controlling pro-inflammatory signaling, immune activation, and cellular metabolism. Such broad “gene silencing” might be expected as a response to prevent chronic damage to the essential functions of the intestine, including nutrient digestion and absorption, as well as defense against bacterial invasion and support microbial symbiosis. In particular, our data showed containment of cytokine and chemokine signaling and inhibition of the oxidative phosphorylation (OXPHOS) and PPAR-γ pathways throughout the post-CFA-IAI period. OXPHOS and mitochondrial function are fundamental for metabolic homeostasis of all cell types of the intestine and imperative to a functional barrier, however, enhanced flux through this pathway occurs when increased ATP is needed by immune cell during their activation and cytokine production. Furthermore, mitigation of reactive oxygen species (ROS), generated as by-products of enhanced OXPHOS, would prevent their damaging effect on intestinal function [132], including disrupted barrier function, dysbiosis, and impaired immune responses [133, 134].

Genes in a second pleiotropic signaling pathway, the PPAR-γ pathway, extensively studied in colon cancers[135] were also downregulated in the post-CFA-IAI period, and this occurred both in the intestinal tissues and the synovium. In the context of the latter, this activity is pivotal in regulation of adipose tissue metabolisms, and its downregulation is a hallmark of inflammatory responses [136], which is consistent with loss of adipocytes in the myeloid/fibrotic induced synovium from CFA-IAI. A protective effect of its downregulation in the intestinal tissues might be attributed to silencing its cross-signaling with a range of other signaling pathways, including NFκB, Notch [137], JAK/STAT [138, 139], MAPK [140], and Wtn/β-catenin [136]; some of which were also found to be downregulated in the post-CFA intestines. In summary, we provide, for the first time, data on temporally coordinated cellular responses between joint tissues and the intestine following an acute inflammatory insult by ICFA-IAI into the knee joints of skeletally mature rats. Additional application of spatial transcriptomics to depict anatomical location of transcriptomic alterations in the intestinal barrier, together with ATACSeq[141] to identify

regions of the genome that are accessible or blocked would further clarify regulatory mechanisms that could serve as therapeutic targets locally or systemically, during inter-organ communication in chronic arthritis.

Transmission of signals between diseased tissues and the gut has been postulated for a wide range of disease conditions, but the molecular and cell biological mechanisms remain largely undefined, except for the much-studied bidirectional pathway between the brain and the intestine[142], which includes cytokine, chemokines, migrating or circulating immune cells, and microbiota-derived metabolites. More relevant as a potential mediator of intestinal responses to joint inflammation is the enteric nervous system (ENS), which is a highly conserved network of neuron and glial cells located throughout the intestinal tract [143]. In this study, it likely was indicated in the development of gut inflammation and dysbiosis in response to psychological stressors [144], such as pain-induced anxiety [145], and could also underlie the presence of the allostatic tissue response [146]. Indeed, our preliminary data suggest a likely neurobiological involvement in the intestinal response to joint inflammation induced by CFA-IAI (*data not shown*). Additional mining of our transcriptomic data sets indicated modulation of serotonergic pathways, glutamatergic synapse activity, synaptic vesicle recycling, and retrograde endocannabinoid signaling throughout both ileum and colon. Select transcripts of genes with known neurobiological effects, such *Gdf15*, *Atp1a3*, and *Mdga2* [147] were activated in the ileum [147-149], suggesting that in future mechanistic studies for joint-gut communications, potential Vagus/ENS responses should be assessed.

In conclusion, since the CFA-induced joint inflammation model does not develop chronic systemic inflammatory conditions, it remains to be established whether multiple or chronic or consecutive allostatic responses of the intestinal tissue to joint inflammation will result in 'allostatic overload' [150]. Such conditions might ultimately lead to pathological disruption of the intestinal barrier function with dysbiosis as reported in both inflammatory bowel disease [151] and might also underlie the intestinal dysfunction reported in both patients and animal models of inflammatory arthritis [2, 21].

Methods

Animal husbandry. All procedures used in this study were approved and in compliance with the Institutional Animal Care and Use Committee (IACUC) at Rush University Medical Center. A total of 44 male Sprague Dawley (SD) rats (375-400g, approximately 4 months old, Envigo) were pair-housed in cages (polysulfone,19 × 10.5 × 8 in.) in the animal facility maintained at 22°C and 35%-55% humidity with a 12-hour light/dark cycle (light 7 AM-7 PM). Standard laboratory-grade rodent chow (Teklad Global Rodent Diet 2018, 18% protein; Envigo) and water were provided *ad libitum* (**Fig. S1**).

Induction of knee joint inflammation with Complete Freund's adjuvant. Experiments were initiated after a 2-week acclimatization period to minimize effects of stress conditions during transport and housing, severity, and inter-group inconsistency in disease responses. Intra-articular injections (IAI), blood collections and sacrifice were all conducted at the same time of day, i.e. between 9AM-noon. Rats were assigned to one of three study groups

(n=6 rats/group): Naïve (no intra-articular injection), Complete Freund's Adjuvant (CFA, 10mg Mycobacterium tuberculosis, 1.5ml Mannide monooleate and 8.5ml paraffin oil, InvivoGen) and vehicle controls (1xPBS). IAI was administered using a 29G insulin syringe lateral to the patellar tendon as a single 50 µl dose bilaterally, into the left and right knee joints. On day 0 (day before IAI) and days 3, 7 and 14 post-IAI, under 3% isoflurane anesthesia, rats were weighed and knee and ankle diameters measured using calipers in the medial-lateral orientation. Non-fasted tail-vein blood was collected into a BD Vacutainer SST tube per rat. Blood was allowed to clot at room temperature. Serum was separated by centrifugation at 3,000 rpm for 18 min at 4°C (~250 µL per bleed) and 40 µL 10X proteinase inhibitor (PI) cocktail (cOmplete, Mini, EDTA-free Protease Inhibitor Cocktail) was added prior to storage at -80°C.

Sacrifice, tissue collections and sample storage. All rats were euthanized by CO_2 inhalation and secondary cervical dislocation. At sacrifice, bilateral hind limbs were collected from all rats and disarticulated at the hip. From right hind limbs, synovial fluid was collected by opening the joint capsule while the knee was carefully flexed. The synovial fluid from the right and left knee joints was combined from each individual rat. The joint cavity was rinsed twice with 150µL 1xPBS and collected into sterile microcentrifuge tubes. Lavages were centrifuged at 3,000 rpm/805 g for 10 min at 4°C to remove cells and debris. Supernatants were stored at -80ºC until further analyses. To minimize difficulties in result interpretation due to potential sampling errors of synovium from the rat knee joint, synovial tissues were collected from the readily identifiable peri-meniscal sites and the patellar fat pad, placed into RNALater and stored at -80ºC for RNA-Seq analyses. From the right disarticulated hind limbs, femora and tibiae were fixed in 10%NBF for 7 days and then moved to 70% EtOH until they underwent micro-computed tomography scanning (Scanco 50, Switzerland). Left intact knee joints were isolated by making transverse cuts 1.5cm proximal and distal to the joint and then fixed in 10% neutral-buffered formalin (NBF). Joints were decalcified in 20% EDTA, cut at midline sagittally and paraffin processed, embedded and sectioned at 6µm slices for histology. Right intact knee joints were dissected open using a fresh scalpel. Synovium and patellar fat pad were excised into RNALater (Invitrogen) and froze at -80°C until RNA extraction. Ileum and colon were dissected and fecal contents expressed into sterile 1.5ml microcentrifuge tubes from both gut segments and stored at -80ºC for 16S microbiome analyses. The remaining tissues were either rinsed in ice-cold 1xPBS, transferred to RNALater and stored at -80ºC for RNASeq, or placed into Modified Bouin's fixative and prepared into Swiss rolls [152] for paraffin embedding, and sectioned at 6µm thickness for histology and immunohistochemistry (**Fig. S1**).

Histological and immunohistochemical evaluation of joint and intestinal tissues. Sagittal sections from knee joints were stained with Hematoxylin/Eosin, anti-CD68 (Abcam, Ab283654; 1:100) or anti-CD4 Abcam, Ab237722 1:2000). Sections of intestinal Swiss rolls were stained using the Alcian Blue Kit (Vector Labs, H-3501), anti-CD68 (1:100), anti-CD4 (1:2000), anti-CD8 (Abcam, Ab237709, 1:500) or anti-Ki67 (Invitrogen, MA5-14520; 1:100), Invitrogen, MA5-14520) or the following biotinylated lectins (all from Vector Labs), *Griffonia Bandeiraea*

Simplidifolia Lectin I, (GSL I, B-1105-2), *Maackia Amurensis Lectin II* (MAL II, B-1265-1) and *Ulex Europaeus Agglutinin I* (UEA, B-1065-2). Prior to histochemical staining, antigen retrieval was performed using Tris/EDTA (Abcam, ab93684), and sections were blocked with normal goat serum (Vector Laboratories, S-1000). Immuno- and lectin reactivities were developed using the ABC kit (Vector Laboratories, PK-7100) and the DAB kit (Vector Laboratories, SK-4100). Methyl green (Vector Laboratories, H-3402) was used as a counterstain. Slides were imaged using an Olympus VS200 Scanner.

Western blot characterization of affinity-purified antibodies to mouse bikunin. A synthetic peptide of mouse bikunin was synthesized and conjugated to Keyhole Limpet Hemocyanin (KLH), via a non-authentic cysteine residue at the C-terminal end, for production of a polyclonal antibody in a rabbit (Mimotopes, Australia). The anti-serum (from rabbit A) was affinity purified using the immunizing peptide (Genscript, USA) covalently coupled via the cysteine residue to SulphoLink Coupling Resin (Thermo Scientific Pierce, UK), according to the manufacturer's instructions. Purified IgG fractions were pooled, concentrated and stored in aliquots at -20ºC; the affinity purified antibody is designated ap_A_mBikunin. A Western blot of mouse serum treated with/without chondrotinase ABC lyase or NaOH was used to characterize the affinity purified antibodies. Here 1.25 µL of mouse serum was incubated with/without 0.1 U Chondroitinase ABC lyase (from *Proteus vulgaris*; Sigma Aldrich) for 2 h at 37˚C or 0.1 M NaOH for 10 min at RT after which 1.0 µL 1 M HCl was added to the NaOH-treated samples. Reactions were stopped by adding 5 µl of 5X sample loading buffer; 12 µl of each reaction was run on a NOVEX 4-20% Tris-Glycine gel. Proteins were transferred to a nitrocellulose membrane in Tris-Glycine transfer buffer. Blots were blocked for 1 h with 5% (w/v) dried milk in PBS/0.05% (v/v) Tween-20 (PBST), washed briefly in PBST and then incubated with ap_A_mBikunin (diluted 1:500 in PBST with 5% (w/v) dried milk) overnight at 4˚C. After washing in PBST the membrane was incubated with IRDye 800CW-conjugated goat anti-rabbit IgG secondary antibody (1:5000 in PBS; LI-COR Biosciences Ltd) for 1 h at room temperature, washed as before and visualized using an Odyssey CLx imaging system (LI-COR). The species detected by the antibody are indicated to the right in Fig. S2.

Western blot analyses of serum and synovial fluid bikunin. Commercially available mouse serum, which was processed the same as experimental rat serum, was included in each western blot as an internal standard. Serum samples were thawed on ice and diluted 1:1 with 50mM ammonium acetate pH 7.0 containing 1XPI and debris removed with a 0.45µM filters. 150µL of sera were desalted using MicroCon 3 filtration units (at 12,500 rpm in a microfuge for 15 min) and retentates washed once with 450µL 50mM ammonium acetate, pH 7.0. Desalted proteins were collected from the membrane with 500µL ammonium acetate, pH 7.0. Portions (containing 7.5µL equivalents of serum) were incubated at 37°C for 2 hrs. with or without 5mU of protease-free chondroitinase ABC lyase (Chondroitinase ABC protease free).

Synovial fluid samples were thawed on ice, diluted to 450µL with 50mM ammonium acetate, pH 7.0 containing 1XPI, clarified by centrifugation at 12,000 g at 4°C for 15 min, and desalted using MicroCon 3 filtration

units as described above for serum samples. The retentates were recovered in 200µL 50mM ammonium acetate, pH 7.0 and 100µL portions were incubated at 37°C for 2h with or without 5mU of protease-free chondroitinase ABC.

Sera and synovial fluid samples were speedvac dried and analyzed by gel electrophoresis and western blot. Chondroitinase digestion buffer was removed by speedvac evaporation. Samples were dissolved in Tris-glycine SDS sample buffer (Novex, AMS.E1028-02) containing 100µl of 0.5mM DTT, heated at 90°C for 5 min before electrophoresis on SDS gels (Invitrogen Novex WedgeWell 4-12% Tris-Glycine). Separated proteins were electro-transferred on ice (250V, 302µA for 45 min and 150V, 297µA for 15 min) to 0.45µm nitrocellulose membranes (BioRad) and these were incubated with affinity purified anti-bikunin antibody (ap_A_mBikunin). Antibody reactivity with inter-α-inhibitor (IαI) and pre-α-inhibitor (PαI), bikunin, and bikunin core protein[108] was characterized (**Fig. S2A).** The Western blotting procedure (in **Fig. S2 B,C**) was performed as previously published [153]. Chemiluminescent images were recorded using iBright1500 Instrumentation and further analyzed using ImageJ software. Data are shown as integrated pixel density (IPD) relative to bikunin present in standard mouse serum (Sigma Aldrich m595).

Micro-computed tomography analyses of femurs. Micro CT scanning was completed using a Scanco µCT50 (Switzerland). Right femurs were scanned using 70kVp, 114µA, 500ms integration time, and 10µm voxel size. The region of interest (ROI) for trabecular and cortical bone analyses started just proximal to the distal femoral growth plate and continued 2 mm proximally into the metaphysis. The trabecular and cortical bone compartments were analyzed separately using thresholds of 200 and 1000, respectively. Cortical and trabecular bone parameters were measured using the manufacturer's software. Periosteal reaction was noted when present and analyzed separately from the cortex using the same threshold values.

Bulk RNASeq analyses of synovium and intestine. To obtain reproducible and high-quality yields of RNA from synovium, tissues were harvested from right and left knees and pooled from n=3 rats, then analyzed as a single sample. Distal ileum and colon tissues in RNAlater were thawed on ice and 1cm pieces were dissected out (including villi, submucosa, and smooth muscle layers) using transverse cuts. The number of intestinal tissue replicas to provide sufficient DEG detection power was determined as previously described [154].

Using previously published methods [155] RNA was extracted and purified from all tissues, samples with RIN numbers $\geq$7 were reverse transcribed into cDNA, PCR amplified with primers CS1_515F and CS2_806R followed by library preparation. Bioinformatic analyses of sequencing data was carried out as follows: Raw reads were trimmed to remove Truseq adapters and bases from the 3' end with quality scores less than 20 using cutadapt[156]; trimmed reads shorter than 40bp were discarded, and were then aligned to the mRatBN7.2 *Rattus norvegicus* (Norway rat) reference genome using STAR[157]. The expression level of ENSEMBL genes was quantified using featureCounts[158] and the resulting expression counts were used to compute differential expression statistics with edgeR[159, 160]. Normalized expression was computed as $\log_2$ counts per million

(CPM), including a TMM normalization and batch effect correction. In all cases p-values were adjusted for multiple testing using the false discovery rate (FDR) correction of Benjamini and Hochberg[161]. Volcano plots were generated within the R programming language. DEG (Differentially Expressed Genes) with an absolute Log_2FC (Log Fold Change) <+2 or <-2 and a q value of less than 0.05 were assigned to specific pathways using the KEGG and further grouped under seven functional categories: Metabolism, Cellular Processes, Genetic Information Processing, Environmental Processing and Immune System

16S microbiome analyses. Details have been described by us previously [6]. Briefly, DNA was extracted from fecal samples using a Maxwell RSC48 device (Promega), with bead-beating implemented off-instrument. Microbial community structure was characterized by DNA extraction, PCR amplification and sequencing of 16S ribosomal RNA gene amplicons[162]. Microbiome bioinformatics was performed with QIIME2 2021.11[163]. Raw sequence data were checked for quality using FastQC and merged using PEAR[164]. Merged sequences were quality filtered using the q2-demux plugin followed by denoising with DADA2 [165] (via q2-dada2). Primer adapter sequences were removed using cutadapt algorithm[156]. Alpha-diversity metrics (observed features[166], Shannon Index[167], Simpson's Index [168], and Pielou's Evenness) and beta diversity metrics were calculated using q2-diversity after samples were rarefied to a depth of 59,000 sequences per sample. Taxonomy was assigned to ASVs using the q2-feature-classifier[169] classify-sklearn naïve Bayes taxonomy classifier against the SILVA 138 99% reference sequences database[170]. Differentially abundant genus level taxa between pairwise groups were identified using the compositional centered Log-ratio Kruskal Wallis (CLR-KW) algorithm. Adjusted P-values (also known as q-values) were generated using the Benjamini–Hochberg method[161].

Statistical Analyses for Bone Data. Control and test rats from 2 separate cohorts (one in the summer and one in the winter) were included. For the trabecular parameters, we observed a cohort effect so we express all test results normalized to the mean of the cohort-specific control animals. Significance was assessed using one-way analyses of variance (ANOVA) for group effects with Bonferroni post hoc tests. All results are reported as means ± standard deviation and individual data points are shown. The statistical testing was performed with commercially available software (SPSS v.19 for Windows, Chicago, IL).

Acknowledgements

We would like to thank Dr. Georgia Papavasiliou (Illinois Institute of Technology) and Dr. Joseph Reynold (Rosalind Franklin University) for their insightful discussions on intestinal immunology and therapeutic target discovery during the progression of this project; Dr. Stefan Green for his input in study design and genomic analyses; and Rylan Martin for technical support. Funding for this project is from the Orthopedics Departmental Fund RUMC (MMM), the Katz/Rubschlager Endowed Chair at RUMC (AP), and Versus Arthritis, UK Grant 22277 (AJD and CMM).

Figure 1. Analyses of knee joint responses to IAI of CFA or PBS

(A) At time of sacrifice the diameters of knee joints were measured as described in the Method from rats without treatment (Pre-Treat), after IAI of PBS and 3 days (3d), 7 days (7d) and 14 day (14d) post-CFA. CFA-IAI knees showed significant swelling at all three time points, when compared to pre-treatment or PBS-IAI (Bars= $p < 0.001$, 1-way ANOVA). **(B,C)** Abundance of bikunin species in synovial fluids (**B**) and sera (**C**) were determined by western blotting as described in the Methods and Supporting Information **Fig. S2**. Note that for pre-treatment (Pre-Treat) and PBS groups, the measurements at 0d and 14d, respectively, were combined since no significant differences were observed between those two groups (general linear model 0d v. 3d v. 14d PBS serum $p = 0.226$). Coronal FFPE sections of pretreatment and 14d IAI CFA knee joints were stained with H&E (**D** & **G**), anti-CD68 (**E** & **H**) or anti-CD4 (**F** & **I**). The CFA-induced synovial hyperplasia enriched in collagenous ECM and infiltrated by CD68+ macrophages is indicated by black arrows and the swollen patellar tendon by (*). M=meniscus, Fc=femoral condyles, TP=tibial plateau, S=synovium, PT= patellar tendon.

Figure 2. µCT analyses of femoral metaphyses and epiphyses following IAI-CFA

(A) 3D rendering of the distal femoral metaphysis and epiphyses show cortical pitting at 3d in the proximal region of the patellar groove with pitting extending to the epiphyseal and metaphyseal regions at 7d (yellow arrows). There is a cortical regenerative response visible by 14d**. (B)** Representative 2D slices through the distal metaphysis adjacent to the patellar groove show the typical appearance of a periosteal mineralization response (red arrows) in the antero-mediolateral region of the femur. This was present after CFA-IAI in (n=7) 7d and (n=2) 14d rats. **(C)** 3D renderings of the metaphyseal trabecular bone adjacent to the cortical bone showed decreased bone volume by 7d post-CFA, which also had recovered by 14d. Scale bars all panels = 1mm. **(D)** Representative 3D renderings of the isolated cortical periosteal mineralization response in the proximal femur at 7d and 14d post-CFA-IAI. The spatial distribution of the cortical pitting at 7d shown in panel A matches the periosteal reaction at 7d and is corrected by 14d post-CFA. **(E)** Bone volume fraction (BV/TV) normalized to pre-treatment group. BV/TV decreases with CFA-IAI compared to both pre-treatment and PBS-IAI. *=$p<0.05$, **=$p< 0.01$, ***=$p< 0.001$.

Figure 3. Differentially expressed genes in synovial tissue at 3d, 7d and 14d after IAI of CFA or Saline.

(A) Heat map illustrating overall shifts in transcriptomic landscape after IAI-PBS (grey bars) or CFA (black bars), relative to d0 (yellow bar). **(B-F)** Statistical significance (p-value) vs. the magnitude of change (log FC) were calculated as described in the Methods and DEGs are summarized in volcano plots**.** Log FC thresholds of −2 and +2 and an adjusted p-value threshold of 0.05 are delineated by the dotted lines. Upregulated transcripts are on the right, downregulated transcripts are on the left of the lines, and statistically significant DEGs are above the horizontal lines. **Grey dots =** not significant, **Blue dots** = Genes $p<0.05$, **Red dots=** Genes $p < 0.05$ and 2-fold change.

Figure 4. Differentially expressed genes in proximal ileum tissue at 3d, 7d and 14d after IAI of CFA.
(A) Heat maps illustrating overall shifts in transcriptomic landscape after IAI of CFA relative to d0. Each vertical column corresponds to tissue from a single animal. **(B-D** CFA at 3d, 7 d and 14d respectively**)** Statistical significance (p value) vs the magnitude of change (log FC) are summarized in volcano plots using the log FC thresholds of −2 and +2 and P-values of 0.05 (dotted vertical and horizontal lines). **Grey dots =** not significant, **Green dots=** Genes 2-fold change, **Blue dots** = Genes p<0.05, **Red dots=** Genes p < 0.05 and 2-fold change.

Figure 5. Differentially expressed genes in distal ileum tissue at 3d, 7d and 14d after IAI of CFA.
(A) Heat maps illustrating overall shifts in transcriptomic landscape after IAI of CFA relative to d0. Each vertical column corresponds to tissue from a single animal. **(B-D** CFA at 3d, 7 d and 14d respectively**)** Statistical significance (p value) vs the magnitude of change (log FC) are summarized in volcano plots using the log FC thresholds of −2 and +2 and P-values of 0.05 (dotted vertical and horizontal lines). **Grey dots =** not significant, **Green dots=** Genes 2-fold change, **Blue dots** = Genes p<0.05, **Red dots=** Genes p < 0.05 and 2-fold change.

Figure 6. Differentially expressed genes in distal colon tissue at 3d, 7d and 14d after IAI of CFA.
(A) Heat maps illustrating overall shifts in transcriptomic landscape after IAI of CFA relative to d0. Each vertical column corresponds to tissue from a single animal. **(B-D** CFA at 3d, 7 d and 14d respectively**)** Statistical significance (p value) vs the magnitude of change (log FC) are summarized in volcano plots using the log FC thresholds of −2 and +2 and P-values of 0.05 (dotted vertical and horizontal lines). **Grey dots =** not significant, **Green dots=** Genes 2-fold change, **Blue dots** = Genes p<0.05, **Red dots=** Genes p < 0.05 and 2-fold change.

Figure 7. Venn diagram illustration of modified biological process in synovium.
Following **(A)** CFA or **(B)** PBS exposure. The numbers in individual circles indicate the total pathways activated (↑) or suppressed (↓) at each time point, and these are individually displayed and in color-coded KEGG-based grouping of "Biological Processes". Processes modified at two (3d/7d, 7d/14d, 3d/14d) or three (3d/7d/14d) times points are listed to the right of the Venn diagram and the number of affected pathways in each Process is shown in brackets.

Figure 8. Venn diagram illustration of modified biological processes in proximal and distal ileum and colon following CFA-IAI. Numbers in individual circles indicate the total pathways activated (↑) or suppressed (↓) at each time point, and these are individually displayed and in color-coded KEGG-based grouping of "Biological Processes". Processes modified at two (3d/7d, 7d/14d, 3d/14d) or three (3d/7d/14d) times points are listed to the right of the Venn diagram and the number of affected pathways in each Process is shown in brackets.

Figure 9. Comparisons of modulated pathways in synovial and intestinal tissue following CFA-IAI.

Activated pathways are marked with a red upward pointing arrow (↑) and suppressed pathways with a blue downward pointing arrow (↓). No change is indicated by a horizontal double arrow (↔). SYN= synovium, PI = proximal ileum, DI = distal ileum, Co= Colon.

Figure 10. Effect of CFA-IAI on macrophage and T cell responses in distal Ileum and colon

Adjacent FFPE-sections from proximal and distal regions of the ileum and colon were stained with (**A**) anti-CD68 to localize macrophages or (**B**) anti-CD4 and (**C**) anti-CD8 to localize T-cells. Black arrows indicate regions of increased reactivity post CFA. (**D**) DEGs typically associated with intestinal macrophages or T cells caused by CFA-IAI are summarized in the heat map. PI=Proximal Ileum, DI= Distal Ileum, PC= Proximal Colon, DC= Distal Colon.

Figure 11. Modified mucin secretion in distal ileum and colon following CFA-IAI. Adjacent FFPE-sections of Swiss-rolled ileum or colon stained with Alcian Blue (**A**) or the biotinylated GSI lectin (**B**) as described in the Methods. Brown= positive stain; Black arrows show the increased mucin secretion with enhanced GSI staining in the DI at 3d post IAI of CFA. Modified gene transcripts in the mucin biosynthesis pathways in proximal and distal regions of the ileum and the distal colon, which were affected by IAI of CFA are summarized in the heat map in panel (**C).** PI=Proximal Ileum, DI= Distal Ileum, PC= Proximal Colon, DC= Distal Colon.

Figure 12. Effects of CFA-IAI on genes in associated with digestive functions and microbiome compositions in distal ileum and colon. (A) Data were obtained from the DEGs from analyses of RNASeq data (see Figs. 3 & 5) and are shown as log fold changes ($p<0.05$) as a heat map. **(B** & **C)** 16S Amplicon Sequencing of Fecal Microbiome was performed as described in the Methods**.** Relative bacterial abundance (>1%) is shown for the distal ileum (DI, **B**) and the distal colon (DC, **C**) at pre-treatment, 3d, 7d and 14d at the phylum level. Individual phyla are color-coded and listed on the right.

References

1. Kalinkovich A, Livshits G. A cross talk between dysbiosis and gut-associated immune system governs the development of inflammatory arthropathies. Semin Arthritis Rheum. 2019;49(3):474-84. Epub 20190531. doi: 10.1016/j.semarthrit.2019.05.007. PubMed PMID: 31208713.
2. Scher JU, Littman DR, Abramson SB. Microbiome in Inflammatory Arthritis and Human Rheumatic Diseases. Arthritis Rheumatol. 2016;68(1):35-45. doi: 10.1002/art.39259. PubMed PMID: 26331579; PubMed Central PMCID: PMCPMC4789258.
3. Favazzo LJ, Hendesi H, Villani DA, Soniwala S, Dar QA, Schott EM, et al. The gut microbiome-joint connection: implications in osteoarthritis. Curr Opin Rheumatol. 2020;32(1):92-101. doi: 10.1097/bor.0000000000000681. PubMed PMID: 31724973; PubMed Central PMCID: PMCPMC6903327.
4. Hernandez CJ, Guss JD, Luna M, Goldring SR. Links Between the Microbiome and Bone. J Bone Miner Res. 2016;31(9):1638-46. Epub 20160726. doi: 10.1002/jbmr.2887. PubMed PMID: 27317164; PubMed Central PMCID: PMCPMC5434873.

5. Seely KD, Kotelko CA, Douglas H, Bealer B, Brooks AE. The Human Gut Microbiota: A Key Mediator of Osteoporosis and Osteogenesis. Int J Mol Sci. 2021;22(17). Epub 20210831. doi: 10.3390/ijms22179452. PubMed PMID: 34502371; PubMed Central PMCID: PMCPMC8431678.
6. Moran MM, Wilson BM, Li J, Engen PA, Naqib A, Green SJ, et al. The gut microbiota may be a novel pathogenic mechanism in loosening of orthopedic implants in rats. Faseb j. 2020;34(11):14302-17. Epub 20200915. doi: 10.1096/fj.202001364R. PubMed PMID: 32931052; PubMed Central PMCID: PMCPMC8025663.
7. Hou K, Wu ZX, Chen XY, Wang JQ, Zhang D, Xiao C, et al. Microbiota in health and diseases. Signal Transduct Target Ther. 2022;7(1):135. Epub 20220423. doi: 10.1038/s41392-022-00974-4. PubMed PMID: 35461318; PubMed Central PMCID: PMCPMC9034083.
8. Saxami G, Kerezoudi EN, Eliopoulos C, Arapoglou D, Kyriacou A. The Gut-Organ Axis within the Human Body: Gut Dysbiosis and the Role of Prebiotics. Life (Basel). 2023;13(10). Epub 20231008. doi: 10.3390/life13102023. PubMed PMID: 37895405; PubMed Central PMCID: PMCPMC10608660.
9. Vancamelbeke M, Vermeire S. The intestinal barrier: a fundamental role in health and disease. Expert Rev Gastroenterol Hepatol. 2017;11(9):821-34. Epub 20170626. doi: 10.1080/17474124.2017.1343143. PubMed PMID: 28650209; PubMed Central PMCID: PMCPMC6104804.
10. Fu Y, Lyu J, Wang S. The role of intestinal microbes on intestinal barrier function and host immunity from a metabolite perspective. Front Immunol. 2023;14:1277102. Epub 20231009. doi: 10.3389/fimmu.2023.1277102. PubMed PMID: 37876938; PubMed Central PMCID: PMCPMC10591221.
11. Luis AS, Hansson GC. Intestinal mucus and their glycans: A habitat for thriving microbiota. Cell Host Microbe. 2023;31(7):1087-100. doi: 10.1016/j.chom.2023.05.026. PubMed PMID: 37442097; PubMed Central PMCID: PMCPMC10348403.
12. Inaba R, Vujakovic S, Bergstrom K. The gut mucus network: A dynamic liaison between microbes and the immune system. Semin Immunol. 2023;69:101807. Epub 20230719. doi: 10.1016/j.smim.2023.101807. PubMed PMID: 37478802.
13. Allaire JM, Crowley SM, Law HT, Chang SY, Ko HJ, Vallance BA. The Intestinal Epithelium: Central Coordinator of Mucosal Immunity. Trends Immunol. 2018;39(9):677-96. Epub 20180430. doi: 10.1016/j.it.2018.04.002. PubMed PMID: 29716793.
14. Brown H, Esterházy D. Intestinal immune compartmentalization: implications of tissue specific determinants in health and disease. Mucosal Immunol. 2021;14(6):1259-70. Epub 20210701. doi: 10.1038/s41385-021-00420-8. PubMed PMID: 34211125.
15. Lockhart A, Mucida D, Bilate AM. Intraepithelial Lymphocytes of the Intestine. Annu Rev Immunol. 2024;42(1):289-316. Epub 20240614. doi: 10.1146/annurev-immunol-090222-100246. PubMed PMID: 38277691; PubMed Central PMCID: PMCPMC11608099.
16. Salvo Romero E, Alonso Cotoner C, Pardo Camacho C, Casado Bedmar M, Vicario M. The intestinal barrier function and its involvement in digestive disease. Rev Esp Enferm Dig. 2015;107(11):686-96. doi: 10.17235/reed.2015.3846/2015. PubMed PMID: 26541659.
17. Li J, Jia N, Cui M, Li Y, Li X, Chu X. The intestinal mucosal barrier - A key player in rheumatoid arthritis? Clin Anat. 2023;36(7):977-85. Epub 20230516. doi: 10.1002/ca.24055. PubMed PMID: 37191299.
18. Matei DE, Menon M, Alber DG, Smith AM, Nedjat-Shokouhi B, Fasano A, et al. Intestinal barrier dysfunction plays an integral role in arthritis pathology and can be targeted to ameliorate disease. Med. 2021;2(7):864-83.e9. doi: 10.1016/j.medj.2021.04.013. PubMed PMID: 34296202; PubMed Central PMCID: PMCPMC8280953.
19. Tajik N, Frech M, Schulz O, Schälter F, Lucas S, Azizov V, et al. Targeting zonulin and intestinal epithelial barrier function to prevent onset of arthritis. Nat Commun. 2020;11(1):1995. Epub 20200424. doi: 10.1038/s41467-020-15831-7. PubMed PMID: 32332732; PubMed Central PMCID: PMCPMC7181728.
20. Lyu P, Wen J, Zhang W, Liu N, Stolzer I, Gießl A, et al. Expression of HIF1α in intestinal epithelium restricts arthritis inflammation by inhibiting RIPK3-induced cell death machinery. Ann Rheum Dis. 2024;83(8):984-97. Epub 20240715. doi: 10.1136/ard-2023-224491. PubMed PMID: 38503474; PubMed Central PMCID: PMCPMC11287550.
21. Zaiss MM, Joyce Wu HJ, Mauro D, Schett G, Ciccia F. The gut-joint axis in rheumatoid arthritis. Nat Rev Rheumatol. 2021;17(4):224-37. Epub 20210305. doi: 10.1038/s41584-021-00585-3. PubMed PMID: 33674813.

22. Romero-Figueroa MDS, Ramírez-Durán N, Montiel-Jarquín AJ, Horta-Baas G. Gut-joint axis: Gut dysbiosis can contribute to the onset of rheumatoid arthritis via multiple pathways. Front Cell Infect Microbiol. 2023;13:1092118. Epub 20230127. doi: 10.3389/fcimb.2023.1092118. PubMed PMID: 36779190; PubMed Central PMCID: PMCPMC9911673.
23. Morimoto T, Kobayashi T, Kakiuchi T, Esaki M, Tsukamoto M, Yoshihara T, et al. Gut-spine axis: a possible correlation between gut microbiota and spinal degenerative diseases. Front Microbiol. 2023;14:1290858. Epub 20231027. doi: 10.3389/fmicb.2023.1290858. PubMed PMID: 37965563; PubMed Central PMCID: PMCPMC10641865.
24. Longo UG, Lalli A, Bandini B, de Sire R, Angeletti S, Lustig S, et al. Role of the Gut Microbiota in Osteoarthritis, Rheumatoid Arthritis, and Spondylarthritis: An Update on the Gut-Joint Axis. Int J Mol Sci. 2024;25(6). Epub 20240313. doi: 10.3390/ijms25063242. PubMed PMID: 38542216; PubMed Central PMCID: PMCPMC10970477.
25. Wei Z, Li F, Pi G. Association Between Gut Microbiota and Osteoarthritis: A Review of Evidence for Potential Mechanisms and Therapeutics. Front Cell Infect Microbiol. 2022;12:812596. Epub 20220316. doi: 10.3389/fcimb.2022.812596. PubMed PMID: 35372125; PubMed Central PMCID: PMCPMC8966131.
26. Guido G, Ausenda G, Iascone V, Chisari E. Gut permeability and osteoarthritis, towards a mechanistic understanding of the pathogenesis: a systematic review. Ann Med. 2021;53(1):2380-90. doi: 10.1080/07853890.2021.2014557. PubMed PMID: 34933614; PubMed Central PMCID: PMCPMC8725942.
27. Maagensen H, Helsted MM, Gasbjerg LS, Vilsbøll T, Knop FK. The Gut-Bone Axis in Diabetes. Curr Osteoporos Rep. 2023;21(1):21-31. Epub 20221128. doi: 10.1007/s11914-022-00767-2. PubMed PMID: 36441432.
28. Wallimann A, Magrath W, Thompson K, Moriarty T, Richards RG, Akdis CA, et al. Gut microbial-derived short-chain fatty acids and bone: a potential role in fracture healing. Eur Cell Mater. 2021;41:454-70. Epub 20210421. doi: 10.22203/eCM.v041a29. PubMed PMID: 33881768; PubMed Central PMCID: PMCPMC9100835.
29. Tu Y, Yang R, Xu X, Zhou X. The microbiota-gut-bone axis and bone health. J Leukoc Biol. 2021;110(3):525-37. Epub 20210422. doi: 10.1002/jlb.3mr0321-755r. PubMed PMID: 33884666.
30. Zhang YW, Wu Y, Liu XF, Chen X, Su JC. Targeting the gut microbiota-related metabolites for osteoporosis: The inextricable connection of gut-bone axis. Ageing Res Rev. 2024;94:102196. Epub 20240112. doi: 10.1016/j.arr.2024.102196. PubMed PMID: 38218463.
31. Wallimann A, Magrath W, Pugliese B, Stocker N, Westermann P, Heider A, et al. Butyrate Inhibits Osteoclast Activity In Vitro and Regulates Systemic Inflammation and Bone Healing in a Murine Osteotomy Model Compared to Antibiotic-Treated Mice. Mediators Inflamm. 2021;2021:8817421. Epub 20211210. doi: 10.1155/2021/8817421. PubMed PMID: 34924815; PubMed Central PMCID: PMCPMC8683197.
32. Ai T, Shang L, Li B, Li J, Qin R. Konjac Oligosaccharides Alleviated Ovariectomy-Induced Bone Loss through Gut Microbiota Modulation and Treg/Th17 Regulation. J Agric Food Chem. 2024;72(14):7969-79. Epub 20240329. doi: 10.1021/acs.jafc.4c00281. PubMed PMID: 38551374.
33. Keirns BH, Lucas EA, Smith BJ. Phytochemicals affect T helper 17 and T regulatory cells and gut integrity: implications on the gut-bone axis. Nutr Res. 2020;83:30-48. Epub 20200815. doi: 10.1016/j.nutres.2020.08.006. PubMed PMID: 33010588.
34. Uematsu T, Sakai A, Ito H, Suzuki H. Intra-articular administration of tachykinin NK_1 receptor antagonists reduces hyperalgesia and cartilage destruction in the inflammatory joint in rats with adjuvant-induced arthritis. Eur J Pharmacol. 2011;668(1-2):163-8. Epub 20110706. doi: 10.1016/j.ejphar.2011.06.037. PubMed PMID: 21749865.
35. Fischer BD, Adeyemo A, O'Leary ME, Bottaro A. Animal models of rheumatoid pain: experimental systems and insights. Arthritis Res Ther. 2017;19(1):146. Epub 20170630. doi: 10.1186/s13075-017-1361-6. PubMed PMID: 28666464; PubMed Central PMCID: PMCPMC5493070.
36. Nazir S, Ahmad I, Mobashar A, Sharif A, Shabbir A, Chaudhary WA. Mechanistic evaluation of antiarthritic and anti-inflammatory effect of campesterol ester derivatives in complete Freund's adjuvant-induced arthritic rats. Front Pharmacol. 2023;14:1346054. Epub 20240123. doi: 10.3389/fphar.2023.1346054. PubMed PMID: 38322703; PubMed Central PMCID: PMCPMC10844886.
37. Wang X, Liu D, Li D, Yan J, Yang J, Zhong X, et al. Combined treatment with glucosamine and chondroitin sulfate improves rheumatoid arthritis in rats by regulating the gut microbiota. Nutr Metab (Lond).

2023;20(1):22. Epub 20230404. doi: 10.1186/s12986-023-00735-2. PubMed PMID: 37016458; PubMed Central PMCID: PMCPMC10071728.
38. Liu M, Li S, Cao N, Wang Q, Liu Y, Xu Q, et al. Intestinal flora, intestinal metabolism, and intestinal immunity changes in complete Freud's adjuvant-rheumatoid arthritis C57BL/6 mice. Int Immunopharmacol. 2023;125(Pt A):111090. Epub 20231021. doi: 10.1016/j.intimp.2023.111090. PubMed PMID: 37866312.
39. Lord MS, Melrose J, Day AJ, Whitelock JM. The Inter-α-Trypsin Inhibitor Family: Versatile Molecules in Biology and Pathology. J Histochem Cytochem. 2020;68(12):907-27. Epub 20200708. doi: 10.1369/0022155420940067. PubMed PMID: 32639183; PubMed Central PMCID: PMCPMC7711241.
40. Loredo-Pérez AA, Montalvo-Blanco CE, Hernández-González LI, Anaya-Reyes M, Fernández Del Valle-Laisequilla C, Reyes-García JG, et al. High-fat diet exacerbates pain-like behaviors and periarticular bone loss in mice with CFA-induced knee arthritis. Obesity (Silver Spring). 2016;24(5):1106-15. Epub 20160331. doi: 10.1002/oby.21485. PubMed PMID: 27030572.
41. Schulkin J, Sterling P. Allostasis: A Brain-Centered, Predictive Mode of Physiological Regulation. Trends Neurosci. 2019;42(10):740-52. Epub 20190902. doi: 10.1016/j.tins.2019.07.010. PubMed PMID: 31488322.
42. Wu G, Nie W, Wang Q, Hao Y, Gong S, Zheng Y, et al. Umbelliferone Ameliorates Complete Freund Adjuvant-Induced Arthritis via Reduction of NF-κB Signaling Pathway in Osteoclast Differentiation. Inflammation. 2021;44(4):1315-29. Epub 20210123. doi: 10.1007/s10753-021-01418-x. PubMed PMID: 33484396.
43. Thind AS, Monga I, Thakur PK, Kumari P, Dindhoria K, Krzak M, et al. Demystifying emerging bulk RNA-Seq applications: the application and utility of bioinformatic methodology. Brief Bioinform. 2021;22(6). doi: 10.1093/bib/bbab259. PubMed PMID: 34329375.
44. Parisien M, Lima LV, Dagostino C, El-Hachem N, Drury GL, Grant AV, et al. Acute inflammatory response via neutrophil activation protects against the development of chronic pain. Sci Transl Med. 2022;14(644):eabj9954. Epub 20220511. doi: 10.1126/scitranslmed.abj9954. PubMed PMID: 35544595; PubMed Central PMCID: PMCPMC10317000.
45. Sung PS, Chang WC, Hsieh SL. CLEC5A: A Promiscuous Pattern Recognition Receptor to Microbes and Beyond. Adv Exp Med Biol. 2020;1204:57-73. doi: 10.1007/978-981-15-1580-4_3. PubMed PMID: 32152943; PubMed Central PMCID: PMCPMC7121389.
46. Zhou M, Qin S, Chu Y, Wang F, Chen L, Lu Y. Immunolocalization of MMP-2 and MMP-9 in human rheumatoid synovium. Int J Clin Exp Pathol. 2014;7(6):3048-56. Epub 20140515. PubMed PMID: 25031723; PubMed Central PMCID: PMCPMC4097284.
47. Gartshteyn Y, Askanase AD, Mor A. SLAM Associated Protein Signaling in T Cells: Tilting the Balance Toward Autoimmunity. Front Immunol. 2021;12:654839. Epub 20210416. doi: 10.3389/fimmu.2021.654839. PubMed PMID: 33936082; PubMed Central PMCID: PMCPMC8086963.
48. Cesaro A, Anceriz N, Plante A, Pagé N, Tardif MR, Tessier PA. An inflammation loop orchestrated by S100A9 and calprotectin is critical for development of arthritis. PLoS One. 2012;7(9):e45478. Epub 20120918. doi: 10.1371/journal.pone.0045478. PubMed PMID: 23029038; PubMed Central PMCID: PMCPMC3445527.
49. Takata K, Takano S, Miyagi M, Mukai M, Iwase D, Aikawa J, et al. Elevated macrophage-inducible C-type lectin expression in the synovial tissue of patients with rheumatoid arthritis. Cent Eur J Immunol. 2021;46(4):470-3. Epub 20211203. doi: 10.5114/ceji.2021.111471. PubMed PMID: 35125945; PubMed Central PMCID: PMCPMC8808308.
50. Gulkesen A, Akgol G, Poyraz AK, Aydin S, Denk A, Yildirim T, et al. Lipocalin 2 as a clinical significance in rheumatoid arthritis. Cent Eur J Immunol. 2017;42(3):269-73. Epub 20171030. doi: 10.5114/ceji.2017.70969. PubMed PMID: 29204091; PubMed Central PMCID: PMCPMC5708208.
51. Kasher M, Williams FMK, Freidin MB, Malkin I, Cherny SS, Livshits G. Understanding the complex genetic architecture connecting rheumatoid arthritis, osteoporosis and inflammation: discovering causal pathways. Hum Mol Genet. 2022;31(16):2810-9. doi: 10.1093/hmg/ddac061. PubMed PMID: 35349660; PubMed Central PMCID: PMCPMC9402243.
52. Esalatmanesh K, Fayyazi H, Esalatmanesh R, Khabbazi A. The association between serum levels of growth differentiation factor-15 and rheumatoid arthritis activity. Int J Clin Pract. 2020;74(9):e13564. Epub 20200618. doi: 10.1111/ijcp.13564. PubMed PMID: 32478946.
53. van Caam A, Aarts J, van Ee T, Vitters E, Koenders M, van de Loo F, et al. TGFβ-mediated expression of TGFβ-activating integrins in SSc monocytes: disturbed activation of latent TGFβ? Arthritis Res Ther.

2020;22(1):42. Epub 20200306. doi: 10.1186/s13075-020-2130-5. PubMed PMID: 32143707; PubMed Central PMCID: PMCPMC7059334.
54. Martín-Márquez BT, Sandoval-García F, Corona-Meraz FI, Martínez-García EA, Sánchez-Hernández PE, Salazar-Páramo M, et al. Osteopontin: A Bone-Derived Protein Involved in Rheumatoid Arthritis and Osteoarthritis Immunopathology. Biomolecules. 2023;13(3). Epub 20230309. doi: 10.3390/biom13030502. PubMed PMID: 36979437; PubMed Central PMCID: PMCPMC10046882.
55. Li Y, Zhang S, Liu J, Zhang Y, Zhang N, Cheng Q, et al. The pentraxin family in autoimmune disease. Clin Chim Acta. 2023;551:117592. Epub 20231011. doi: 10.1016/j.cca.2023.117592. PubMed PMID: 37832905.
56. Van Der Meer-Van Kraaij C, Van Lieshout EM, Kramer E, Van Der Meer R, Keijer J. Mucosal pentraxin (Mptx), a novel rat gene 10-fold down-regulated in colon by dietary heme. Faseb j. 2003;17(10):1277-85. doi: 10.1096/fj.02-1036com. PubMed PMID: 12832292.
57. Sun C, Wang X, Hui Y, Fukui H, Wang B, Miwa H. The Potential Role of REG Family Proteins in Inflammatory and Inflammation-Associated Diseases of the Gastrointestinal Tract. Int J Mol Sci. 2021;22(13). Epub 20210703. doi: 10.3390/ijms22137196. PubMed PMID: 34281249; PubMed Central PMCID: PMCPMC8268738.
58. Greenhill C. REG3G - a potential link between the intestinal microbiome and host physiology. Nat Rev Endocrinol. 2023;19(1):5. doi: 10.1038/s41574-022-00774-4. PubMed PMID: 36319759.
59. Grunddal KV, Tonack S, Egerod KL, Thompson JJ, Petersen N, Engelstoft MS, et al. Adhesion receptor ADGRG2/GPR64 is in the GI-tract selectively expressed in mature intestinal tuft cells. Mol Metab. 2021;51:101231. Epub 20210405. doi: 10.1016/j.molmet.2021.101231. PubMed PMID: 33831593; PubMed Central PMCID: PMCPMC8105302.
60. Stacey D, Suppiah V, Benyamin B, Lee SH, Hyppönen E. In-silico functional analyses identify TMPRSS15-mediated intestinal absorption of lithium as a modulator of lithium response in bipolar disorder. J Affect Disord. 2024;358:416-21. Epub 20240510. doi: 10.1016/j.jad.2024.05.050. PubMed PMID: 38735581.
61. Dos Santos Ramos A, Viana GCS, de Macedo Brigido M, Almeida JF. Neutrophil extracellular traps in inflammatory bowel diseases: Implications in pathogenesis and therapeutic targets. Pharmacol Res. 2021;171:105779. Epub 20210721. doi: 10.1016/j.phrs.2021.105779. PubMed PMID: 34298111.
62. Li T, Wen Y, Lu Q, Hua S, Hou Y, Du X, et al. MST1/2 in inflammation and immunity. Cell Adh Migr. 2023;17(1):1-15. Epub 20231101. doi: 10.1080/19336918.2023.2276616. PubMed PMID: 37909712; PubMed Central PMCID: PMCPMC10761064.
63. Duluc I, Lorentz O, Fritsch C, Leberquier C, Kedinger M, Freund JN. Changing intestinal connective tissue interactions alters homeobox gene expression in epithelial cells. J Cell Sci. 1997;110 (Pt 11):1317-24. doi: 10.1242/jcs.110.11.1317. PubMed PMID: 9202392.
64. Fotiadis D, Kanai Y, Palacín M. The SLC3 and SLC7 families of amino acid transporters. Mol Aspects Med. 2013;34(2-3):139-58. doi: 10.1016/j.mam.2012.10.007. PubMed PMID: 23506863.
65. Li M, Zhao J, Cao M, Liu R, Chen G, Li S, et al. Mast cells-derived MiR-223 destroys intestinal barrier function by inhibition of CLDN8 expression in intestinal epithelial cells. Biol Res. 2020;53(1):12. Epub 20200324. doi: 10.1186/s40659-020-00279-2. PubMed PMID: 32209121; PubMed Central PMCID: PMCPMC7092522.
66. Zhang C, Xiang C, Zhou K, Liu X, Qiao G, Zhao Y, et al. Intestinal lysozyme1 deficiency alters microbiota composition and impacts host metabolism through the emergence of NAD(+)-secreting ASTB Qing110 bacteria. mSystems. 2024;9(3):e0121423. Epub 20240216. doi: 10.1128/msystems.01214-23. PubMed PMID: 38364095; PubMed Central PMCID: PMCPMC10949482.
67. Grizotte-Lake M, Zhong G, Duncan K, Kirkwood J, Iyer N, Smolenski I, et al. Commensals Suppress Intestinal Epithelial Cell Retinoic Acid Synthesis to Regulate Interleukin-22 Activity and Prevent Microbial Dysbiosis. Immunity. 2018;49(6):1103-15.e6. doi: 10.1016/j.immuni.2018.11.018. PubMed PMID: 30566883; PubMed Central PMCID: PMCPMC6319961.
68. Yan S, Conley JM, Reilly AM, Stull ND, Abhyankar SD, Ericsson AC, et al. Intestinal Gpr17 deficiency improves glucose metabolism by promoting GLP-1 secretion. Cell Rep. 2022;38(1):110179. doi: 10.1016/j.celrep.2021.110179. PubMed PMID: 34986353; PubMed Central PMCID: PMCPMC8972502.
69. Morrice N, Vainio S, Mikkola K, van Aalten L, Gallagher JR, Ashford MLJ, et al. Metformin increases the uptake of glucose into the gut from the circulation in high-fat diet-fed male mice, which is enhanced by a

reduction in whole-body Slc2a2 expression. Mol Metab. 2023;77:101807. Epub 20230916. doi: 10.1016/j.molmet.2023.101807. PubMed PMID: 37717665; PubMed Central PMCID: PMCPMC10550722.
70. Soták M, Casselbrant A, Rath E, Zietek T, Strömstedt M, Adingupu DD, et al. Intestinal sodium/glucose cotransporter 3 expression is epithelial and downregulated in obesity. Life Sci. 2021;267:118974. Epub 20201230. doi: 10.1016/j.lfs.2020.118974. PubMed PMID: 33385407.
71. Zhai Y, Liu X, Huang Z, Zhang J, Stalin A, Tan Y, et al. Data mining combines bioinformatics discover immunoinfiltration-related gene SERPINE1 as a biomarker for diagnosis and prognosis of stomach adenocarcinoma. Sci Rep. 2023;13(1):1373. Epub 20230125. doi: 10.1038/s41598-023-28234-7. PubMed PMID: 36697459; PubMed Central PMCID: PMCPMC9876925.
72. Glal D, Sudhakar JN, Lu HH, Liu MC, Chiang HY, Liu YC, et al. ATF3 Sustains IL-22-Induced STAT3 Phosphorylation to Maintain Mucosal Immunity Through Inhibiting Phosphatases. Front Immunol. 2018;9:2522. Epub 20181105. doi: 10.3389/fimmu.2018.02522. PubMed PMID: 30455690; PubMed Central PMCID: PMCPMC6230592.
73. Cao Y, Yang Q, Deng H, Tang J, Hu J, Liu H, et al. Transcriptional factor ATF3 protects against colitis by regulating follicular helper T cells in Peyer's patches. Proc Natl Acad Sci U S A. 2019;116(13):6286-91. Epub 20190312. doi: 10.1073/pnas.1818164116. PubMed PMID: 30862736; PubMed Central PMCID: PMCPMC6442638.
74. Mayassi T, Ladell K, Gudjonson H, McLaren JE, Shaw DG, Tran MT, et al. Chronic Inflammation Permanently Reshapes Tissue-Resident Immunity in Celiac Disease. Cell. 2019;176(5):967-81.e19. Epub 20190207. doi: 10.1016/j.cell.2018.12.039. PubMed PMID: 30739797; PubMed Central PMCID: PMCPMC6667191.
75. Rodriguez Sawicki L, Bottasso Arias NM, Scaglia N, Falomir Lockhart LJ, Franchini GR, Storch J, et al. FABP1 knockdown in human enterocytes impairs proliferation and alters lipid metabolism. Biochim Biophys Acta Mol Cell Biol Lipids. 2017;1862(12):1587-94. Epub 20170913. doi: 10.1016/j.bbalip.2017.09.006. PubMed PMID: 28919479; PubMed Central PMCID: PMCPMC5663247.
76. Wang R, Kwon IK, Singh N, Islam B, Liu K, Sridhar S, et al. Type 2 cGMP-dependent protein kinase regulates homeostasis by blocking c-Jun N-terminal kinase in the colon epithelium. Cell Death Differ. 2014;21(3):427-37. Epub 20131122. doi: 10.1038/cdd.2013.163. PubMed PMID: 24270408; PubMed Central PMCID: PMCPMC3921591.
77. Tetteh PW, Kretzschmar K, Begthel H, van den Born M, Korving J, Morsink F, et al. Generation of an inducible colon-specific Cre enzyme mouse line for colon cancer research. Proc Natl Acad Sci U S A. 2016;113(42):11859-64. Epub 20161005. doi: 10.1073/pnas.1614057113. PubMed PMID: 27708166; PubMed Central PMCID: PMCPMC5081651.
78. Fukui H, Sekikawa A, Tanaka H, Fujimori Y, Katake Y, Fujii S, et al. DMBT1 is a novel gene induced by IL-22 in ulcerative colitis. Inflamm Bowel Dis. 2011;17(5):1177-88. Epub 20100907. doi: 10.1002/ibd.21473. PubMed PMID: 20824812.
79. Liu Z, Chen X, Wang X, Chen X, Song CH, Du Y, et al. Chemokine CXCL11 links microbial stimuli to intestinal inflammation. Clin Exp Immunol. 2011;164(3):396-406. Epub 20110325. doi: 10.1111/j.1365-2249.2011.04382.x. PubMed PMID: 21438871; PubMed Central PMCID: PMCPMC3087936.
80. Pulakazhi Venu VK, Alston L, Iftinca M, Tsai YC, Stephens M, Warriyar KVV, et al. Nr4A1 modulates inflammation-associated intestinal fibrosis and dampens fibrogenic signaling in myofibroblasts. Am J Physiol Gastrointest Liver Physiol. 2021;321(3):G280-g97. Epub 20210721. doi: 10.1152/ajpgi.00338.2019. PubMed PMID: 34288735.
81. Kriz V, Korinek V. Wnt, RSPO and Hippo Signalling in the Intestine and Intestinal Stem Cells. Genes (Basel). 2018;9(1). Epub 20180108. doi: 10.3390/genes9010020. PubMed PMID: 29316729; PubMed Central PMCID: PMCPMC5793173.
82. Sun EW, Martin AM, de Fontgalland D, Sposato L, Rabbitt P, Hollington P, et al. Evidence for Glucagon Secretion and Function Within the Human Gut. Endocrinology. 2021;162(4). doi: 10.1210/endocr/bqab022. PubMed PMID: 33534908.
83. Hughes CJ, Alderman C, Wolin AR, Fields KM, Zhao R, Ford HL. All eyes on Eya: A unique transcriptional co-activator and phosphatase in cancer. Biochim Biophys Acta Rev Cancer. 2024;1879(3):189098. Epub 20240328. doi: 10.1016/j.bbcan.2024.189098. PubMed PMID: 38555001; PubMed Central PMCID: PMCPMC11111358.

84. Kim M, Jho EH. Cross-talk between Wnt/β-catenin and Hippo signaling pathways: a brief review. BMB Rep. 2014;47(10):540-5. doi: 10.5483/bmbrep.2014.47.10.177. PubMed PMID: 25154721; PubMed Central PMCID: PMCPMC4261510.
85. Li M, Zhang FJ, Bai RJ. The Hippo-YAP Signaling Pathway in Osteoarthritis and Rheumatoid Arthritis. J Inflamm Res. 2024;17:1105-20. Epub 20240219. doi: 10.2147/jir.S444758. PubMed PMID: 38406325; PubMed Central PMCID: PMCPMC10891274.
86. Li XF, Yin SQ, Li H, Yang YL, Chen X, Song B, et al. PPAR-γ alleviates the inflammatory response in TNF-α-induced fibroblast-like synoviocytes by binding to p53 in rheumatoid arthritis. Acta Pharmacol Sin. 2023;44(2):454-64. Epub 20220802. doi: 10.1038/s41401-022-00957-9. PubMed PMID: 35918412; PubMed Central PMCID: PMCPMC9889328.
87. Jüni P, Hari R, Rutjes AW, Fischer R, Silletta MG, Reichenbach S, et al. Intra-articular corticosteroid for knee osteoarthritis. Cochrane Database Syst Rev. 2015;2015(10):Cd005328. Epub 20151022. doi: 10.1002/14651858.CD005328.pub3. PubMed PMID: 26490760; PubMed Central PMCID: PMCPMC8884338.
88. Reichenbach S, Rutjes AW, Nüesch E, Trelle S, Jüni P. Joint lavage for osteoarthritis of the knee. Cochrane Database Syst Rev. 2010;(5):Cd007320. Epub 20100512. doi: 10.1002/14651858.CD007320.pub2. PubMed PMID: 20464751.
89. Genua M, Rutella S, Correale C, Danese S. The triggering receptor expressed on myeloid cells (TREM) in inflammatory bowel disease pathogenesis. J Transl Med. 2014;12:293. Epub 20141028. doi: 10.1186/s12967-014-0293-z. PubMed PMID: 25347935; PubMed Central PMCID: PMCPMC4231187.
90. Bishop ES, Namkoong H, Aurelian L, McCarthy M, Nallagatla P, Zhou W, et al. Age-dependent Microglial Disease Phenotype Results in Functional Decline in Gut Macrophages. Gastro Hep Adv. 2023;2(2):261-76. Epub 20220929. doi: 10.1016/j.gastha.2022.09.006. PubMed PMID: 36908772; PubMed Central PMCID: PMCPMC10003669.
91. Johansson ME, Hansson GC. Immunological aspects of intestinal mucus and mucins. Nat Rev Immunol. 2016;16(10):639-49. Epub 20160808. doi: 10.1038/nri.2016.88. PubMed PMID: 27498766; PubMed Central PMCID: PMCPMC6435297.
92. Chen YF, Boland CR, Kraus ER, Goldstein IJ. The lectin Griffonia simplicifolia I-A4 (GS I-A4) specifically recognizes terminal alpha-linked N-acetylgalactosaminyl groups and is cytotoxic to the human colon cancer cell lines LS174t and SW1116. Int J Cancer. 1994;57(4):561-7. doi: 10.1002/ijc.2910570420. PubMed PMID: 7514154.
93. Yao Y, Kim G, Shafer S, Chen Z, Kubo S, Ji Y, et al. Mucus sialylation determines intestinal host-commensal homeostasis. Cell. 2022;185(7):1172-88.e28. Epub 20220317. doi: 10.1016/j.cell.2022.02.013. PubMed PMID: 35303419; PubMed Central PMCID: PMCPMC9088855.
94. Forouzanfar F, Pourbagher-Shahri AM, Ghazavi H. Evaluation of Antiarthritic and Antinociceptive Effects of Cedrol in a Rat Model of Arthritis. Oxid Med Cell Longev. 2022;2022:4943965. Epub 20220425. doi: 10.1155/2022/4943965. PubMed PMID: 35509836; PubMed Central PMCID: PMCPMC9060983.
95. Hasan H, Ismail H, El-Orfali Y, Khawaja G. Therapeutic benefits of Indole-3-Carbinol in adjuvant-induced arthritis and its protective effect against methotrexate induced-hepatic toxicity. BMC Complement Altern Med. 2018;18(1):337. Epub 20181219. doi: 10.1186/s12906-018-2408-1. PubMed PMID: 30567538; PubMed Central PMCID: PMCPMC6299996.
96. Chen X, Wang J, He Z, Liu X, Liu H, Wang X. Analgesic and Anxiolytic Effects of Gastrodin and Its Influences on Ferroptosis and Jejunal Microbiota in Complete Freund's Adjuvant-Injected Mice. Front Microbiol. 2022;13:841662. Epub 20220419. doi: 10.3389/fmicb.2022.841662. PubMed PMID: 35516438; PubMed Central PMCID: PMCPMC9063750.
97. Burek DJ, Massaly N, Yoon HJ, Doering M, Morón JA. Behavioral outcomes of complete Freund adjuvant-induced inflammatory pain in the rodent hind paw: a systematic review and meta-analysis. Pain. 2022;163(5):809-19. doi: 10.1097/j.pain.0000000000002467. PubMed PMID: 34510137; PubMed Central PMCID: PMCPMC9018465.
98. Irfan HM, Anjum A, Asim MH, Rasheed SU, Alamgeer, Siddique F. In vitro and in vivo modulatory effects of fluoxetine on gene expression and antioxidant enzymes in CFA-induced chronic inflammatory model: drug repurposing for arthritis. Inflammopharmacology. 2024;32(5):3429-41. Epub 20240827. doi: 10.1007/s10787-024-01553-5. PubMed PMID: 39192161.

99. Kaneguchi A, Ozawa J, Moriyama H, Yamaoka K. Nociception contributes to the formation of myogenic contracture in the early phase of adjuvant-induced arthritis in a rat knee. J Orthop Res. 2017;35(7):1404-13. Epub 20160919. doi: 10.1002/jor.23412. PubMed PMID: 27584936.
100. Golabi S, Zaringhalam J, Manaheji H. The Impact of Synovial NF-κB Activation on Apoptosis Pattern Change During Adjuvant-induced Inflammation. Basic Clin Neurosci. 2017;8(3):173-82. doi: 10.18869/nirp.bcn.8.3.173. PubMed PMID: 28781725; PubMed Central PMCID: PMCPMC5535323.
101. Golabi S, Zaringhalam J, Manaheji H. Synovial interlukin-6 affects apoptosis induction via nuclear factor kappa-B and fractalkine pathway during adjuvant arthritis. Med J Islam Repub Iran. 2020;34:25. Epub 20200325. doi: 10.34171/mjiri.34.25. PubMed PMID: 32551314; PubMed Central PMCID: PMCPMC7293817.
102. Cai L, Li CM, Tang WJ, Liu MM, Chen WN, Qiu YY, et al. Therapeutic Effect of Penta-acetyl Geniposide on Adjuvant-Induced Arthritis in Rats: Involvement of Inducing Synovial Apoptosis and Inhibiting NF-κB Signal Pathway. Inflammation. 2018;41(6):2184-95. doi: 10.1007/s10753-018-0861-0. PubMed PMID: 30069664.
103. Sun HQ, Yan D, Wang QN, Meng HZ, Zhang YY, Yin LX, et al. 1,25-Dihydroxyvitamin D3 attenuates disease severity and induces synoviocyte apoptosis in a concentration-dependent manner in rats with adjuvant-induced arthritis by inactivating the NF-κB signaling pathway. J Bone Miner Metab. 2019;37(3):430-40. Epub 20180810. doi: 10.1007/s00774-018-0944-x. PubMed PMID: 30097709.
104. Yoshihara Y, Plaas A, Osborn B, Margulis A, Nelson F, Stewart M, et al. Superficial zone chondrocytes in normal and osteoarthritic human articular cartilages synthesize novel truncated forms of inter-alpha-trypsin inhibitor heavy chains which are attached to a chondroitin sulfate proteoglycan other than bikunin. Osteoarthritis Cartilage. 2008;16(11):1343-55. Epub 20080603. doi: 10.1016/j.joca.2008.04.004. PubMed PMID: 18524635.
105. Falkenberg C, Blom A, Fries E, Ekström G, Särnstrand B, Salier JP, et al. Alpha1-microglobulin and bikunin in rats with collagen II-induced arthritis: plasma levels and liver mRNA content. Scand J Immunol. 1997;46(2):122-8. doi: 10.1046/j.1365-3083.1997.d01-103.x. PubMed PMID: 9583992.
106. Kida D, Yoneda M, Miyaura S, Ishimaru T, Yoshida Y, Ito T, et al. The SHAP-HA complex in sera from patients with rheumatoid arthritis and osteoarthritis. J Rheumatol. 1999;26(6):1230-8. PubMed PMID: 10381035.
107. Scott JL, Dong Y, Yin J, Dodd RJ, Kouvatsos N, Drummond SP, et al. A novel method to quantify TSG-6 protein levels in synovial fluid from osteoarthritis patients. Proteoglycan Research. 2024;2(3):e70003. doi: https://doi.org/10.1002/pgr2.70003.
108. Day AJ, Milner CM. TSG-6: A multifunctional protein with anti-inflammatory and tissue-protective properties. Matrix Biol. 2019;78-79:60-83. Epub 20180131. doi: 10.1016/j.matbio.2018.01.011. PubMed PMID: 29362135.
109. Day AJ. Hyaluronan-protein interactions: Lilliput revisited. Proteoglycan Research. 2024;2(4):e70007. doi: https://doi.org/10.1002/pgr2.70007.
110. Erxleben DA, Dodd RJ, Day AJ, Green DE, DeAngelis PL, Poddar S, et al. Targeted Analysis of the Size Distribution of Heavy Chain-Modified Hyaluronan with Solid-State Nanopores. Anal Chem. 2024;96(4):1606-13. Epub 20240112. doi: 10.1021/acs.analchem.3c04387. PubMed PMID: 38215004; PubMed Central PMCID: PMCPMC11037269.
111. Yingsung W, Zhuo L, Morgelin M, Yoneda M, Kida D, Watanabe H, et al. Molecular heterogeneity of the SHAP-hyaluronan complex. Isolation and characterization of the complex in synovial fluid from patients with rheumatoid arthritis. J Biol Chem. 2003;278(35):32710-8. Epub 20030610. doi: 10.1074/jbc.M303658200. PubMed PMID: 12799384.
112. Zhuo L, Kanamori A, Kannagi R, Itano N, Wu J, Hamaguchi M, et al. SHAP potentiates the CD44-mediated leukocyte adhesion to the hyaluronan substratum. J Biol Chem. 2006;281(29):20303-14. Epub 20060515. doi: 10.1074/jbc.M506703200. PubMed PMID: 16702221.
113. de la Motte CA, Hascall VC, Drazba J, Bandyopadhyay SK, Strong SA. Mononuclear leukocytes bind to specific hyaluronan structures on colon mucosal smooth muscle cells treated with polyinosinic acid:polycytidylic acid: inter-alpha-trypsin inhibitor is crucial to structure and function. Am J Pathol. 2003;163(1):121-33. doi: 10.1016/s0002-9440(10)63636-x. PubMed PMID: 12819017; PubMed Central PMCID: PMCPMC1868154.
114. Shanaj S, Donlin LT. Synovial Tissue: Cellular and Molecular Phenotyping. Curr Rheumatol Rep. 2019;21(10):52. Epub 20190829. doi: 10.1007/s11926-019-0858-1. PubMed PMID: 31468238.

115. Zhang F, Jonsson AH, Nathan A, Millard N, Curtis M, Xiao Q, et al. Deconstruction of rheumatoid arthritis synovium defines inflammatory subtypes. Nature. 2023;623(7987):616-24. Epub 20231108. doi: 10.1038/s41586-023-06708-y. PubMed PMID: 37938773; PubMed Central PMCID: PMCPMC10651487.
116. Zheng Y, Wei K, Jiang P, Zhao J, Shan Y, Shi Y, et al. Macrophage polarization in rheumatoid arthritis: signaling pathways, metabolic reprogramming, and crosstalk with synovial fibroblasts. Front Immunol. 2024;15:1394108. Epub 20240510. doi: 10.3389/fimmu.2024.1394108. PubMed PMID: 38799455; PubMed Central PMCID: PMCPMC11116671.
117. Kieler M, Hofmann M, Schabbauer G. More than just protein building blocks: how amino acids and related metabolic pathways fuel macrophage polarization. Febs j. 2021;288(12):3694-714. Epub 20210222. doi: 10.1111/febs.15715. PubMed PMID: 33460504; PubMed Central PMCID: PMCPMC8359336.
118. Barasa L, Thompson PR. Protein citrullination: inhibition, identification and insertion. Philos Trans R Soc Lond B Biol Sci. 2023;378(1890):20220240. Epub 20231002. doi: 10.1098/rstb.2022.0240. PubMed PMID: 37778377; PubMed Central PMCID: PMCPMC10542963.
119. Cao X, Cui Z, Ding Z, Chen Y, Wu S, Wang X, et al. An osteoarthritis subtype characterized by synovial lipid metabolism disorder and fibroblast-like synoviocyte dysfunction. J Orthop Translat. 2022;33:142-52. Epub 20220312. doi: 10.1016/j.jot.2022.02.007. PubMed PMID: 35330945; PubMed Central PMCID: PMCPMC8919236.
120. Shen C, Gu B, Tang M, Ma K, Du K, Wu J, et al. Biomarkers Identification of Early Rheumatoid Arthritis via Bioinformatics Approach and Experimental Verification. Ann Clin Lab Sci. 2024;54(5):661-70. PubMed PMID: 39537231.
121. Hardy RS, Raza K, Cooper MS. Glucocorticoid metabolism in rheumatoid arthritis. Ann N Y Acad Sci. 2014;1318:18-26. Epub 20140301. doi: 10.1111/nyas.12389. PubMed PMID: 24579884.
122. Weivoda MM, Bradley EW. Macrophages and Bone Remodeling. J Bone Miner Res. 2023;38(3):359-69. Epub 20230203. doi: 10.1002/jbmr.4773. PubMed PMID: 36651575; PubMed Central PMCID: PMCPMC10023335.
123. Yin Z, Gong G, Liu X, Yin J. Mechanism of regulating macrophages/osteoclasts in attenuating wear particle-induced aseptic osteolysis. Front Immunol. 2023;14:1274679. Epub 20231004. doi: 10.3389/fimmu.2023.1274679. PubMed PMID: 37860014; PubMed Central PMCID: PMCPMC10582964.
124. Wu YL, Zhang CH, Teng Y, Pan Y, Liu NC, Liu PX, et al. Propionate and butyrate attenuate macrophage pyroptosis and osteoclastogenesis induced by CoCrMo alloy particles. Mil Med Res. 2022;9(1):46. Epub 20220823. doi: 10.1186/s40779-022-00404-0. PubMed PMID: 35996168; PubMed Central PMCID: PMCPMC9396885.
125. Kikyo N. Circadian Regulation of Macrophages and Osteoclasts in Rheumatoid Arthritis. Int J Mol Sci. 2023;24(15). Epub 20230801. doi: 10.3390/ijms241512307. PubMed PMID: 37569682; PubMed Central PMCID: PMCPMC10418470.
126. Viola A, Munari F, Sánchez-Rodríguez R, Scolaro T, Castegna A. The Metabolic Signature of Macrophage Responses. Front Immunol. 2019;10:1462. Epub 20190703. doi: 10.3389/fimmu.2019.01462. PubMed PMID: 31333642; PubMed Central PMCID: PMCPMC6618143.
127. Albtoush N, Queisser KA, Zawerton A, Lauer ME, Beswick EJ, Petrey AC. TSG6 hyaluronan matrix remodeling dampens the inflammatory response during colitis. Matrix Biol. 2023;121:149-66. Epub 20230629. doi: 10.1016/j.matbio.2023.06.007. PubMed PMID: 37391162; PubMed Central PMCID: PMCPMC10530565.
128. He H, Zhang S, Tighe S, Son J, Tseng SCG. Immobilized heavy chain-hyaluronic acid polarizes lipopolysaccharide-activated macrophages toward M2 phenotype. J Biol Chem. 2013;288(36):25792-803. Epub 20130722. doi: 10.1074/jbc.M113.479584. PubMed PMID: 23878196; PubMed Central PMCID: PMCPMC3764786.
129. Vidal B, Cascão R, Finnilä MAJ, Lopes IP, da Glória VG, Saarakkala S, et al. Effects of tofacitinib in early arthritis-induced bone loss in an adjuvant-induced arthritis rat model. Rheumatology (Oxford). 2018;57(8):1461-71. doi: 10.1093/rheumatology/kex258. PubMed PMID: 28968875.
130. Ross RD, Sumner DR. Bone Matrix Maturation in a Rat Model of Intra-Cortical Bone Remodeling. Calcif Tissue Int. 2017;101(2):193-203. Epub 20170403. doi: 10.1007/s00223-017-0270-7. PubMed PMID: 28374176; PubMed Central PMCID: PMCPMC5500434.
131. Zhang Y, Luo Y, Shi J, Xie Y, Shao H, Li Y. All-trans retinoic acid alleviates collagen-induced arthritis and promotes intestinal homeostasis. Scientific Reports. 2024;14(1):1811. doi: 10.1038/s41598-024-52322-x.

132. Pérez S, Taléns-Visconti R, Rius-Pérez S, Finamor I, Sastre J. Redox signaling in the gastrointestinal tract. Free Radic Biol Med. 2017;104:75-103. Epub 20170103. doi: 10.1016/j.freeradbiomed.2016.12.048. PubMed PMID: 28062361.
133. Bhattacharyya A, Chattopadhyay R, Mitra S, Crowe SE. Oxidative stress: an essential factor in the pathogenesis of gastrointestinal mucosal diseases. Physiol Rev. 2014;94(2):329-54. doi: 10.1152/physrev.00040.2012. PubMed PMID: 24692350; PubMed Central PMCID: PMCPMC4044300.
134. Wen X, Tang L, Zhong R, Liu L, Chen L, Zhang H. Role of Mitophagy in Regulating Intestinal Oxidative Damage. Antioxidants (Basel). 2023;12(2). Epub 20230214. doi: 10.3390/antiox12020480. PubMed PMID: 36830038; PubMed Central PMCID: PMCPMC9952109.
135. Wang C, Lv T, Jin B, Li Y, Fan Z. Regulatory role of PPAR in colorectal cancer. Cell Death Discov. 2025;11(1):28. Epub 20250128. doi: 10.1038/s41420-025-02313-2. PubMed PMID: 39875357; PubMed Central PMCID: PMCPMC11775197.
136. Vallée A, Lecarpentier Y. Crosstalk Between Peroxisome Proliferator-Activated Receptor Gamma and the Canonical WNT/β-Catenin Pathway in Chronic Inflammation and Oxidative Stress During Carcinogenesis. Front Immunol. 2018;9:745. Epub 20180413. doi: 10.3389/fimmu.2018.00745. PubMed PMID: 29706964; PubMed Central PMCID: PMCPMC5908886.
137. Maniati E, Bossard M, Cook N, Candido JB, Emami-Shahri N, Nedospasov SA, et al. Crosstalk between the canonical NF-κB and Notch signaling pathways inhibits Pparγ expression and promotes pancreatic cancer progression in mice. J Clin Invest. 2011;121(12):4685-99. Epub 20111107. doi: 10.1172/jci45797. PubMed PMID: 22056382; PubMed Central PMCID: PMCPMC3225987.
138. Shipley JM, Waxman DJ. Simultaneous, bidirectional inhibitory crosstalk between PPAR and STAT5b. Toxicol Appl Pharmacol. 2004;199(3):275-84. doi: 10.1016/j.taap.2003.12.020. PubMed PMID: 15364543.
139. Kumar N, Sharma N, Mehan S. Connection between JAK/STAT and PPARγ Signaling During the Progression of Multiple Sclerosis: Insights into the Modulation of T-Cells and Immune Responses in the Brain. Curr Mol Pharmacol. 2021;14(5):823-37. doi: 10.2174/1874467214666210301121432. PubMed PMID: 33645493.
140. Wang L, Zhang X, Farrar WL, Yang X. Transcriptional crosstalk between nuclear receptors and cytokine signal transduction pathways in immunity. Cell Mol Immunol. 2004;1(6):416-24. PubMed PMID: 16293210.
141. Grandi FC, Modi H, Kampman L, Corces MR. Chromatin accessibility profiling by ATAC-seq. Nat Protoc. 2022;17(6):1518-52. Epub 20220427. doi: 10.1038/s41596-022-00692-9. PubMed PMID: 35478247; PubMed Central PMCID: PMCPMC9189070.
142. Agirman G, Yu KB, Hsiao EY. Signaling inflammation across the gut-brain axis. Science. 2021;374(6571):1087-92. Epub 20211125. doi: 10.1126/science.abi6087. PubMed PMID: 34822299.
143. Holland AM, Bon-Frauches AC, Keszthelyi D, Melotte V, Boesmans W. The enteric nervous system in gastrointestinal disease etiology. Cell Mol Life Sci. 2021;78(10):4713-33. Epub 20210326. doi: 10.1007/s00018-021-03812-y. PubMed PMID: 33770200; PubMed Central PMCID: PMCPMC8195951.
144. Chalazonitis A, Rao M. Enteric nervous system manifestations of neurodegenerative disease. Brain Res. 2018;1693(Pt B):207-13. Epub 20180131. doi: 10.1016/j.brainres.2018.01.011. PubMed PMID: 29360466; PubMed Central PMCID: PMCPMC6003851.
145. Schneider KM, Blank N, Alvarez Y, Thum K, Lundgren P, Litichevskiy L, et al. The enteric nervous system relays psychological stress to intestinal inflammation. Cell. 2023;186(13):2823-38.e20. Epub 20230525. doi: 10.1016/j.cell.2023.05.001. PubMed PMID: 37236193; PubMed Central PMCID: PMCPMC10330875.
146. McEwen BS. Neurobiological and Systemic Effects of Chronic Stress. Chronic Stress (Thousand Oaks). 2017;1. Epub 20170410. doi: 10.1177/2470547017692328. PubMed PMID: 28856337; PubMed Central PMCID: PMCPMC5573220.
147. Connor SA, Elegheert J, Xie Y, Craig AM. Pumping the brakes: suppression of synapse development by MDGA-neuroligin interactions. Curr Opin Neurobiol. 2019;57:71-80. Epub 20190214. doi: 10.1016/j.conb.2019.01.002. PubMed PMID: 30771697.
148. Liu DD, Lu JM, Zhao QR, Hu C, Mei YA. Growth differentiation factor-15 promotes glutamate release in medial prefrontal cortex of mice through upregulation of T-type calcium channels. Sci Rep. 2016;6:28653. Epub 20160629. doi: 10.1038/srep28653. PubMed PMID: 27353765; PubMed Central PMCID: PMCPMC4926092.

149. Vezyroglou A, Akilapa R, Barwick K, Koene S, Brownstein CA, Holder-Espinasse M, et al. The Phenotypic Continuum of ATP1A3-Related Disorders. Neurology. 2022;99(14):e1511-e26. Epub 20220718. doi: 10.1212/wnl.0000000000200927. PubMed PMID: 36192182; PubMed Central PMCID: PMCPMC9576304.
150. Guidi J, Lucente M, Sonino N, Fava GA. Allostatic Load and Its Impact on Health: A Systematic Review. Psychother Psychosom. 2021;90(1):11-27. Epub 20200814. doi: 10.1159/000510696. PubMed PMID: 32799204.
151. Zhao J, Xue E, Zhou S, Zhang M, Jiang F, Wu W, et al. Allostatic load increases the incidence and risk of adverse prognosis in inflammatory bowel disease. Aliment Pharmacol Ther. 2024;60(8):1062-74. Epub 20240821. doi: 10.1111/apt.18217. PubMed PMID: 39166843.
152. Le Naour J, Montégut L, Joseph A, Garbin K, Vacchelli E, Kroemer G, et al. Improved Swiss-rolling method for histological analyses of colon tissue. MethodsX. 2022;9:101630. Epub 20220209. doi: 10.1016/j.mex.2022.101630. PubMed PMID: 35242614; PubMed Central PMCID: PMCPMC8861817.
153. Xue J, Chen J, Shen Q, Chan D, Li J, Tanguay AP, et al. Addition of High Molecular Weight Hyaluronic Acid to Fibroblast-Like Stromal Cells Modulates Endogenous Hyaluronic Acid Metabolism and Enhances Proteolytic Processing and Secretion of Versican. Cells. 2020;9(7). Epub 20200713. doi: 10.3390/cells9071681. PubMed PMID: 32668663; PubMed Central PMCID: PMCPMC7407811.
154. Jeon H, Xie J, Jeon Y, Jung KJ, Gupta A, Chang W, et al. Statistical Power Analysis for Designing Bulk, Single-Cell, and Spatial Transcriptomics Experiments: Review, Tutorial, and Perspectives. Biomolecules. 2023;13(2). Epub 20230124. doi: 10.3390/biom13020221. PubMed PMID: 36830591; PubMed Central PMCID: PMCPMC9952882.
155. Chan DD, Li J, Luo W, Predescu DN, Cole BJ, Plaas A. Pirfenidone reduces subchondral bone loss and fibrosis after murine knee cartilage injury. J Orthop Res. 2018;36(1):365-76. Epub 20170721. doi: 10.1002/jor.23635. PubMed PMID: 28646530; PubMed Central PMCID: PMCPMC5742076.
156. Martin M. Cutadapt removes adapter sequences from high-throughput sequencing reads. EMBnetjournal. 2011;17:10-2.
157. Dobin A, Davis CA, Schlesinger F, Drenkow J, Zaleski C, Jha S, et al. STAR: ultrafast universal RNA-seq aligner. Bioinformatics. 2013;29(1):15-21. Epub 20121025. doi: 10.1093/bioinformatics/bts635. PubMed PMID: 23104886; PubMed Central PMCID: PMCPMC3530905.
158. Liao Y, Smyth GK, Shi W. featureCounts: an efficient general purpose program for assigning sequence reads to genomic features. Bioinformatics. 2014;30(7):923-30. Epub 20131113. doi: 10.1093/bioinformatics/btt656. PubMed PMID: 24227677.
159. Robinson MD, McCarthy DJ, Smyth GK. edgeR: a Bioconductor package for differential expression analysis of digital gene expression data. Bioinformatics. 2010;26(1):139-40. Epub 20091111. doi: 10.1093/bioinformatics/btp616. PubMed PMID: 19910308; PubMed Central PMCID: PMCPMC2796818.
160. McCarthy DJ, Chen Y, Smyth GK. Differential expression analysis of multifactor RNA-Seq experiments with respect to biological variation. Nucleic Acids Res. 2012;40(10):4288-97. Epub 20120128. doi: 10.1093/nar/gks042. PubMed PMID: 22287627; PubMed Central PMCID: PMCPMC3378882.
161. Feser WJ, Fingerlin TE, Strand MJ, Glueck DH. CALCULATING AVERAGE POWER FOR THE BENJAMINI-HOCHBERG PROCEDURE. J Stat Theory Appl. 2009;8(3):325-52. PubMed PMID: 27818616; PubMed Central PMCID: PMCPMC5095931.
162. Naqib A, Poggi S, Wang W, Hyde M, Kunstman K, Green SJ. Making and Sequencing Heavily Multiplexed, High-Throughput 16S Ribosomal RNA Gene Amplicon Libraries Using a Flexible, Two-Stage PCR Protocol. Methods Mol Biol. 2018;1783:149-69. doi: 10.1007/978-1-4939-7834-2_7. PubMed PMID: 29767361.
163. Bolyen E, Rideout JR, Dillon MR, Bokulich NA, Abnet CC, Al-Ghalith GA, et al. Reproducible, interactive, scalable and extensible microbiome data science using QIIME 2. Nat Biotechnol. 2019;37(8):852-7. doi: 10.1038/s41587-019-0209-9. PubMed PMID: 31341288; PubMed Central PMCID: PMCPMC7015180.
164. Zhang J, Kobert K, Flouri T, Stamatakis A. PEAR: a fast and accurate Illumina Paired-End reAd mergeR. Bioinformatics. 2014;30(5):614-20. Epub 20131018. doi: 10.1093/bioinformatics/btt593. PubMed PMID: 24142950; PubMed Central PMCID: PMCPMC3933873.
165. Callahan BJ, McMurdie PJ, Rosen MJ, Han AW, Johnson AJ, Holmes SP. DADA2: High-resolution sample inference from Illumina amplicon data. Nat Methods. 2016;13(7):581-3. Epub 20160523. doi: 10.1038/nmeth.3869. PubMed PMID: 27214047; PubMed Central PMCID: PMCPMC4927377.
166. Faith DP. Conservation evaluation and phylogenetic diversity. Biological Conservation. 1992;61(1):1-10. doi: https://doi.org/10.1016/0006-3207(92)91201-3.

167. Shannon CE. A Mathematical Theory of Communication. Bell System Technical Journal. 1948;27(3):379-423. doi: https://doi.org/10.1002/j.1538-7305.1948.tb01338.x.
168. Simpson EH. Measurement of Diversity. Nature. 1949;163(4148):688-. doi: 10.1038/163688a0.
169. Bokulich NA, Kaehler BD, Rideout JR, Dillon M, Bolyen E, Knight R, et al. Optimizing taxonomic classification of marker-gene amplicon sequences with QIIME 2's q2-feature-classifier plugin. Microbiome. 2018;6(1):90. Epub 20180517. doi: 10.1186/s40168-018-0470-z. PubMed PMID: 29773078; PubMed Central PMCID: PMCPMC5956843.
170. Quast C, Pruesse E, Yilmaz P, Gerken J, Schweer T, Yarza P, et al. The SILVA ribosomal RNA gene database project: improved data processing and web-based tools. Nucleic Acids Research. 2013;41(D1):D590-D6. doi: 10.1093/nar/gks1219.

Fig. 1

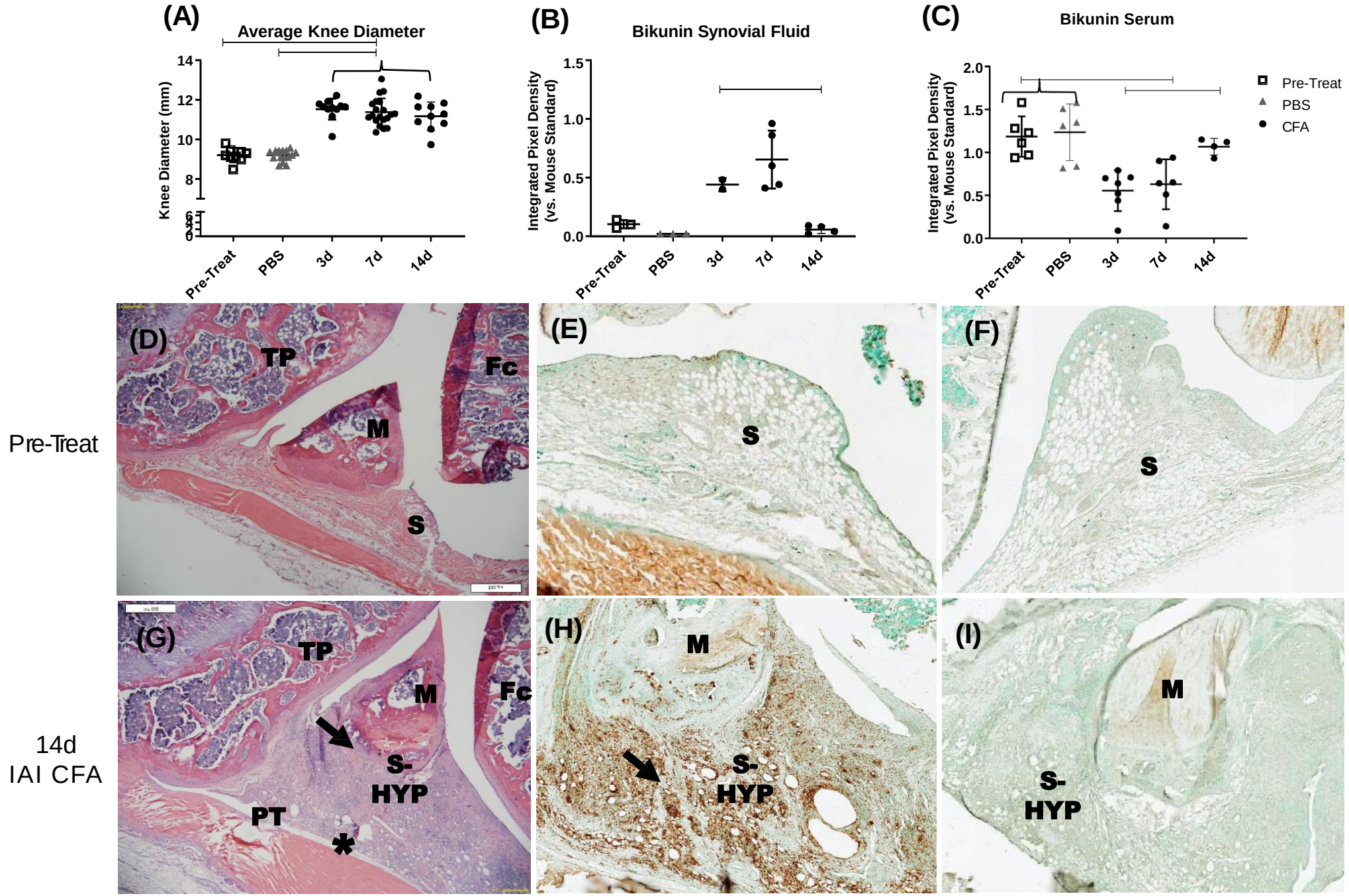
(A)
Average Knee Diameter
Knee Diameter (mm)
14
12
10
8
Pre-Treat
PBS
3d
7d
14d
(B)
Bikunin Synovial Fluid
Integrated Pixel Density (vs. Mouse Standard)
1.5
1.0
0.5
0.0
Pre-Treat
PBS
3d
7d
14d
(C)
Bikunin Serum
Integrated Pixel Density (vs. Mouse Standard)
2.0
1.5
1.0
0.5
0.0
Pre-Treat
PBS
3d
7d
14d
Pre-Treat
PBS
CFA
Pre-Treat
14d
IAI CFA
(D)
TP
Fc
M
S
(E)
S
(F)
S
(G)
TP
M
Fc
S-
HYP
PT
*
(H)
M
S-
HYP
(I)
M
S-
HYP

Fig. 2

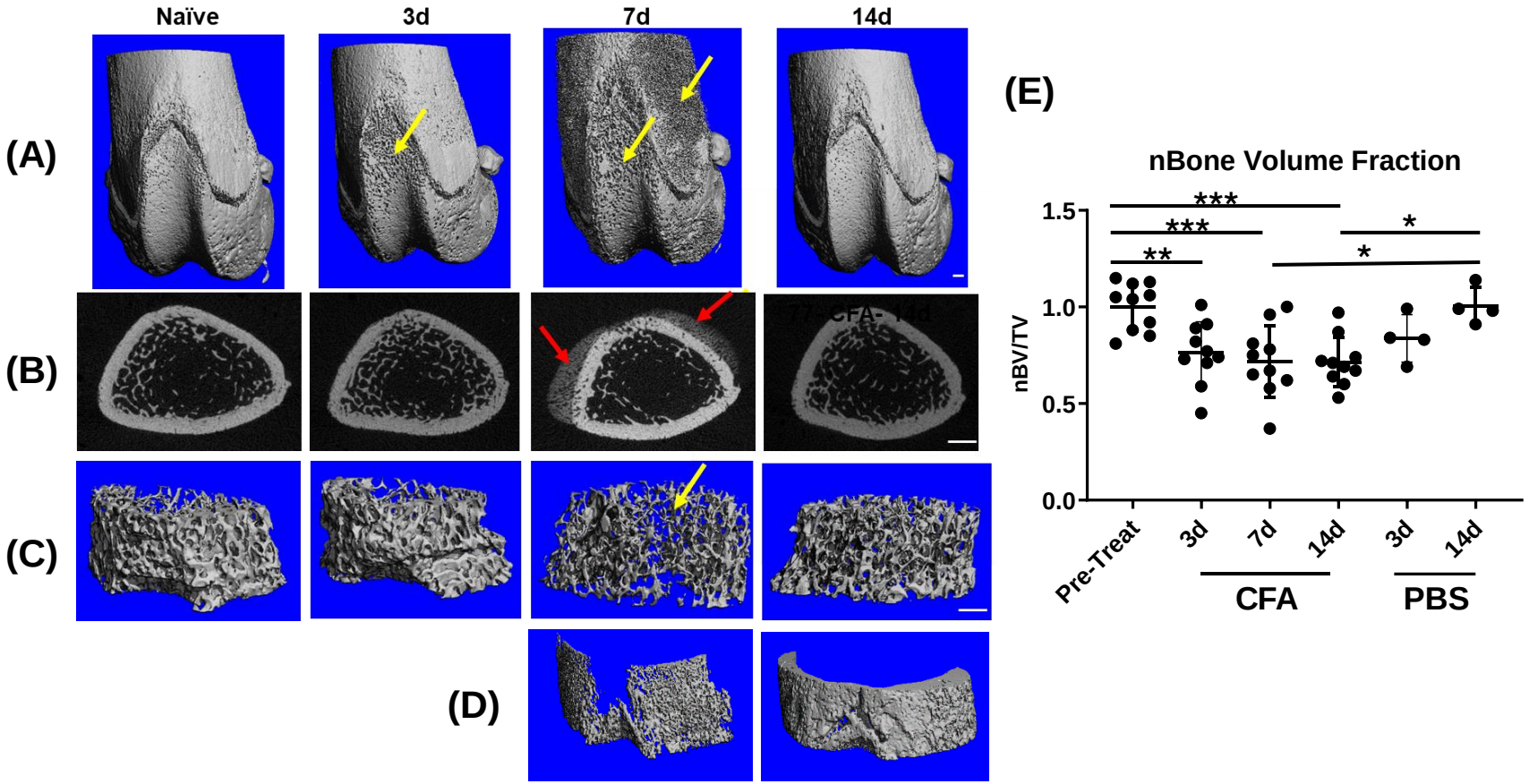
Naïve
3d
7d
14d
(A)
(B)
(C)
(D)
(E)
nBone Volume Fraction
nBV/TV
1.5
1.0
0.5
0.0
***
***
**
*
*
Pre-Treat
3d
7d
14d
3d
14d
CFA
PBS

Fig. 3

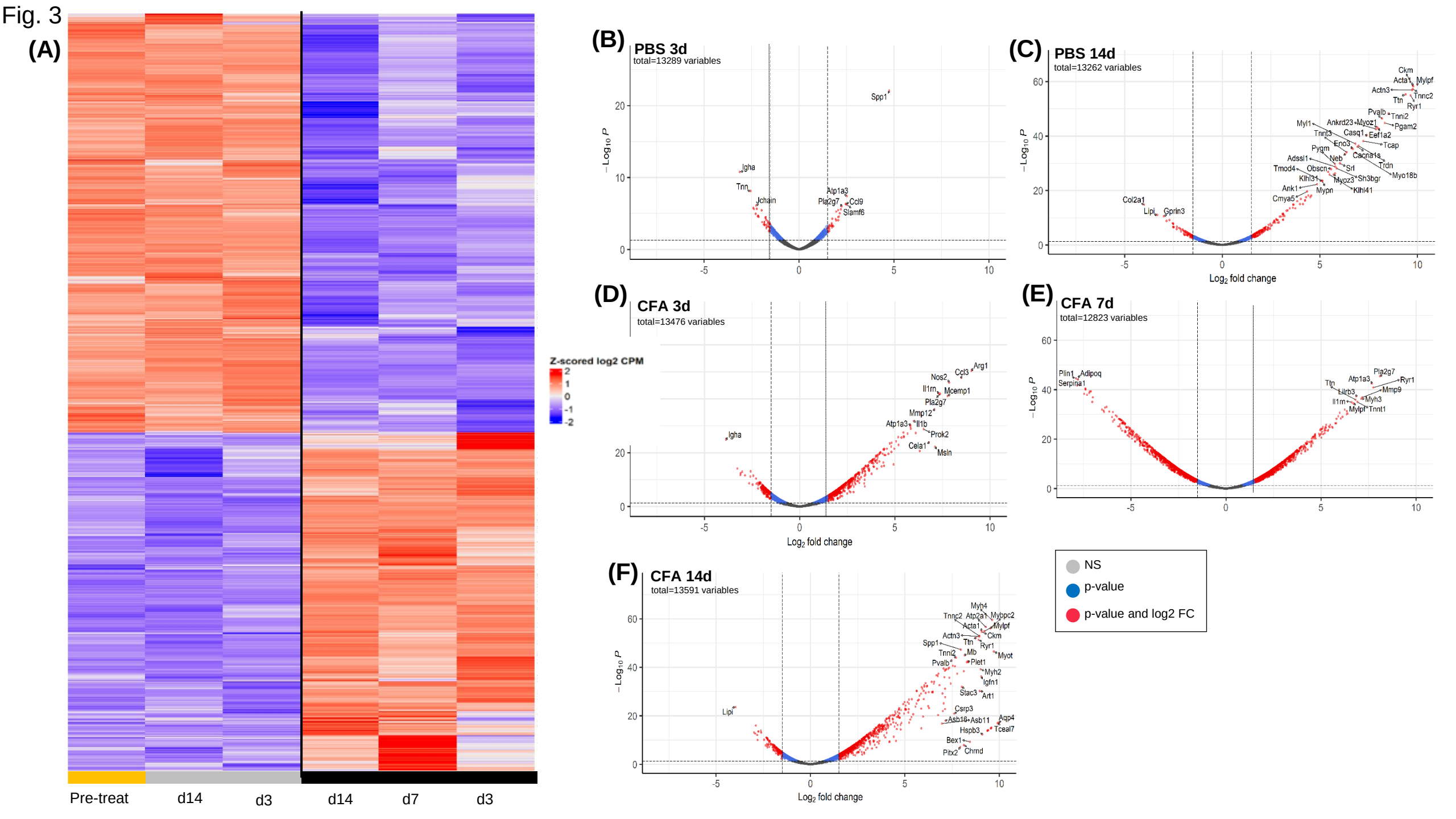
(A)
Pre-treat
d14
d3
d14
d7
d3
Z-scored log2 CPM
2
1
0
-1
-2
(B)
PBS 3d
total=13289 variables
Spp1
Igha
Tnn
Jchain
Atp1a3
Pla2g7
Ccl9
Slamf6
(C)
PBS 14d
total=13262 variables
Ckm
Acta1
Mylpf
Actn3
Tnnc2
Ttn
Ryr1
Pvalb
Tnni2
Myl1
Ankrd23
Myoz1
Pgam2
Tnnt3
Casq1
Eef1a2
Tcap
Pygm
Eno3
Adssl1
Neb
Cacna1s
Trdn
Tmod4
Obscn
Srl
Klhl31
Myoz3
Sh3bgr
Myo18b
Ank1
Mypn
Klhl41
Cmya5
Col2a1
Lipi
Gprin3
(D)
CFA 3d
total=13476 variables
Arg1
Ccl3
Nos2
Il1rn
Mcemp1
Pla2g7
Mmp12
Atp1a3
Il1b
Prok2
Cela1
Msln
Igha
(E)
CFA 7d
total=12823 variables
Plin1
Adipoq
Serpina1
Pla2g7
Atp1a3
Ryr1
Ttn
Lilrb3
Mmp9
Il1rn
Myh3
Mylpf
Tnnt1
(F)
CFA 14d
total=13591 variables
Myh4
Tnnc2
Atp2a1
Mybpc2
Acta1
Mylpf
Actn3
Ckm
Spp1
Ttn
Ryr1
Tnni2
Mb
Myot
Pvalb
Plet1
Myh2
Igfn1
Stac3
Art1
Lipi
Csrp3
Asb16
Asb11
Aqp4
Hspb3
Tceal7
Bex1
Pitx2
Chrmd
$-\text{Log}_{10}\,P$
Log_2 fold change
NS
p-value
p-value and log2 FC

Fig. 4

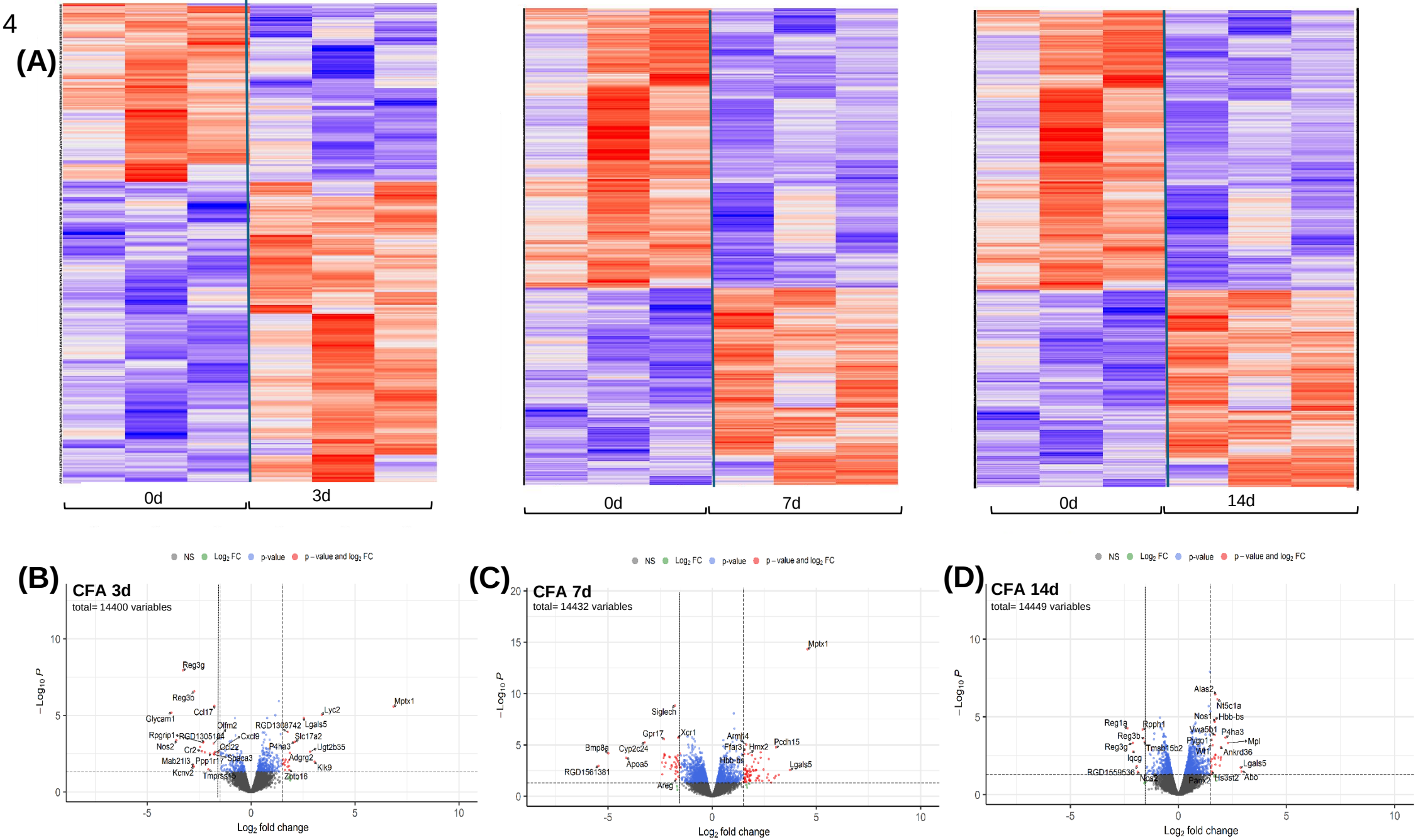
(A)
0d
3d
0d
7d
0d
14d
(B)
CFA 3d
total= 14400 variables
NS
Log2 FC
p-value
p – value and log2 FC
−Log10 P
Log2 fold change
Reg3g
Reg3b
Ccl17
Glycam1
Olfm2
RGD1308742
Lgals5
Lyc2
Mptx1
Rpgrip1
RGD1305184
Cxcl9
Slc17a2
Nos2
Cr2
Ccl22
P4ha3
Ugt2b35
Mab21l3
Ppp1r17
Spaca3
Adgrg2
Kcnv2
Tmprss13
Klk9
Zbtb16
(C)
CFA 7d
total= 14432 variables
Mptx1
Siglech
Gpr17
Xcr1
Armh4
Bmp8a
Cyp2c24
Ffar3
Hmx2
Pcdh15
Apoa5
Hbb-bs
Lgals5
RGD1561381
Areg
(D)
CFA 14d
total= 14449 variables
Alas2
Nt5c1a
Nos1
Hbb-bs
Reg1a
Rpph1
Vwa5b1
P4ha3
Reg3b
Pygo1
Mpl
Reg3g
Tmsb15b2
Wt1
Ankrd36
Iqcg
Lgals5
RGD1559536
Nos2
Pax2
Hs3st2
Abo

Fig. 5

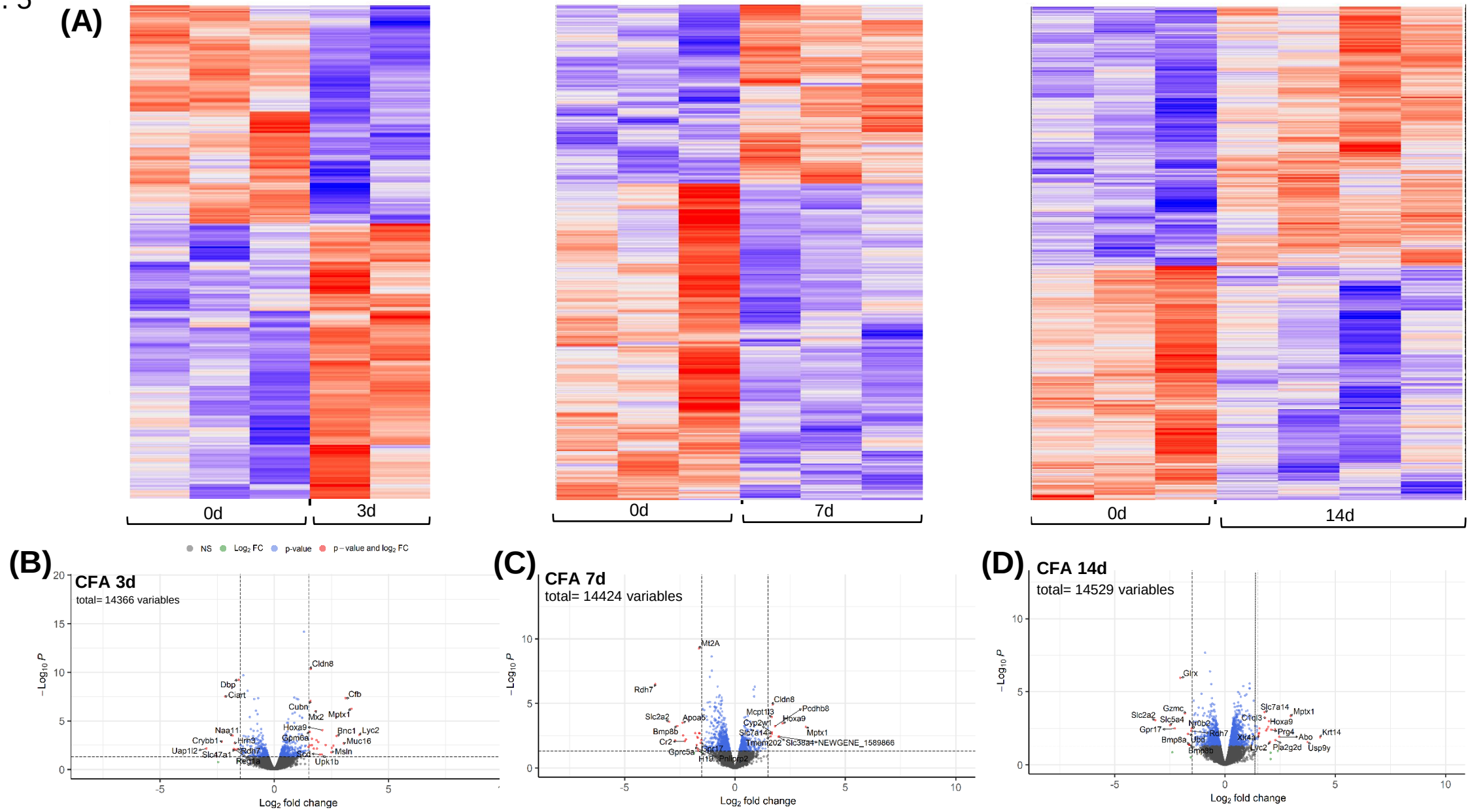
(A)
0d
3d
0d
7d
0d
14d
NS
Log2 FC
p-value
p – value and log2 FC
(B)
CFA 3d
total= 14366 variables
Log2 fold change
(C)
CFA 7d
total= 14424 variables
Log2 fold change
(D)
CFA 14d
total= 14529 variables
Log2 fold change

Fig. 6

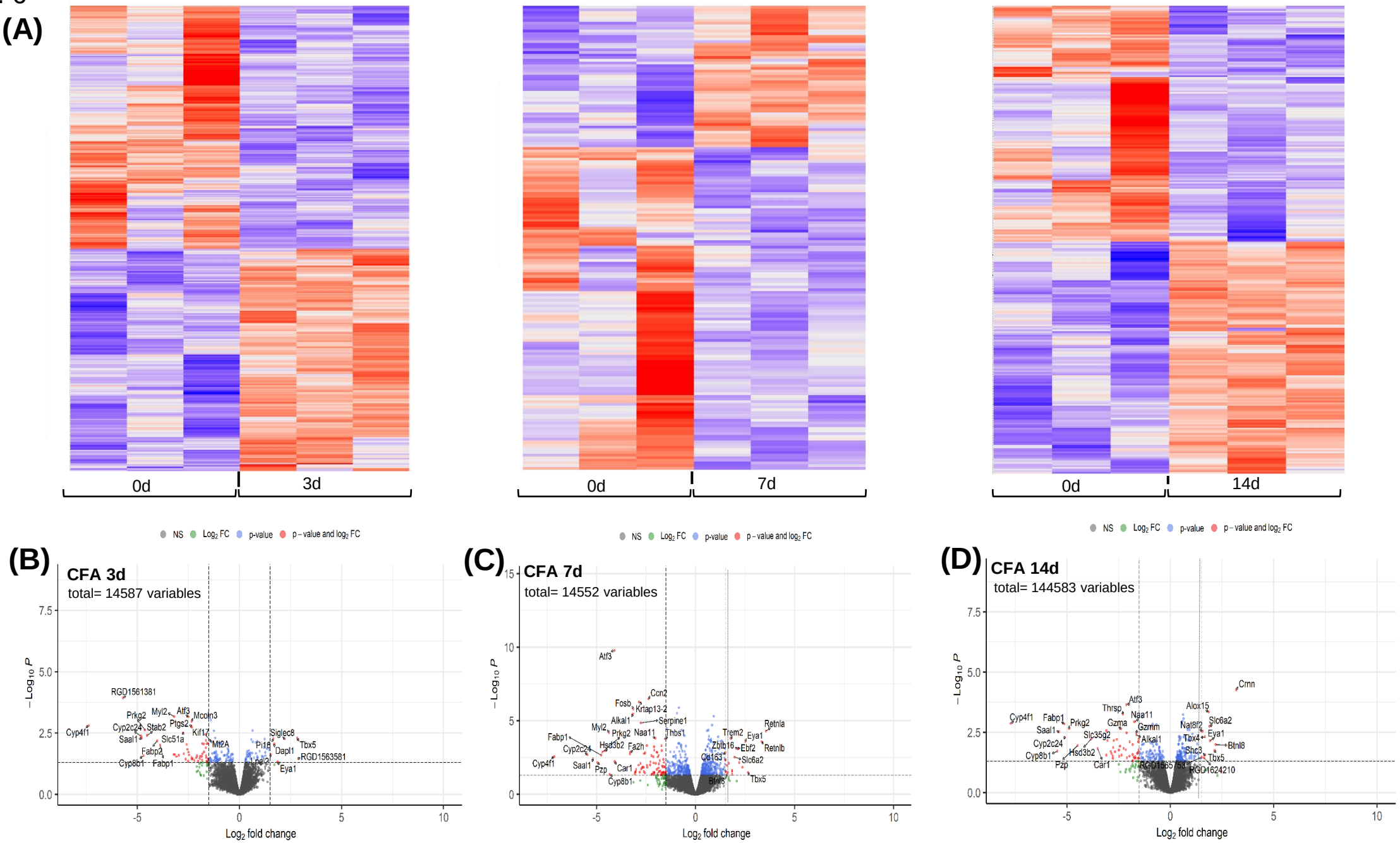
(A)
0d
3d
0d
7d
0d
14d
NS
Log2 FC
p-value
p-value and log2 FC
(B)
CFA 3d
total= 14587 variables
(C)
CFA 7d
total= 14552 variables
(D)
CFA 14d
total= 144583 variables
−Log10 P
Log2 fold change

Fig. 7

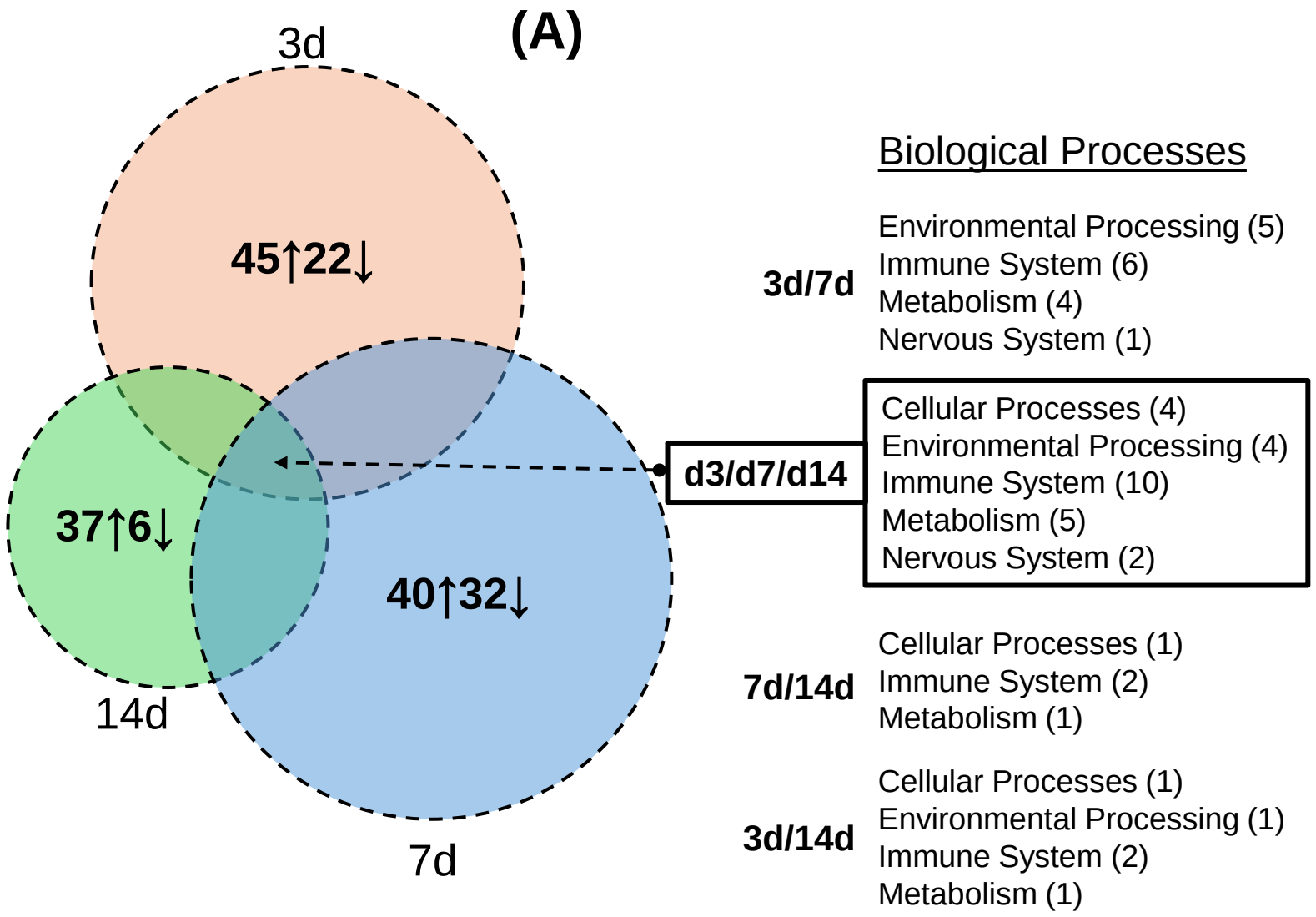
(A)
3d
45↑22↓
37↑6↓
40↑32↓
14d
7d
Biological Processes
3d/7d
Environmental Processing (5)
Immune System (6)
Metabolism (4)
Nervous System (1)
d3/d7/d14
Cellular Processes (4)
Environmental Processing (4)
Immune System (10)
Metabolism (5)
Nervous System (2)
7d/14d
Cellular Processes (1)
Immune System (2)
Metabolism (1)
3d/14d
Cellular Processes (1)
Environmental Processing (1)
Immune System (2)
Metabolism (1)

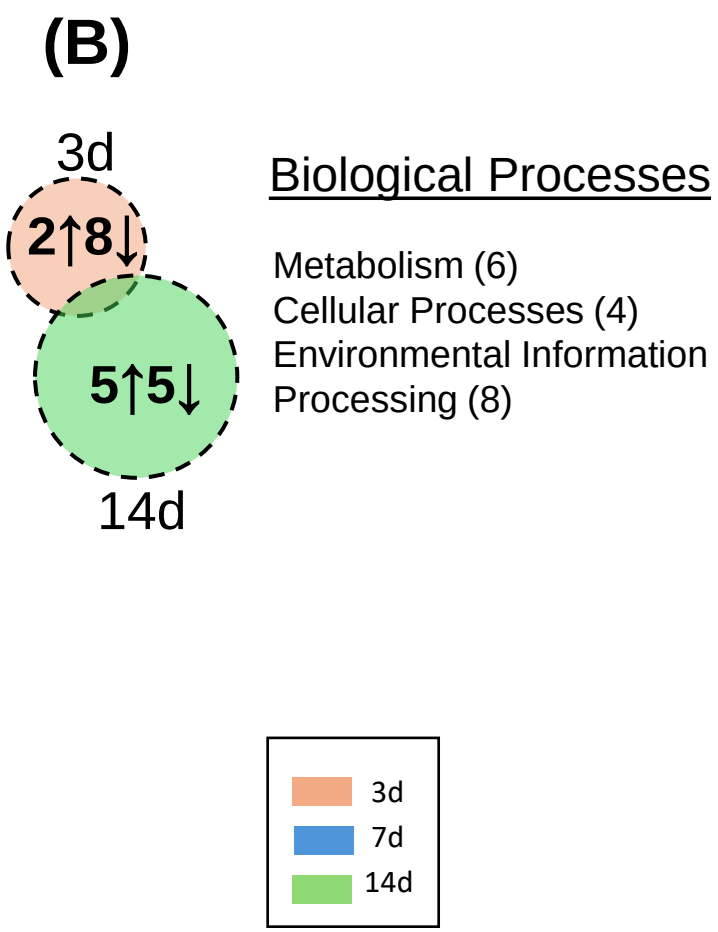
(B)
3d
2↑8↓
5↑5↓
14d
Biological Processes
Metabolism (6)
Cellular Processes (4)
Environmental Information Processing (8)
3d
7d
14d

Fig. 8

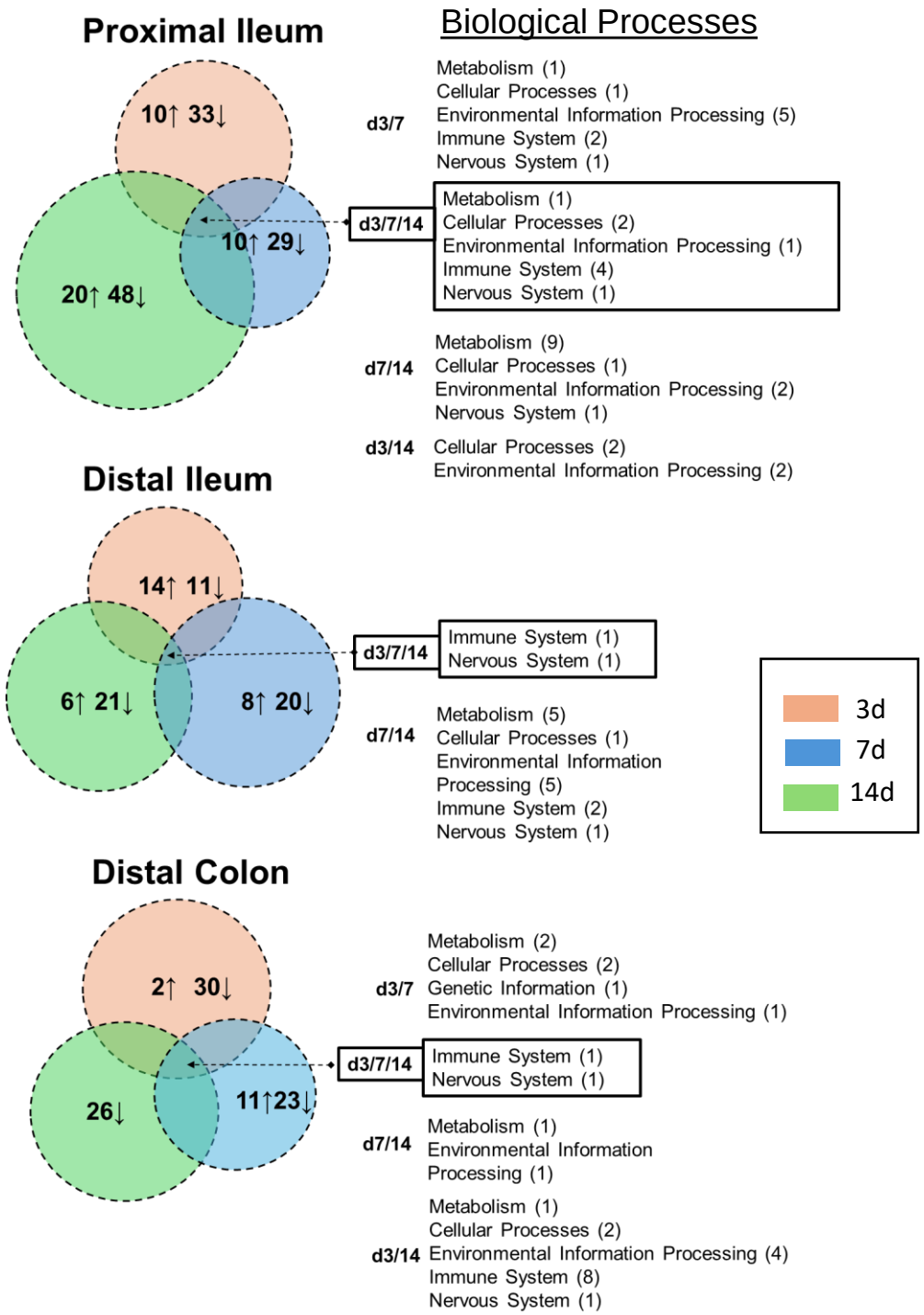
Biological Processes
Proximal Ileum
10↑ 33↓
10↑ 29↓
20↑ 48↓
d3/7
Metabolism (1)
Cellular Processes (1)
Environmental Information Processing (5)
Immune System (2)
Nervous System (1)
d3/7/14
Metabolism (1)
Cellular Processes (2)
Environmental Information Processing (1)
Immune System (4)
Nervous System (1)
d7/14
Metabolism (9)
Cellular Processes (1)
Environmental Information Processing (2)
Nervous System (1)
d3/14
Cellular Processes (2)
Environmental Information Processing (2)
Distal Ileum
14↑ 11↓
6↑ 21↓
8↑ 20↓
d3/7/14
Immune System (1)
Nervous System (1)
d7/14
Metabolism (5)
Cellular Processes (1)
Environmental Information Processing (5)
Immune System (2)
Nervous System (1)
3d
7d
14d
Distal Colon
2↑ 30↓
26↓
11↑23↓
d3/7
Metabolism (2)
Cellular Processes (2)
Genetic Information (1)
Environmental Information Processing (1)
d3/7/14
Immune System (1)
Nervous System (1)
d7/14
Metabolism (1)
Environmental Information Processing (1)
d3/14
Metabolism (1)
Cellular Processes (2)
Environmental Information Processing (4)
Immune System (8)
Nervous System (1)

Fig. 9

		3d				7d				14d			
		SYN	PI	DI	Co	SYN	PI	DI	Co	SYN	PI	DI	Co
Environmental Information Processing	Chemokine signaling	↑	↓	↓	↓	↑	↔	↓	↓	↑	↓	↓	↔
	Cytokine−cytokine receptor interaction	↑	↔	↔	↓	↑	↓	↓	↓	↑	↔	↓	↓
	IL−17 signaling	↑	↓	↔	↔	↑	↔	↔	↔	↑	↔	↔	↓
	JAK−STAT signaling	↑	↓	↔	↔	↔	↓	↓	↓	↔	↔	↔	↔
	NF−kappa B signaling	↑	↔	↔	↓	↑	↔	↔	↓	↑	↔	↔	↔
	TNF signaling	↑	↓	↓	↔	↔	↔	↓	↔	↑	↓	↓	↔
	PPAR signaling pathway	↓	↓	↓	↓	↓	↓	↓	↓	↓	↓	↓	↓
Immune System	Antigen processing and presentation	↔	↓	↔	↓	↑	↓	↓	↓	↑	↓	↓	↔
	B cell receptor signaling	↔	↓	↔	↓	↑	↔	↓	↓	↑	↓	↔	↔
	C−type lectin receptor signaling	↑	↓	↔	↓	↑	↔	↓	↓	↑	↔	↔	↔
	Apoptosis	↔	↔	↔	↔	↑	↓	↓	↓	↑	↓	↓	↔
	Efferocytosis	↑	↓	↔	↔	↑	↔	↓	↔	↔	↔	↓	↔
	Lysosome	↑	↔	↔	↔	↑	↓	↔	↔	↑	↓	↓	↔
	Necroptosis	↑	↓	↔	↔	↑	↓	↓	↔	↑	↓	↓	↔
	NK cell mediated cytotoxicity	↔	↓	↔	↔	↑	↓	↓	↓	↑	↔	↓	↔
	NOD−like receptor signaling	↑	↓	↔	↔	↑	↔	↔	↓	↔	↓	↓	↓
	Phagosome	↑	↓	↔	↓	↑	↓	↓	↓	↑	↓	↓	↔
	T cell receptor signaling	↔	↓	↔	↓	↑	↔	↓	↓	↑	↓	↓	↔
	Th1 and Th2 cell differentiation	↔	↓	↓	↓	↑	↓	↓	↓	↑	↓	↓	↔
	Th17 cell differentiation	↔	↓	↔	↓	↑	↓	↓	↓	↑	↓	↓	↔
	Toll−like receptor signaling	↑	↓	↔	↔	↑	↓	↓	↓	↑	↓	↓	↔
Metabolism	Oxidative phosphorylation	↑	↓	↓	↓	↑	↓	↓	↓	↑	↓	↓	↓

Fig. 10

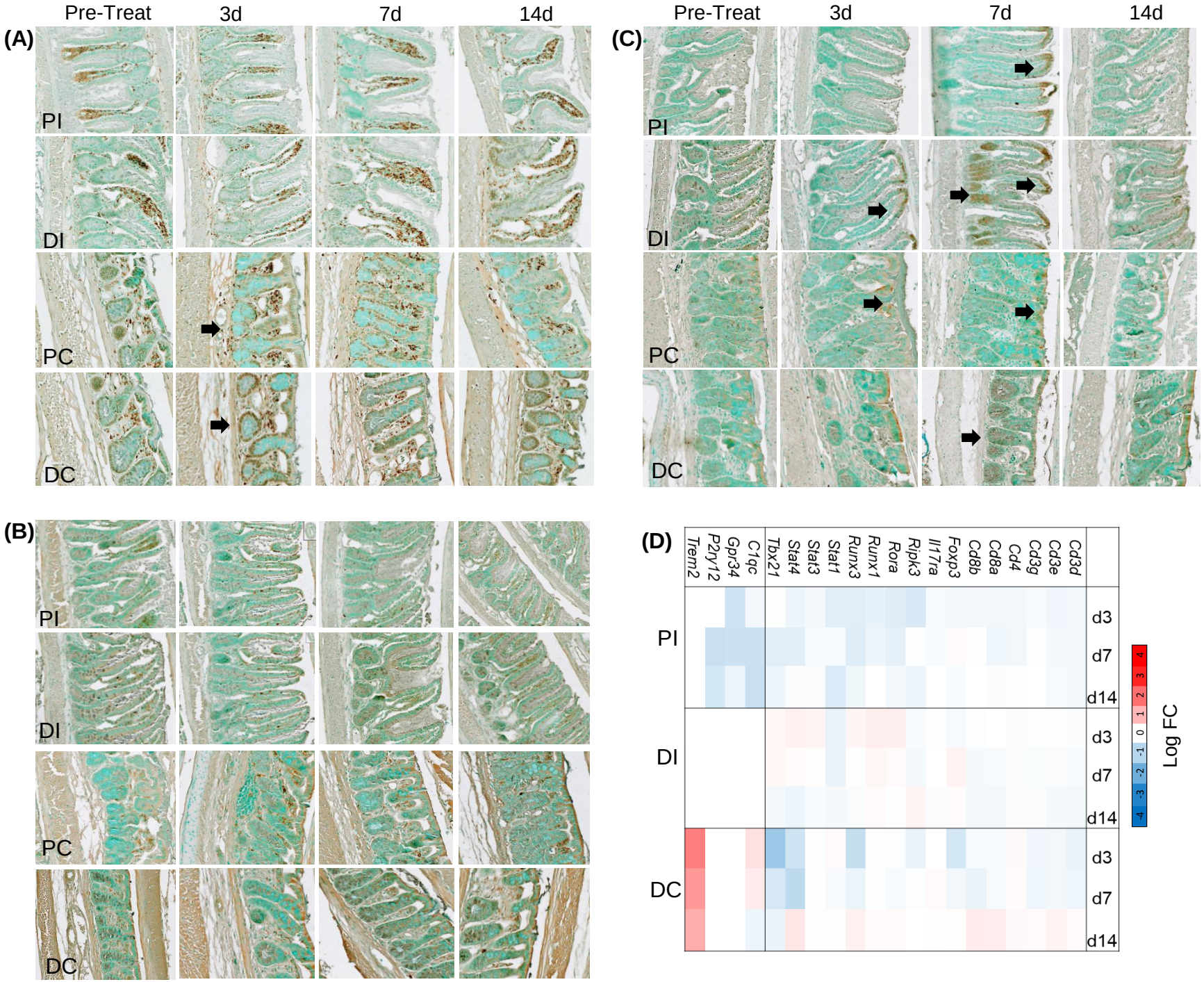
(A)
Pre-Treat
3d
7d
14d
PI
DI
PC
DC
(B)
PI
DI
PC
DC
(C)
Pre-Treat
3d
7d
14d
PI
DI
PC
DC
(D)
Trem2
P2ry12
Gpr34
C1qc
Tbx21
Stat4
Stat3
Stat1
Runx3
Runx1
Rora
Ripk3
Il17ra
Foxp3
Cd8b
Cd8a
Cd4
Cd3g
Cd3e
Cd3d
PI
DI
DC
d3
d7
d14
Log FC
-4
-3
-2
-1
0
1
2
3
4

Fig. 11

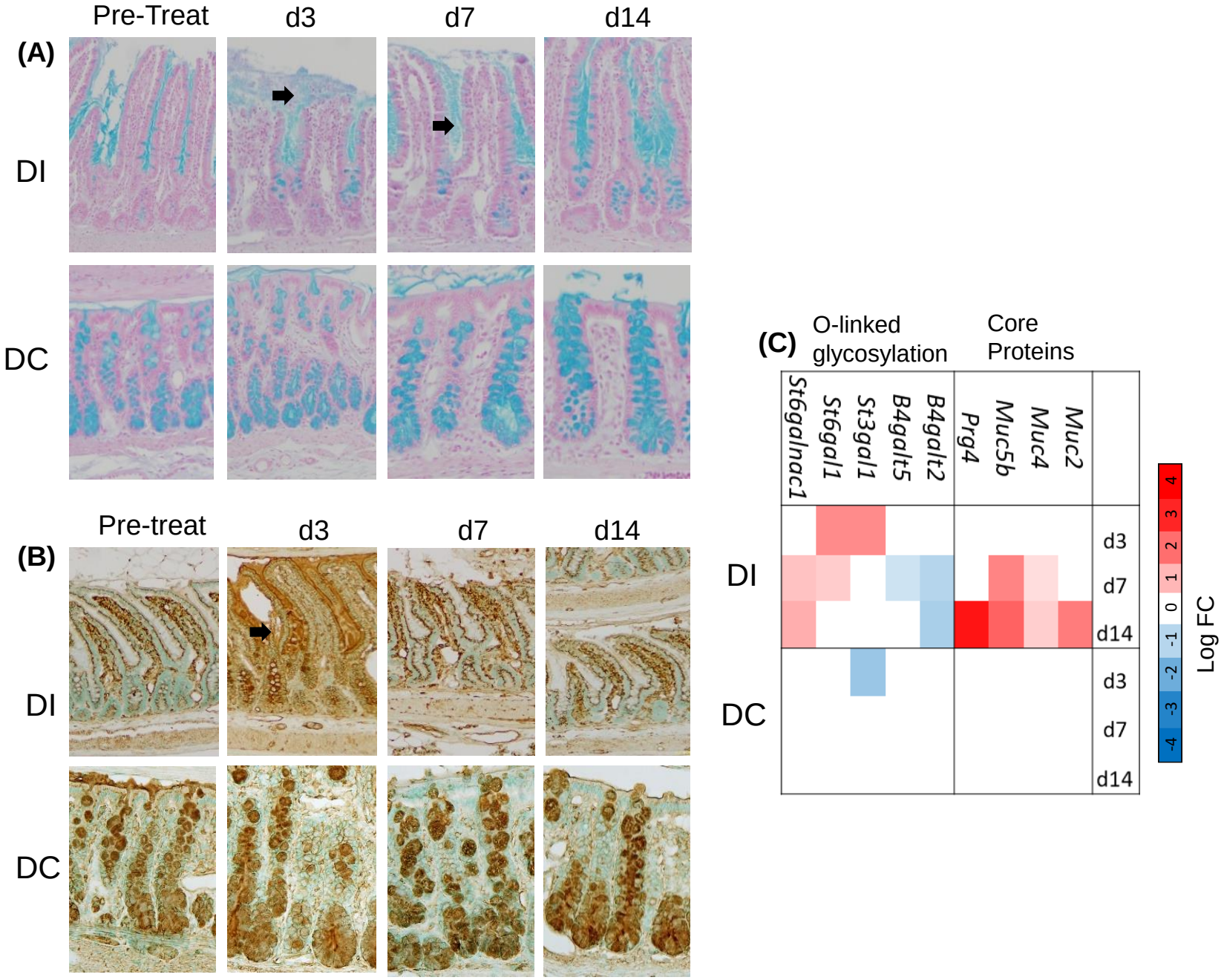
(A)
Pre-Treat
d3
d7
d14
DI
DC
(B)
Pre-treat
d3
d7
d14
DI
DC
(C)
O-linked glycosylation
Core Proteins
St6galnac1
St6gal1
St3gal1
B4galt5
B4galt2
Prg4
Muc5b
Muc4
Muc2
DI
DC
d3
d7
d14
d3
d7
d14
4
3
2
1
0
-1
-2
-3
-4
Log FC

Fig. 12

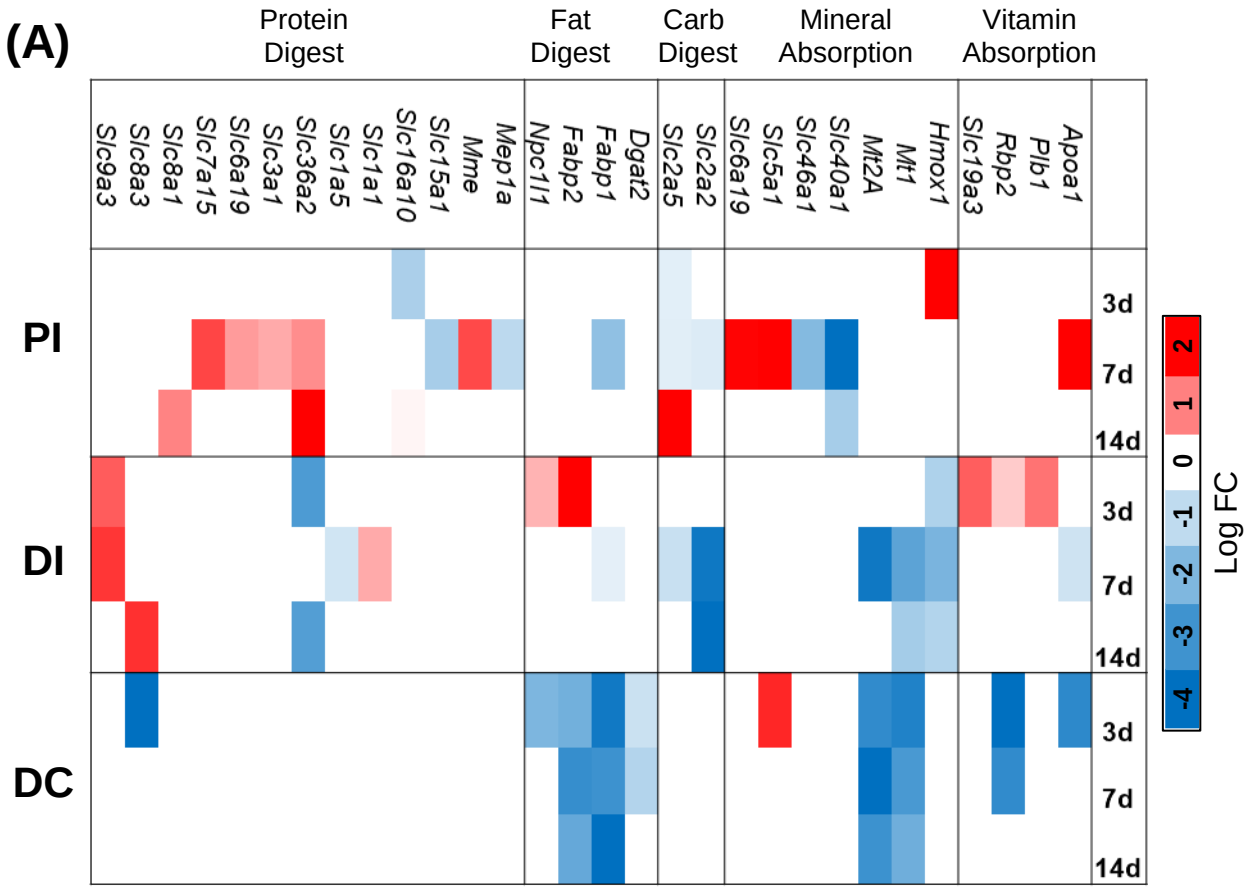
(A)
Protein Digest
Fat Digest
Carb Digest
Mineral Absorption
Vitamin Absorption
Slc9a3
Slc8a3
Slc8a1
Slc7a15
Slc6a19
Slc3a1
Slc36a2
Slc1a5
Slc1a1
Slc16a10
Slc15a1
Mme
Mep1a
Npc1l1
Fabp2
Fabp1
Dgat2
Slc2a5
Slc2a2
Slc6a19
Slc5a1
Slc46a1
Slc40a1
Mt2A
Mt1
Hmox1
Slc19a3
Rbp2
Plb1
Apoa1
PI
DI
DC
3d
7d
14d
2
1
0
-1
-2
-3
-4
Log FC

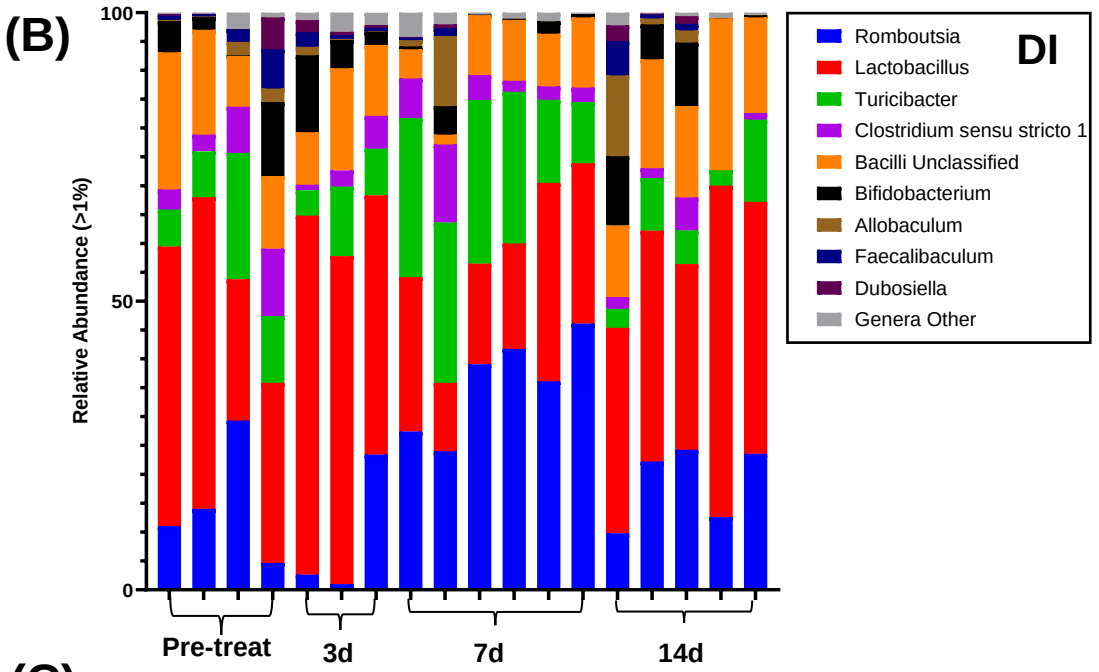
(B)
DI
Relative Abundance (>1%)
100
50
0
Pre-treat
3d
7d
14d
Romboutsia
Lactobacillus
Turicibacter
Clostridium sensu stricto 1
Bacilli Unclassified
Bifidobacterium
Allobaculum
Faecalibaculum
Dubosiella
Genera Other

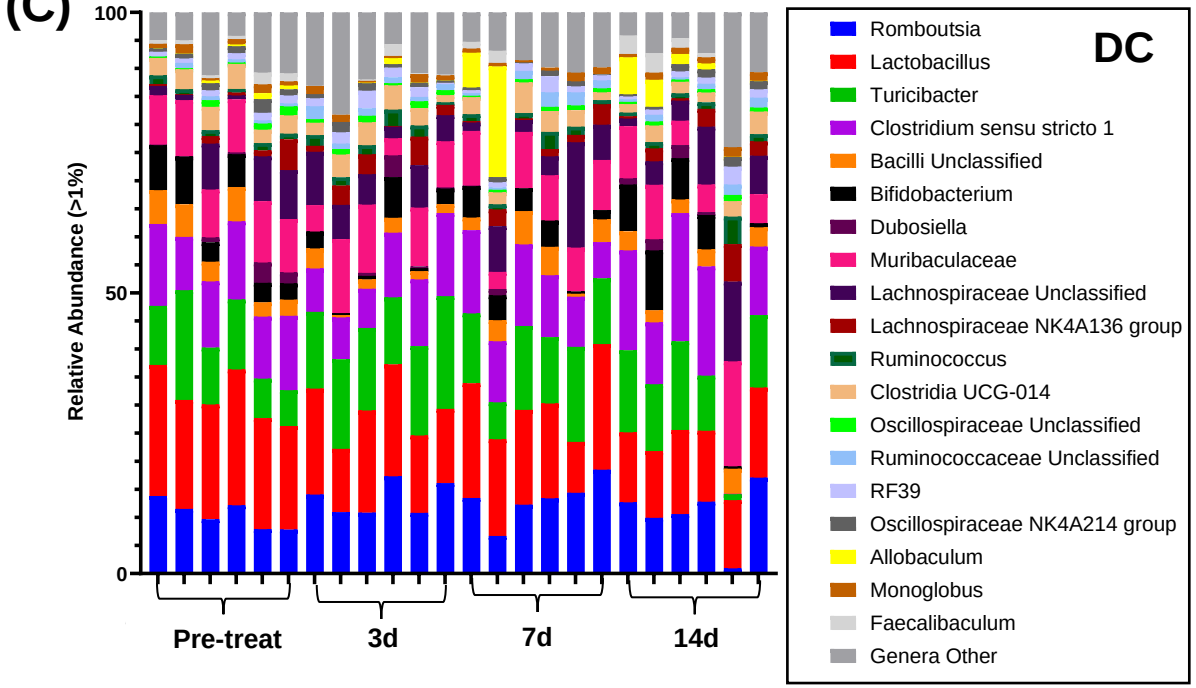
(C)
DC
Relative Abundance (>1%)
100
50
0
Pre-treat
3d
7d
14d
Romboutsia
Lactobacillus
Turicibacter
Clostridium sensu stricto 1
Bacilli Unclassified
Bifidobacterium
Dubosiella
Muribaculaceae
Lachnospiraceae Unclassified
Lachnospiraceae NK4A136 group
Ruminococcus
Clostridia UCG-014
Oscillospiraceae Unclassified
Ruminococcaceae Unclassified
RF39
Oscillospiraceae NK4A214 group
Allobaculum
Monoglobus
Faecalibaculum
Genera Other

Supporting Information Figures

Supporting Information Fig. S1

(A)

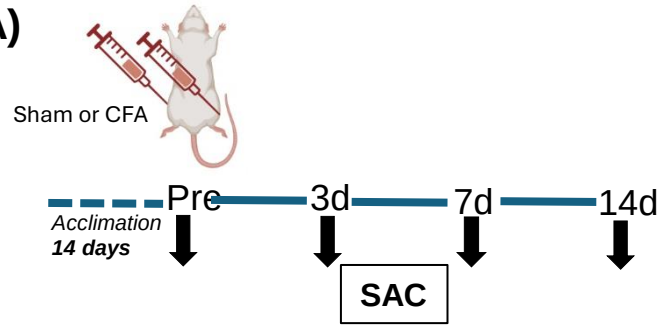

Joint diameter measurement, synovial fluid lavage, ileal and colonic feces, hind legs, ileum and colon tissues

(B)

STUDY GROUP	Cohort 1 SAC time: Pre treat	3d	7d	14d	Cohort 2 SAC time: Pre treat	3d	7d	14d
Naïve	4	-	-	-	6	-	-	-
IAI Saline	-	4	-	4	-	-	-	-
IA CFA	-	4	4	4	-	6	6	6

(C)

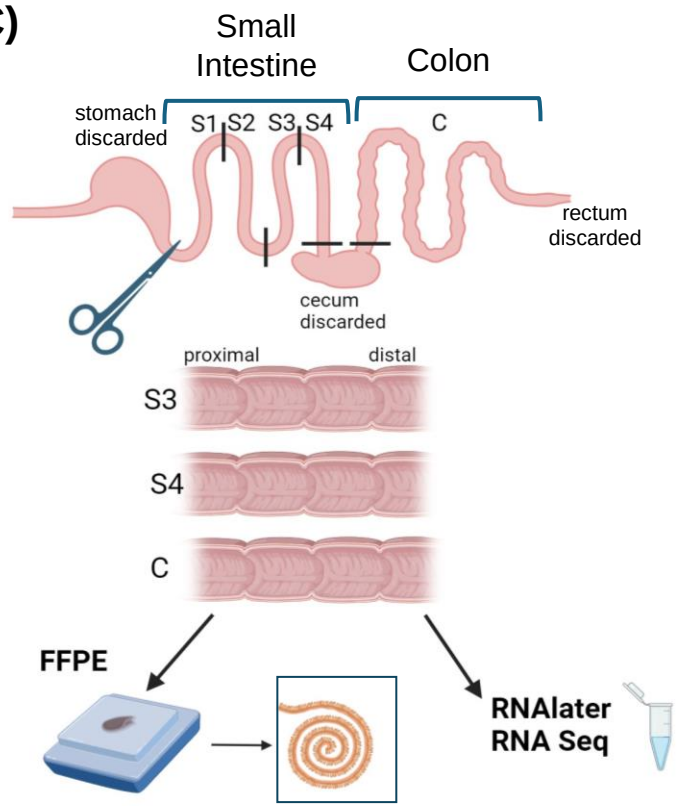

Alcian Blue Stain
Lectin Histochemistry

Supplemental Figure S2

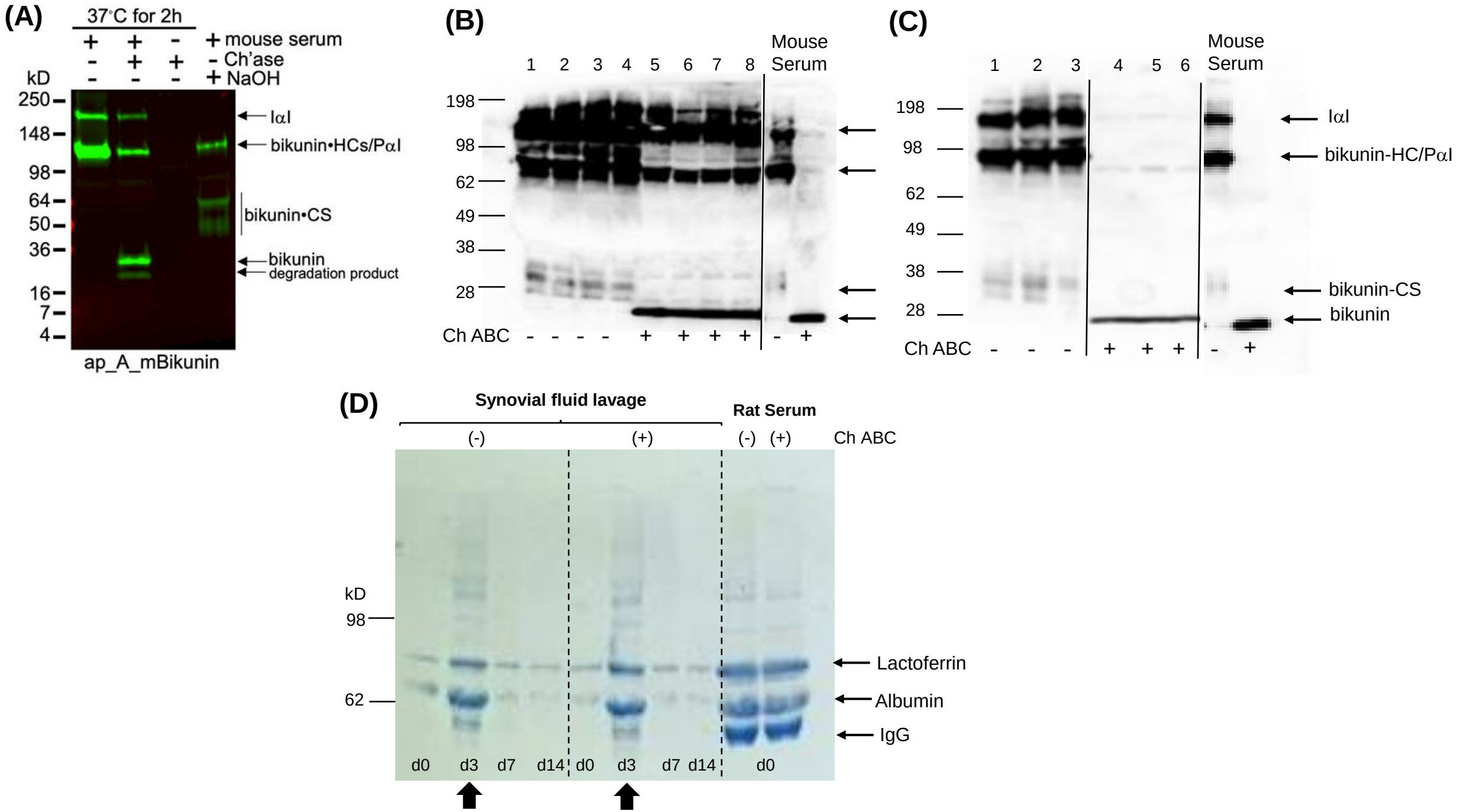

Supporting Information Fig. S3

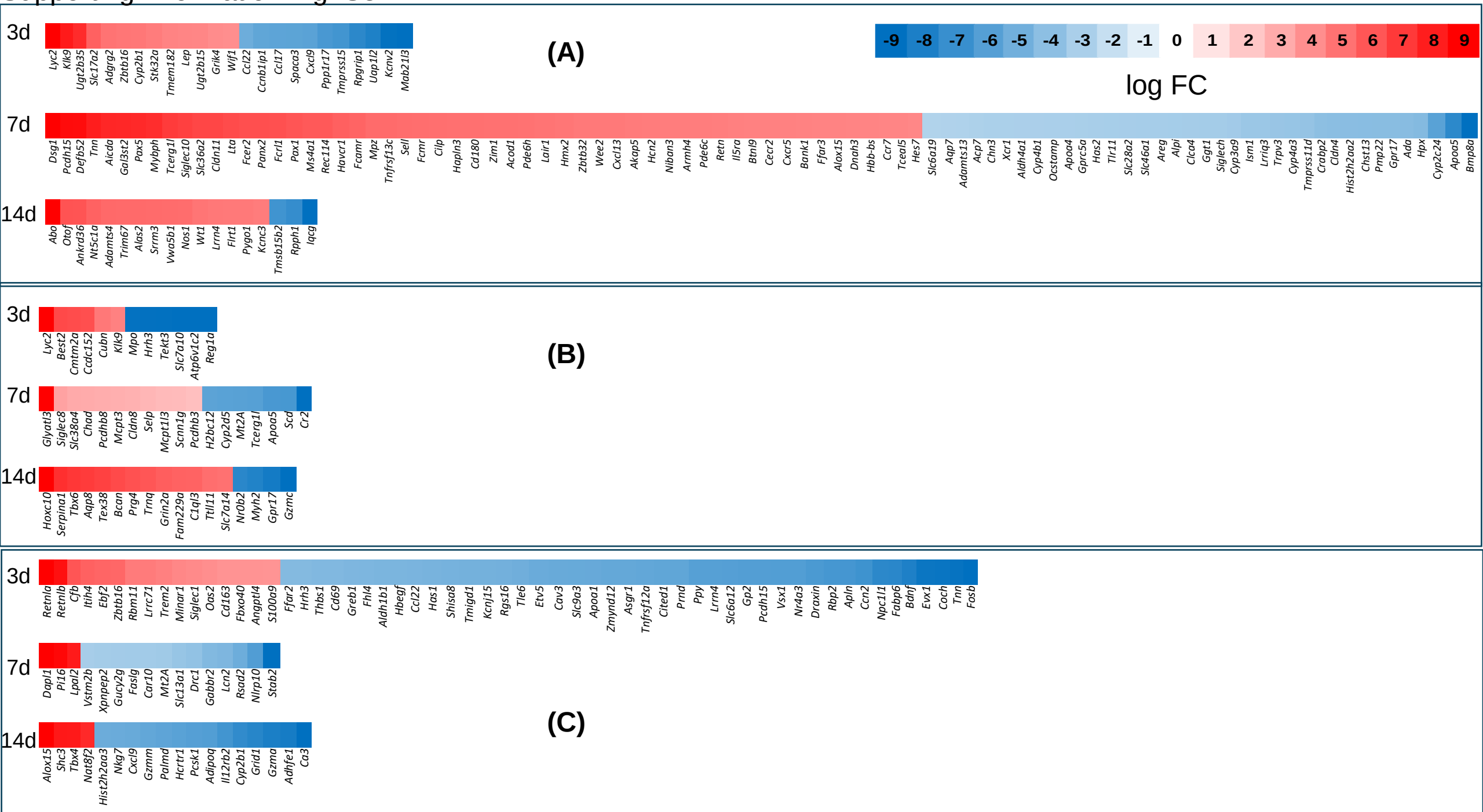

Supporting Information Fig. S4

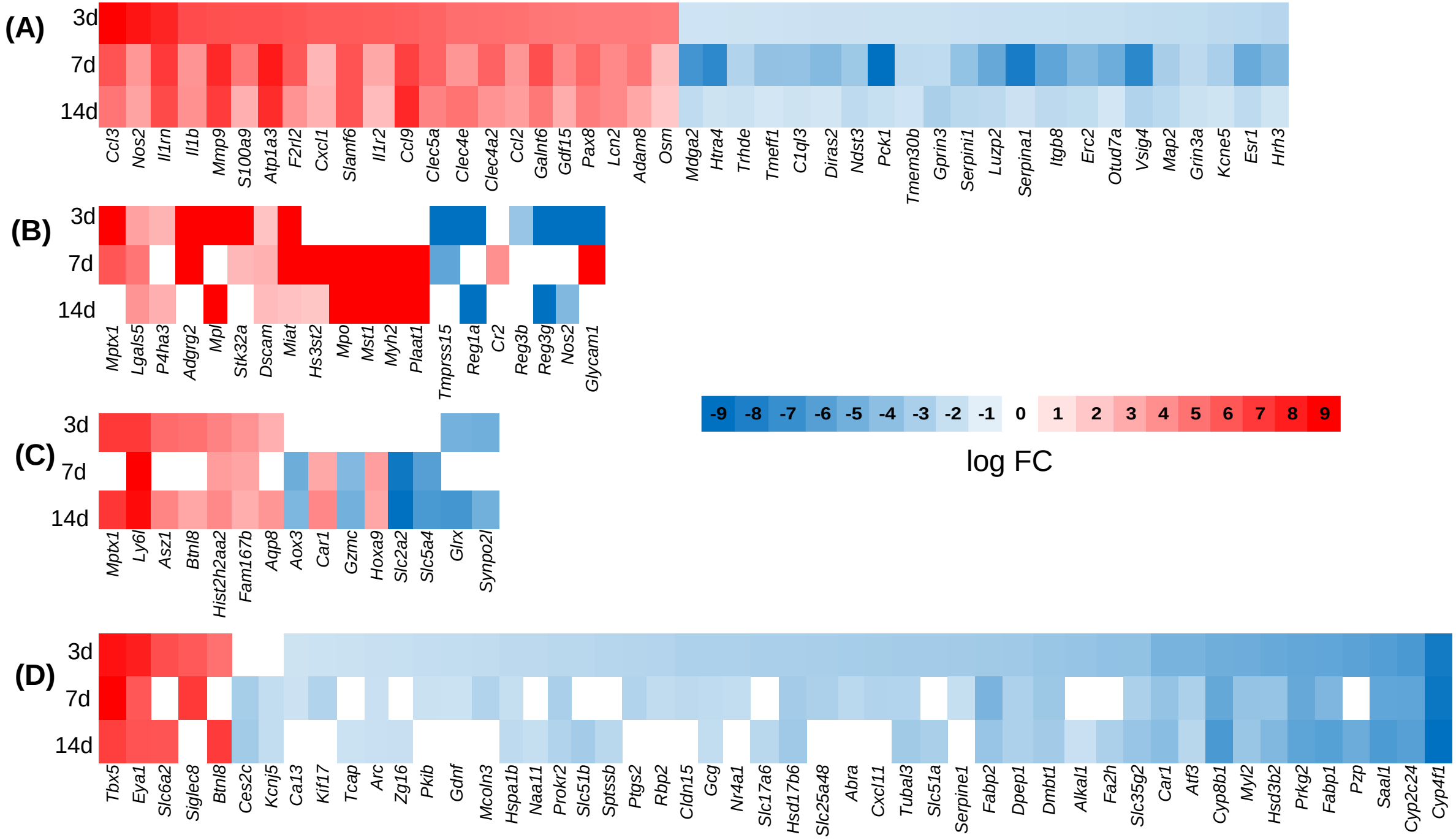

Supporting Information Fig. S5

SYN

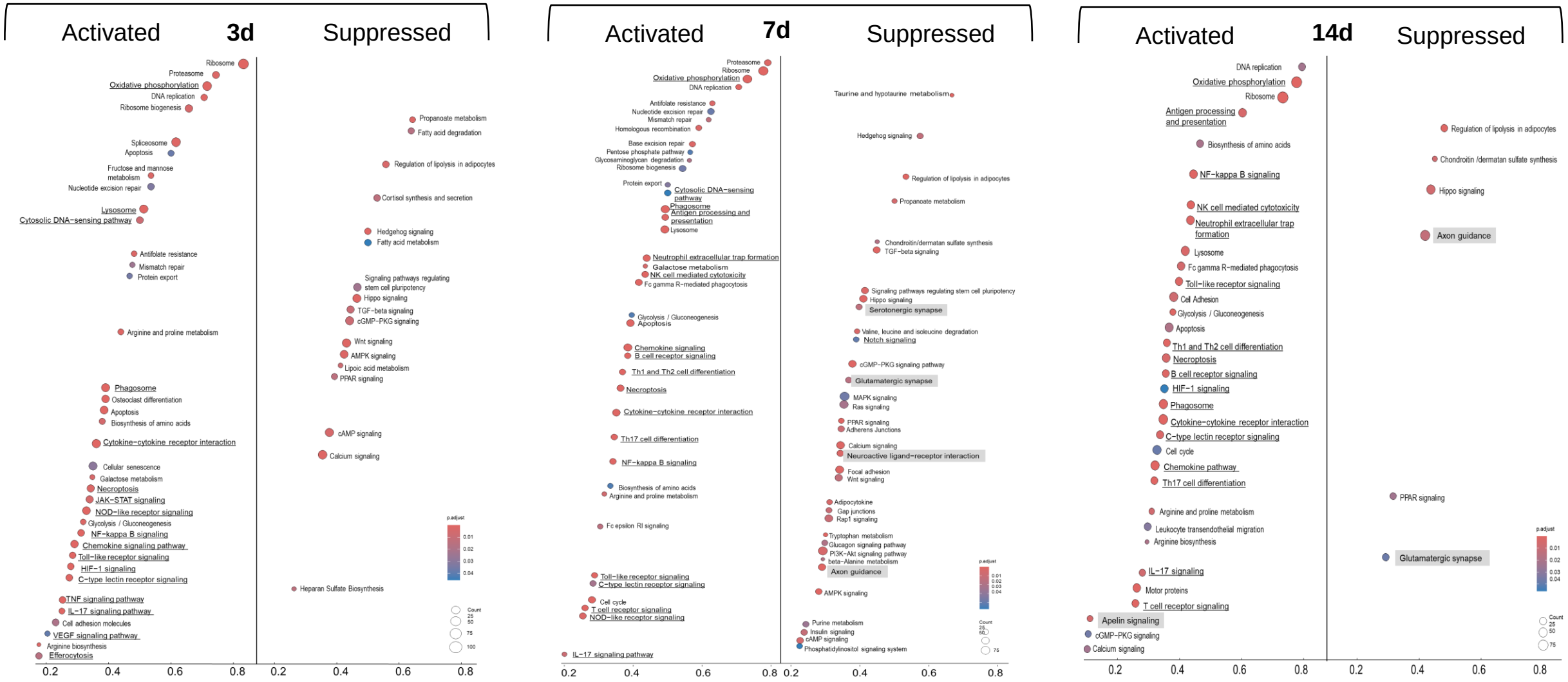

Supporting Information Fig. S6

SYN- PBS

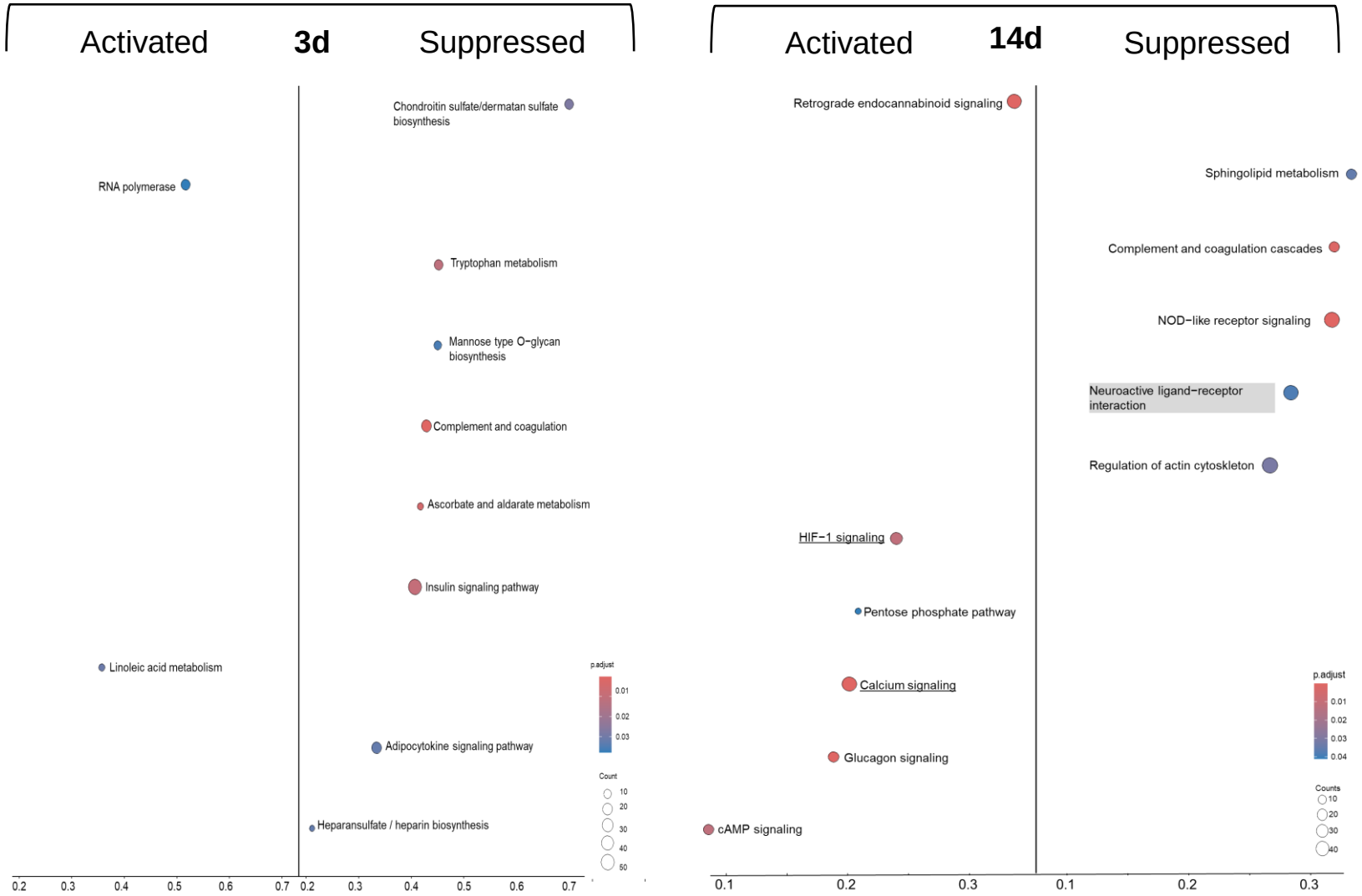

Supporting Information Fig. S7

Proximal Ileum- CFA

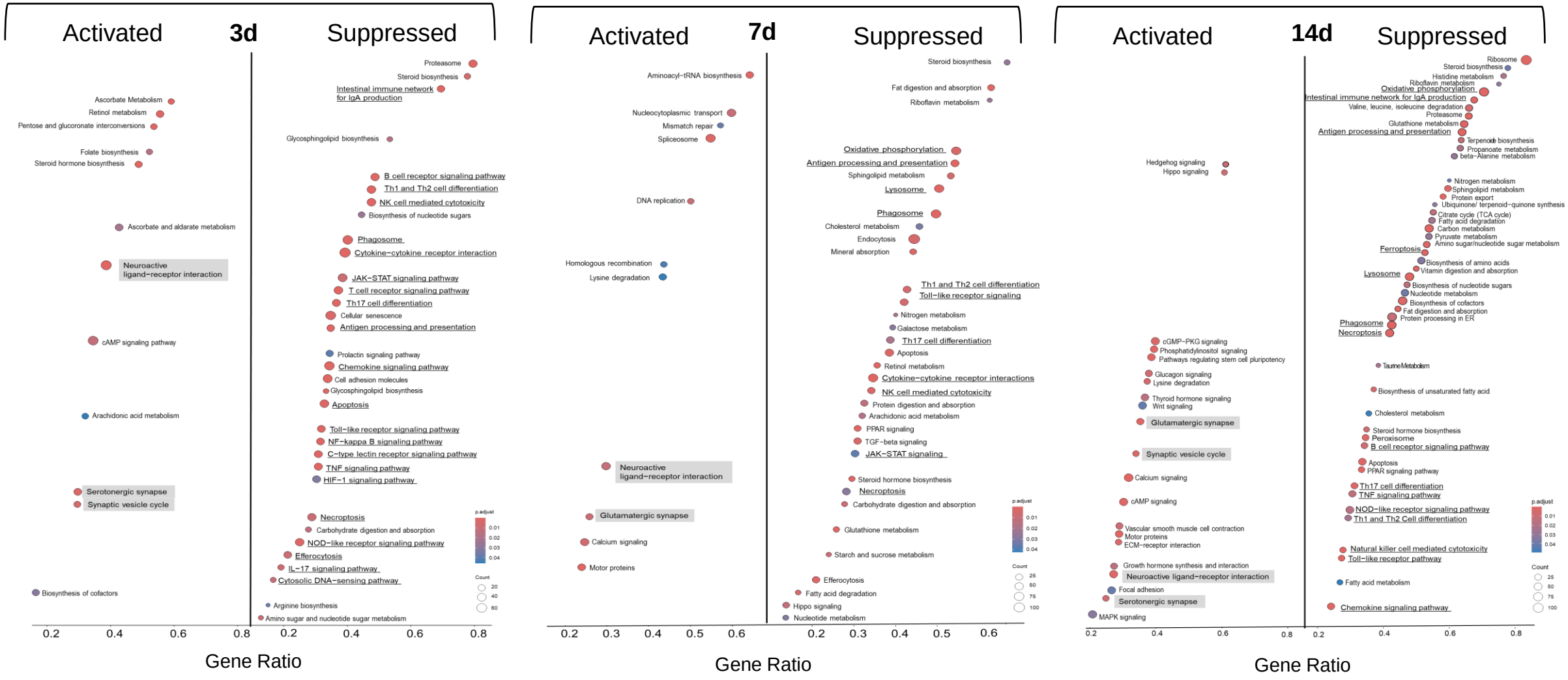

Supporting Information Fig. S8

Distal Ileum- CFA

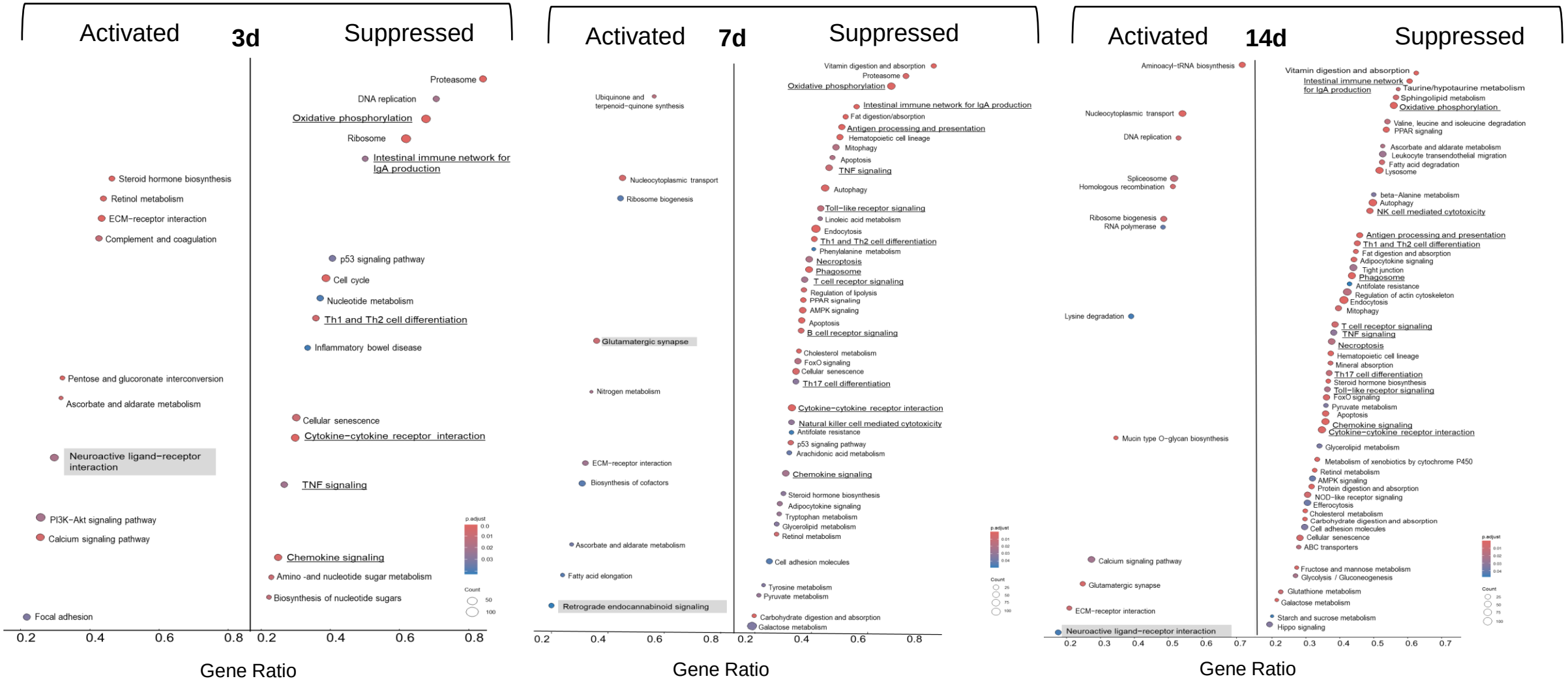

Supporting Information Fig. S9

Distal Colon- CFA

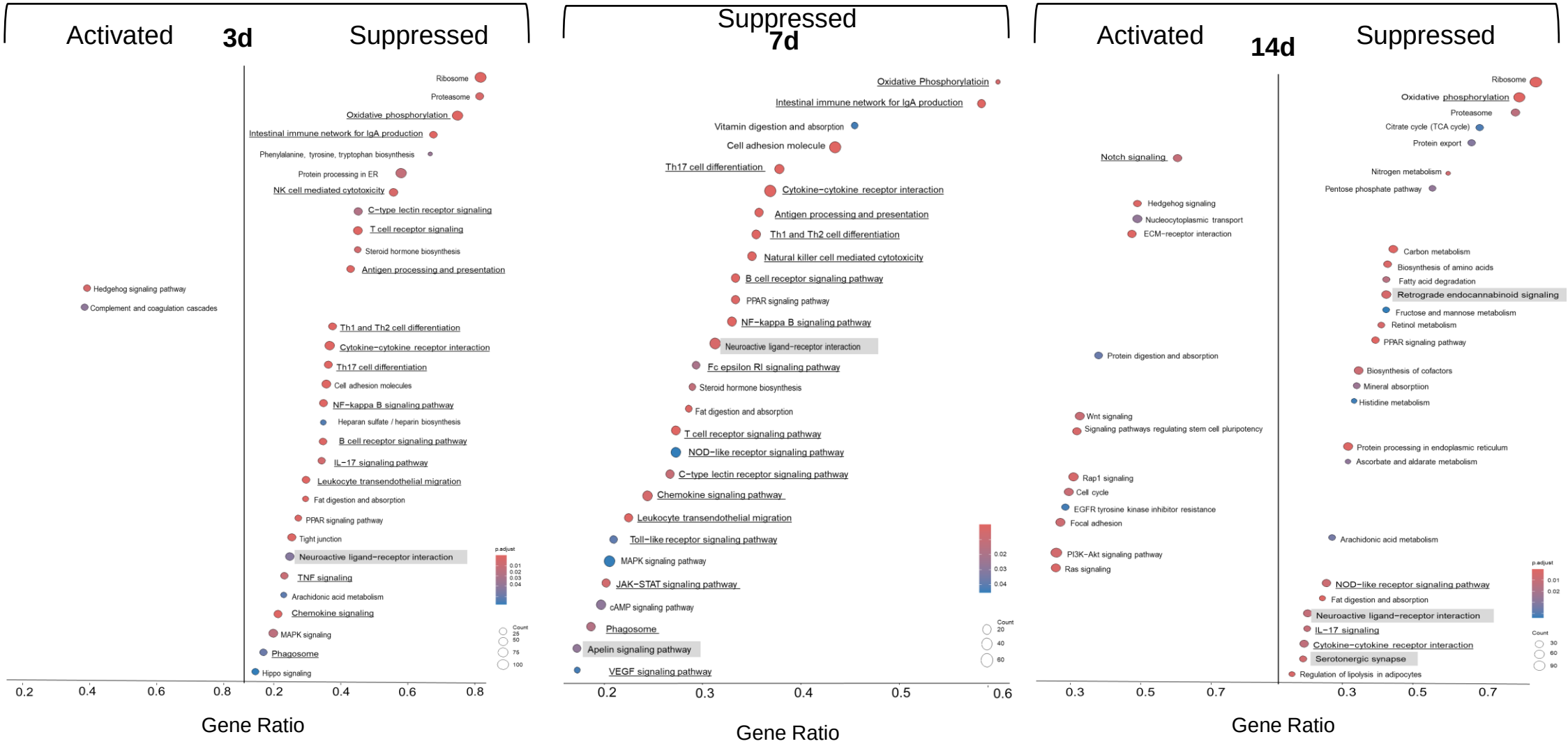

Supporting Information Fig. S10

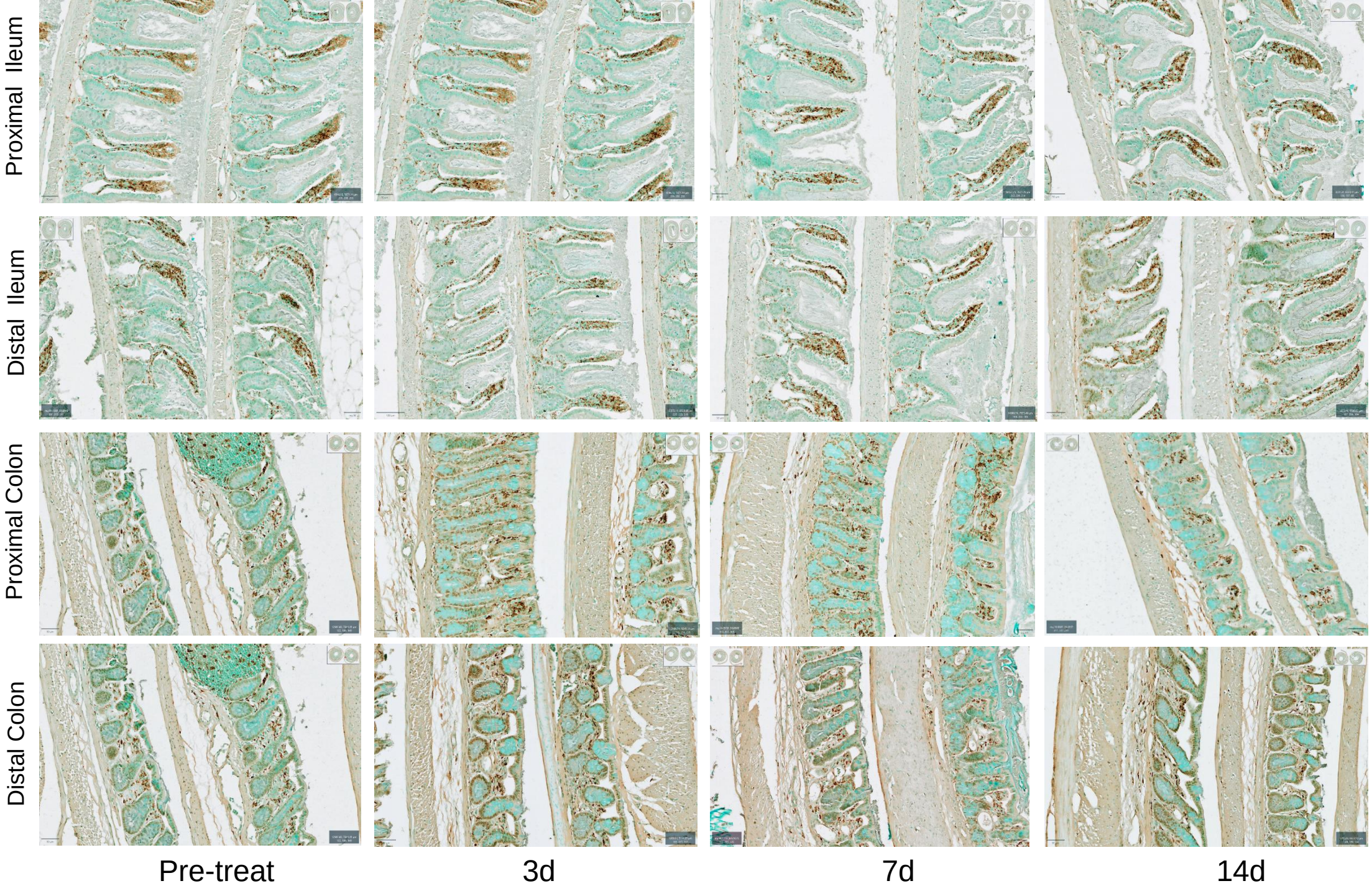

Supporting Information Fig. S11

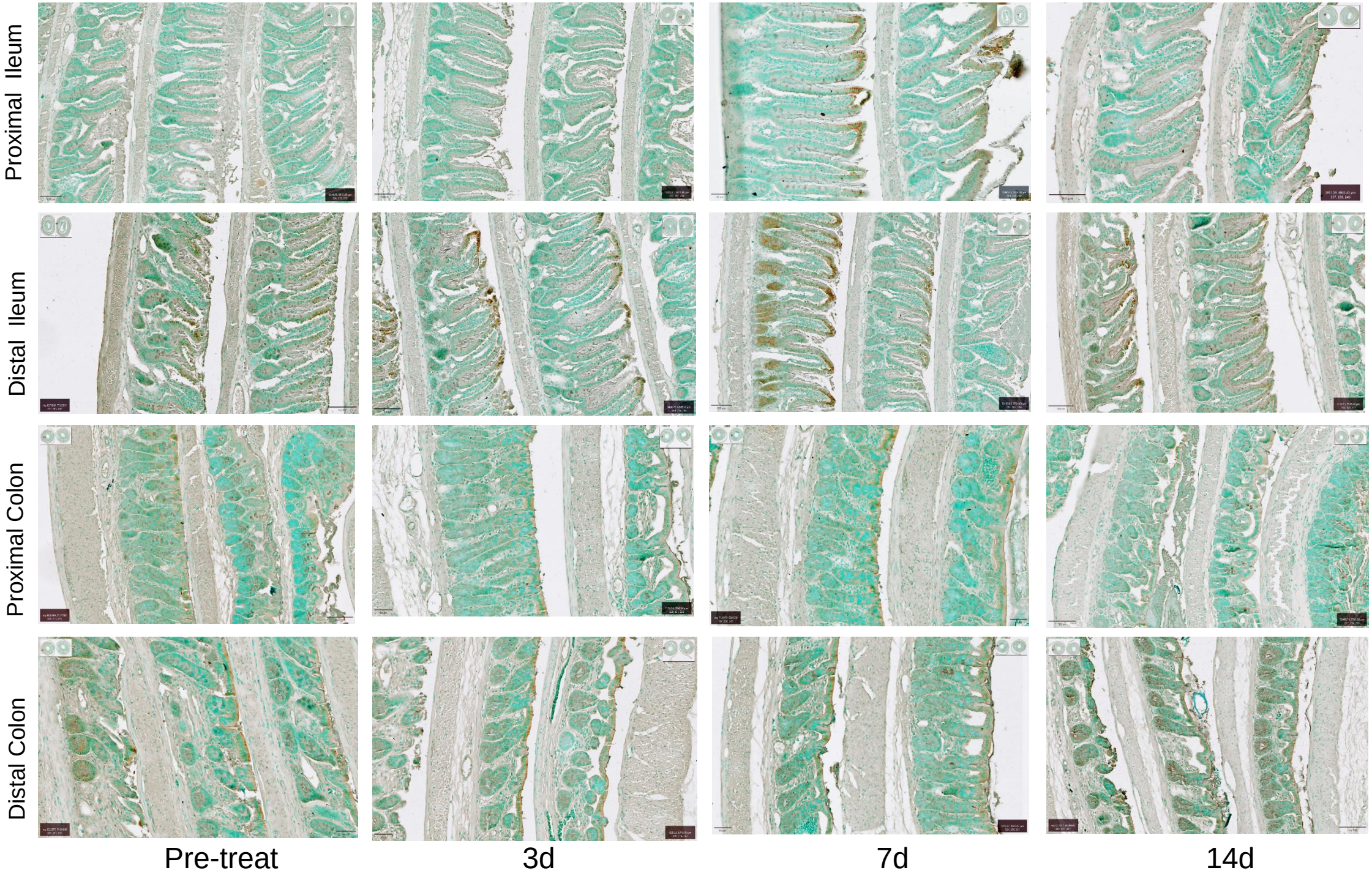

Supporting Information Fig. S12

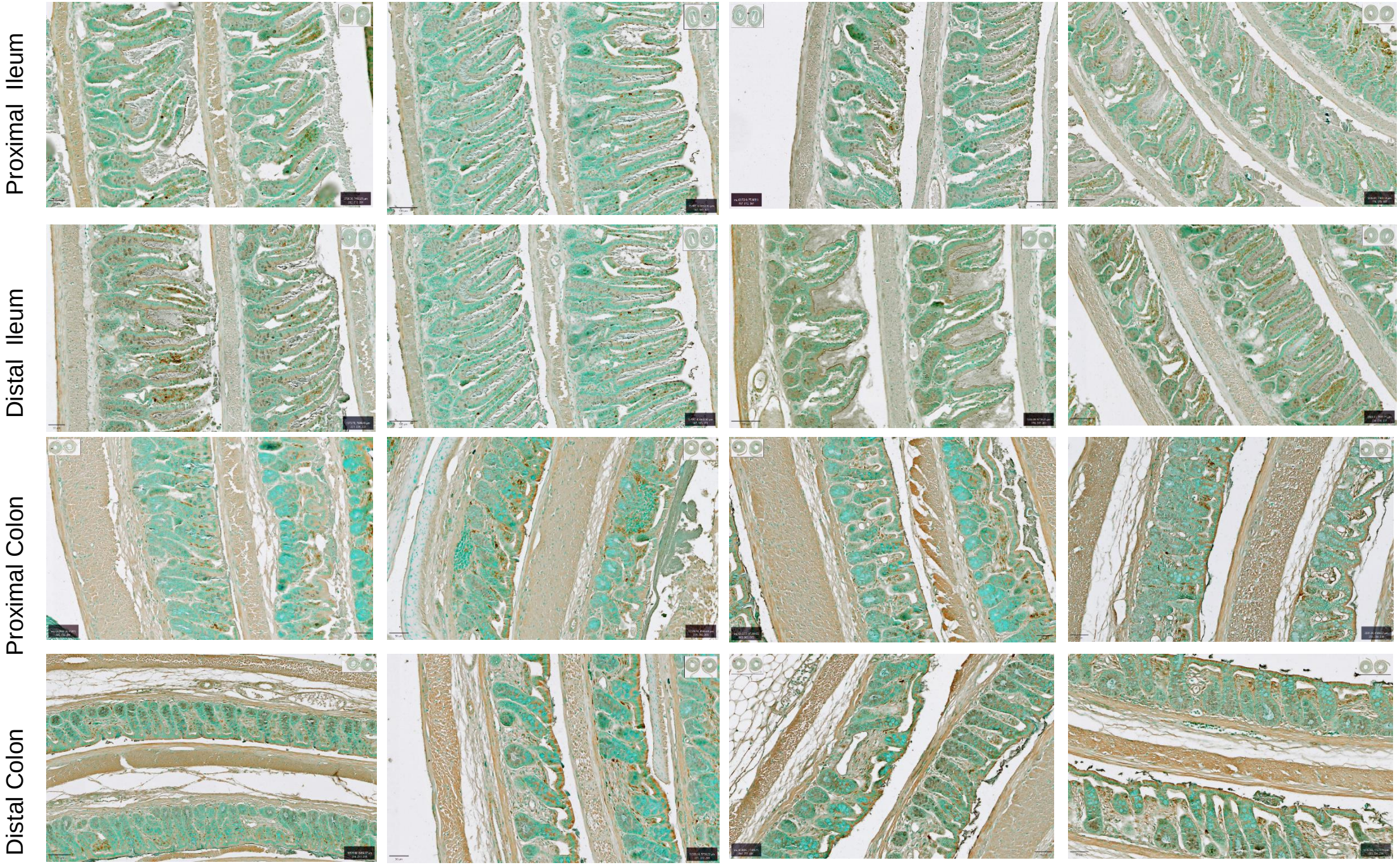

CD4

Supporting Information Fig. S13

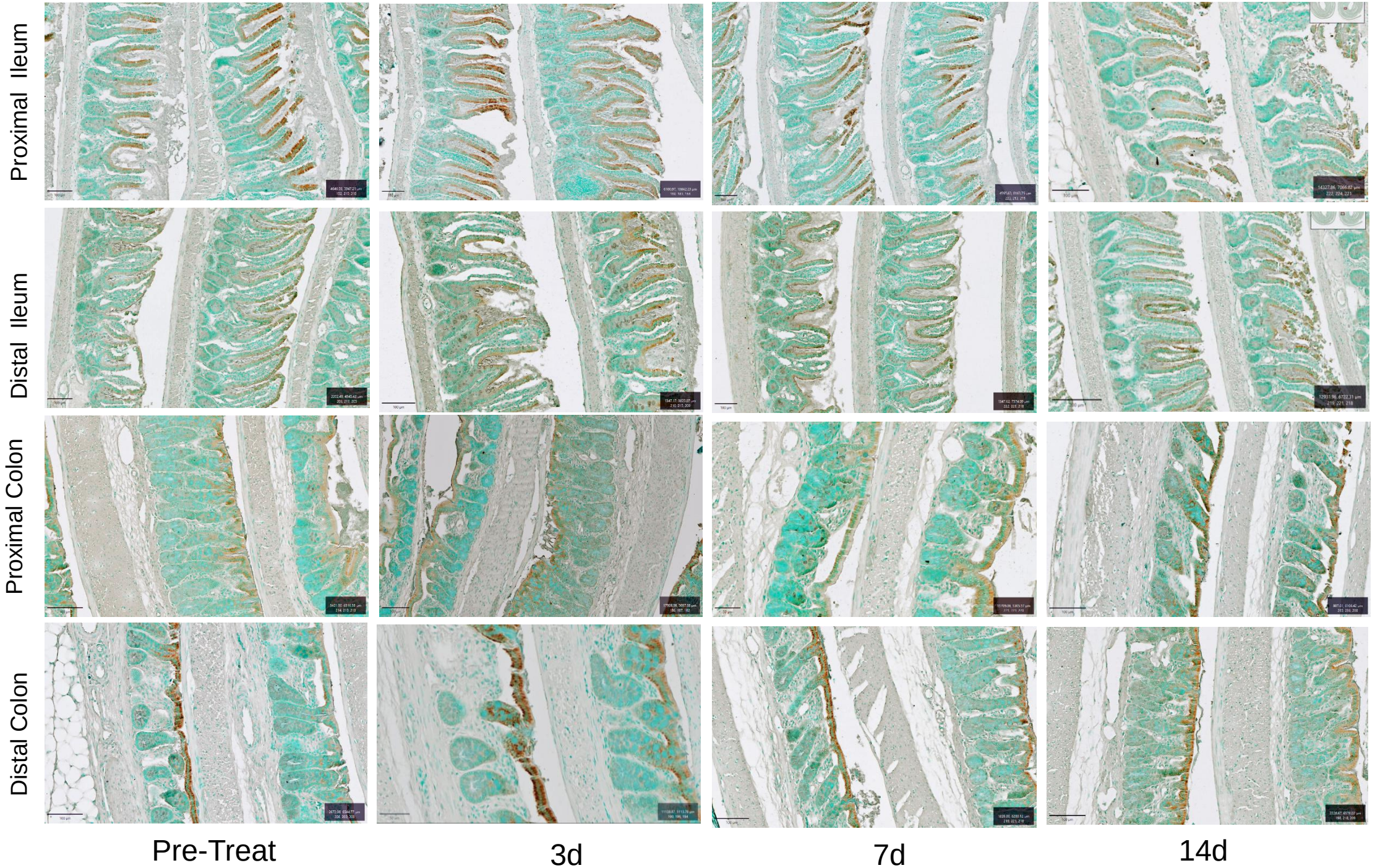

Supporting Information Fig. S14

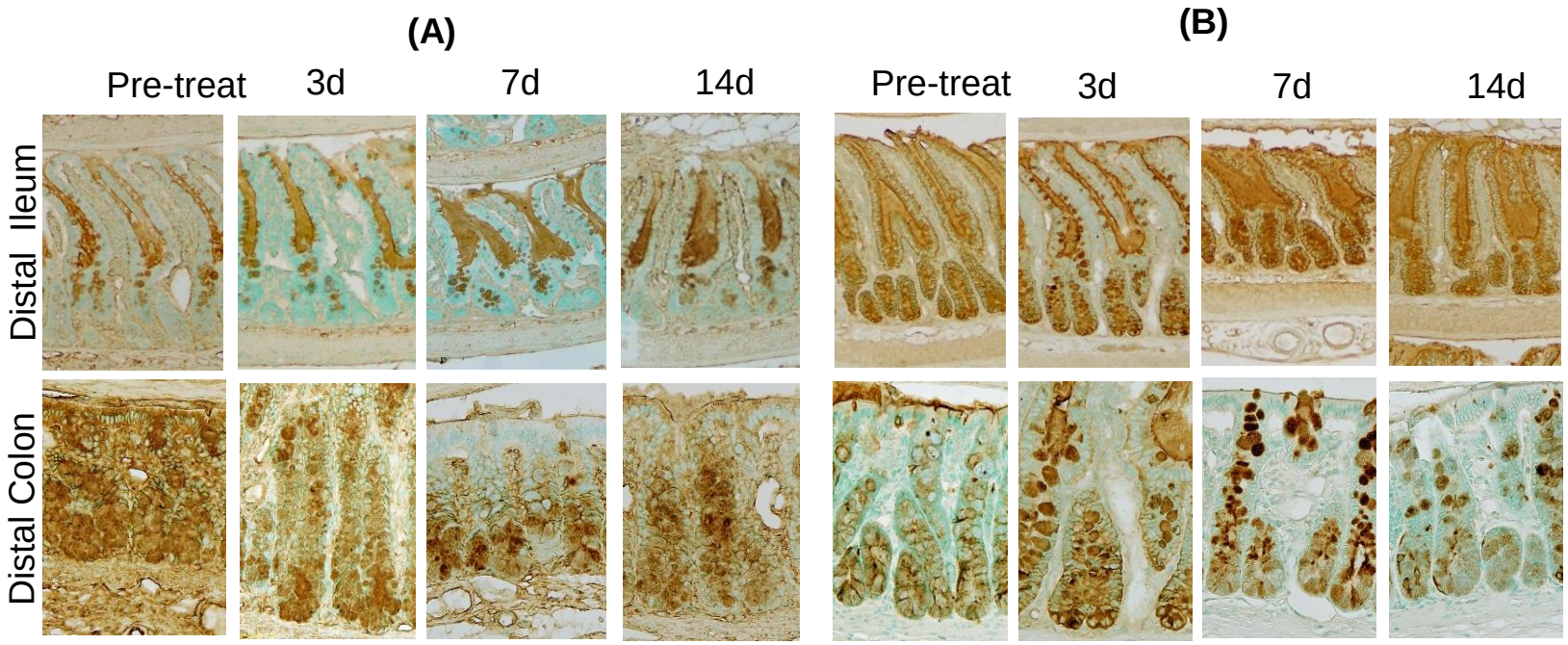
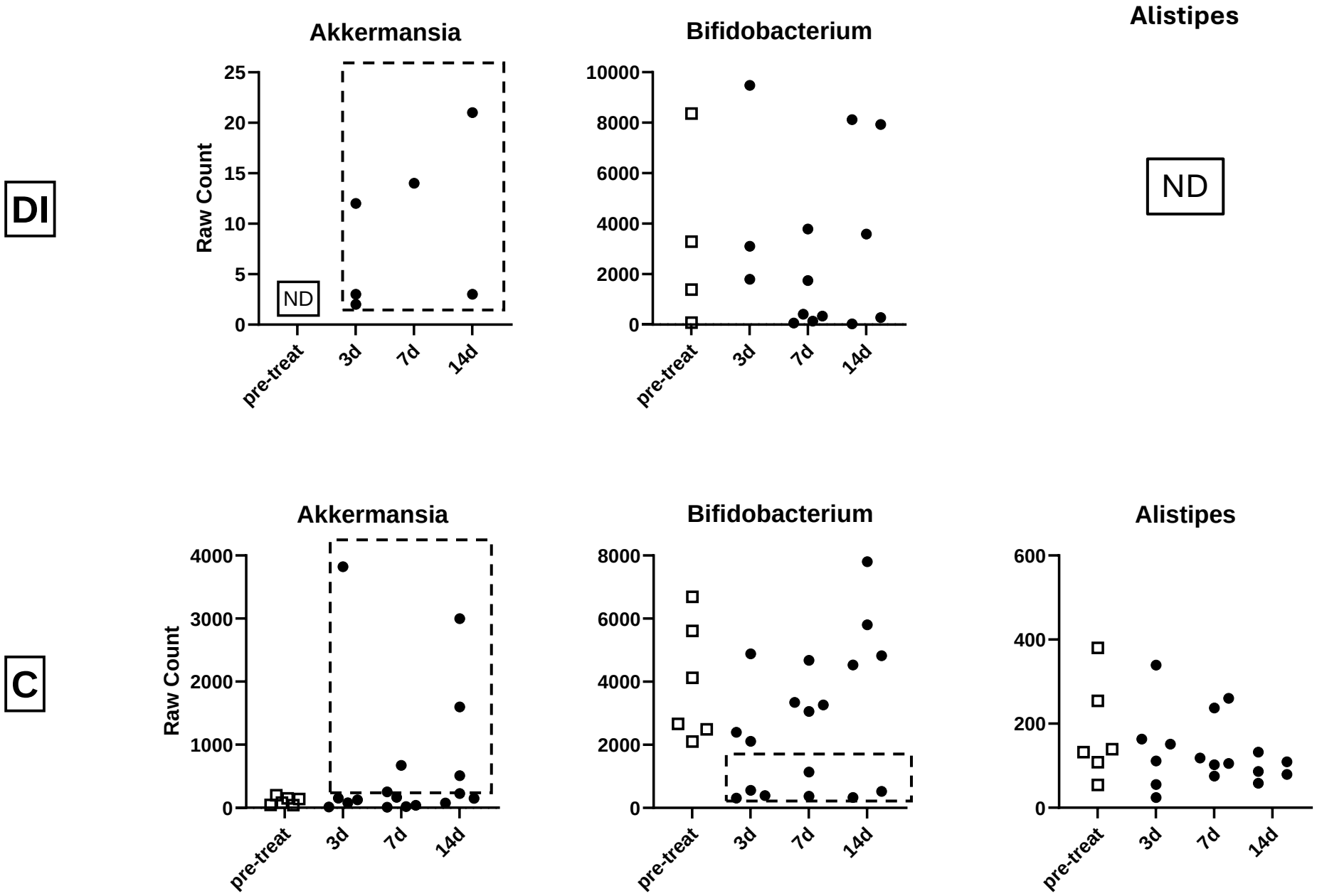
Supporting Information Fig. S15